ANKARA YILDIRIM BEYAZIT UNIVERSITY

GRADUATE SCHOOL OF NATURAL AND APPLIED SCIENCES

EXPERIMENTAL AND NUMERICAL INVESTIGATION OF ENERGY ABSORBING CAPACITY OF ALUMINUM, COMPOSITE, AND HYBRID CRASH BOXES

Ph.D. Thesis by

Sinem KOCAOĞLAN MERT

Department of Mechanical Engineering

December, 2022

ANKARA

EXPERIMENTAL AND NUMERICAL INVESTIGATION OF ENERGY ABSORBING CCAPACITY OF ALUMINUM, COMPOSITE, AND HYBRID CRASH BOXES

A Thesis Submitted to

The Graduate School of Natural and Applied Sciences of

Ankara Yıldırım Beyazıt University

In Partial Fulfillment of the Requirements for the Degree of Doctor of Philosophy in Mechanical Engineering, Department of Mechanical Engineering

by

Sinem KOCAOĞLAN MERT

December, 2022

ANKARA

Ph.D. THESIS EXAMINATION RESULT FORM

We have read the thesis entitled "**Experimental and Numerical Investigation of Energy Absorbing Ccapacity of Aluminum, Composite and Hybrid Crash Boxes**" completed by **Sinem KOCAOĞLAN MERT** under the supervision of **Prof. Dr. Adem ÇİÇEK** and **Prof. Dr. Mehmet Ali GÜLER** and we certify that in our opinion it is fully adequate, in scope and quality, as a thesis for the degree of Doctor of Philosophy.

Prof. Dr. Adem ÇİÇEK	Prof. Dr. Mehmet Ali GÜLER
Supervisor	Co-Supervisor
Prof. Dr. Bora YILDIRIM	Prof. Dr. Erdem ACAR
Jury Member	Jury Member
Prof. Dr. Sadettin ORHAN	Asst. Prof. Yasin SARIKAVAK
Jury Member	Jury Member

Prof. Dr. Sadettin ORHAN

Director

Graduate School of Natural and Applied Sciences

ETHICAL DECLARATION

I hereby declare that, in this thesis which has been prepared in accordance with the Thesis Writing Manual of the Graduate School of Natural and Applied Sciences,

- All data, information, and documents are obtained in the framework of academic and ethical rules,
- All information, documents, and assessments are presented bye with scientific ethics and morals,
- All the materials that have been utilized are fully cited and referenced,
- No change has been made to the utilized materials,
- All the works presented are original,

and in any contrary case of the above statements, I accept to renounce all my legal rights.

Date: **Signature: ……**

Name & Surname:……...…

ACKNOWLEDGMENTS

I would like to express my deepest appreciation to my supervisor, Prof. Dr. Adem ÇİÇEK, and co-supervisor Prof. Dr. Mehmet Ali GÜLER for their precious patience and guidance in every step of my studies.

I would like to thank Prof. Dr. Erdem ACAR and Assoc. Prof. Dr. Murat ALTIN for their valuable contributions and constructive criticisms during my thesis progress. I would also like to thank jury members Prof. Dr. Sadettin ORHAN, Prof. Dr. Bora YILDIRIM and Asst. Prof. Dr. Yasin SARIKAVAK for their comments and proposals to improve the thesis.

I would like to thank Prof. Dr. Metin TANOĞLU and Murat AYDIN for their contribution to characterization tests. I would like to express my gratitude to Hexagon Space Aviation Trade Ltd. for providing honeycomb aluminum fillers. It was obtained free of charge as part of the study. I would like to thank Şakir YALÇIN for his support during the supply phase and Onur MEYDANOĞLU, who shared the documents containing the mechanical properties of the honeycombs from Assan Alüminyum, where the plates of honeycombs were produced.

This thesis was supported by the Scientific Research Project of Ankara Yıldırım Beyazıt University, under project no:5582. I would like to thank Ankara Yıldırım Beyazıt University Scientific Research Projects Coordination Unit for their contributions.

Finally, I would like to express my appreciation to my husband Alper, and my son Umut Tuna.

2022, 29 December **Sinem KOCAOĞLAN MERT**

EXPERIMENTAL AND NUMERICAL INVESTIGATION OF ENERGY ABSORBING CAPACITY OF ALUMINUM, COMPOSITE AND HYBRID CRASH BOXES

ABSTRACT

Within the scope of the thesis, an experimental and numerical study was carried out on the tests of crash boxes and finite element modeling. Aluminum multi-cell tubes were investigated to model the quasi-static experiments. The damage in the constitutive equations was taken into consideration in the finite element (FE) model. The force-displacement behavior and deformation images of the tubes were used to compare the results of the FE model with experiments.

Within the scope of the thesis, an experimental and numerical study was carried out on the tests of composite and hybrid energy absorption tubes and finite element modeling. The absorbed energy, the specific absorbed energy, and the crash force efficiency were obtained in the tests and it was aimed to be verified with the finite element model in the Ls-Dyna commercial program.

First of all, the mechanical properties of the glass fiber reinforced (GFRP) tubes were needed. For this purpose, tensile, compression, and shear tests were carried out by preparing plates in the dimensions specified in the standards. The material data used in the Ls-Dyna program and FE model results were compared with experimental results. The results of the experiments and the numerical model are found compatible.

Keywords: Thin-walled tubes, finite element model, energy absorption, crashworthiness, Ls-Dyna.

ALÜMİNYUM, KOMPOZİT VE HİBRİT BORULARIN ENERJİ SÖNÜMLEME KAPASİTELERİNİN DENEYSEL VE SAYISAL OLARAK İNCELENMESİ

ÖZ

Tez kapsamında çarpışma kutularının testleri ve sonlu eleman modellemesi üzerine deneysel ve nümerik bir çalışma gerçekleştirilmiştir. Yarı statik deneyleri modellemek için alüminyum çok hücreli borular araştırılmıştır. Yapı denklemlerindeki hasar, sonlu elemanlar (SE) modelinde dikkate alınmıştır. SE modelinin sonuçlarını deneylerle karşılaştırmak için boruların kuvvet-yer değiştirme davranışı ve deformasyon görüntüleri kullanılmıştır.

Tez kapsamında kompozit ve hibrit çarpışma kutularının testleri ve sonlu eleman modellemesi üzerine deneysel ve nümerik bir çalışma gerçekleştirilmiştir. Çarpışma kutuları tarafından eksenel yükleme altında absorbe edilen enerji, absorbe edilen spesifik enerji ve ezilme kuvveti verimliliği testlerde elde edilmiş ve sonlu elemanlar modeli ile Ls-Dyna programında doğrulanması amaçlanmıştır.

Sonlu elemanlar modeli ile de doğrulanabilmesi için öncelikle cam elyaf borulara ilişkin mekanik özelliklere ihtiyaç duyulmuştur. Bu amaçla standartlarda belirtilen ölçülerde plakalar hazırlanmış ve çekme, basma ve üç nokta eğme deneyleri gerçekleştirilmiştir. Cam elyaf borular dışındaki malzemelere ait bilgiler kaynaklardan ve malzemenin temin edildiği firmalardan temin edilmiş ve analizlerde kullanılmıştır. Ls-Dyna programında FE model sonuçlarında kullanılan malzeme verileri deneysel sonuçlarla karşılaştırılmıştır. Elde edilen deney sonuçları ile oluşturulan nümerik model sonuçlarının uyumlu olduğu görülmüştür.

Anahtar Kelimeler: İnce cidarlı borular, sonlu elemanlar modeli, enerji absorpsiyonu, çarpışma dayanıklılığı, Ls-Dyna.

CONTENTS

Ph.D. THESIS EXAMINATION RESULT FORM ii
ETHICAL DECLARATION iii
ACKNOWLEDGMENTS iv
ABSTRACT v
ÖZ vi
CONTENTS vii
NOMENCLATURE ix
LIST OF TABLES xi
LIST OF FIGURES xii

CHAPTER 1 - INTRODUCTION 1
1.1 Motivation 5
1.2 Objectives of Thesis 6
1.3 Thesis Structure 7

CHAPTER 2 - LITERATURE REVIEW 8
2.1 Energy Absorbers 8
2.1.1 Crashworthiness 8
2.1.2 Test Methodologies 10
2.1.3 Structural Geometry 10
2.1.4 Crushing Modes and Mechanisms 10
2.2 Aluminum Energy Absorbers 12
2.2.1 Factors Affecting Energy Absorption 13
2.2.2 Experimental Investigations 14
2.2.3 Numerical Investigations 16
2.2.4 Theoretical Investigations 18
2.3 Composite and Hybrid Energy Absorbers 23
2.3.1 Factors Affecting Energy Absorption 25
2.3.2 Experimental Investigations 27
2.3.3 Numerical Investigations 29

CHAPTER 3 - NUMERICAL AND THEORETICAL ANALYSIS OF ALUMINUM TUBES 33

3.1 Results of Experiments 33

3.2 Numerical Analysis of Aluminum Tubes 42

3.2.1 Material Model 42

3.2.2 Model Setup 44

3.3 Theoretical and Numerical Analysis of Aluminum Tubes 48

3.3.1 Empty Rectangular Tubes 48

3.3.2 Foam-filled Rectangular Tubes 55

3.4 Results and Discussion 63

CHAPTER 4 - EXPERIMENTAL AND NUMERICAL STUDIES OF ALUMINUM, COMPOSITE AND HYBRID TUBES UNDER QUASI-STATIC LOADING 65

4.1 Introduction 65

4.2 Fabrication of Tubes 65

4.3 Experimental Setup 66

4.4 Determination of Mechanical Properties 74

4.5 Numerical Modeling Approach of Composite Structures Under Progressive Failure 86

4.5.1 Simulation Setup 86

4.5.2 Finite Element Modeling 87

4.5.3 Simulation Results 94

4.6 Conclusion 106

CHAPTER 5 - SUMMARY, CONCLUSIONS, AND FUTURE WORK 108

5.1 Summary 108

5.2 Conclusions 108

5.3 Future Works 110

REFERENCES 111

CURRICULUM VITAE 122

NOMENCLATURE

Subscripts

b	Width
C	Edge length of the tube cross section
C_{avg}	Linear increasing function of deformation
E	Youngs modulus
$E_{Bending}$	Bending energy
$E_{Membrane}$	Membrane energy
ε_P	Effective true plastic strain
ε_{yp}	Elastic strain to yield and
$\bar{\varepsilon}^p$	Effective plastic strain
F	Crushing force
F_m	Mean crush force
F_p	Peak force
Lc	Total length of all flanges
m	Mass of the structure
n	Strain hardening exponent
N_T	Number of T shape elements
N_L	Number of left corner
N_I	Number of 3 panel type I
N_C	Number of criss-cross
N_{II}	Number of 3 panel type II elements of structure
N_O	Number of corner
t	Thickness of the tube
x_c	Cut-off displacement
σ_u	Ultimate strength
σ_f	Plateu stress
σ_0	Flow stress of material
σ_y	Yield stress
σ_e	Von Mises effective stress
σ_m	Mean stress
σ_t	Effective true stress

$\emptyset$	Yield surface
ϑ^p	Plastic coefficient of contraction
ρ	Density
ρ_f	Density of the foam material
ρ_0	Density of the column

Acronyms

BFM	Basic folding mechanism
CDM	Continuum damage mechanics
CFE	Crush force efficiency
CFRP	Carbon fiber reinforced polymer
EA	Total absorbed energy
FEA	Finite element analysis
FEM	Finite element model
FE	Finite element
FRP	Fiber reinforced polymer
GFRP	Glass fiber reinforced polymer
IPF	Initial peak force
MF	Mean force
PVC	Polyvinylchloride
PS	Polystyrene
PU	Polyurethane
SB	Shell-beam
SEA	Specific energy absorption
SFE	Super folding element
SSFE	Simplified super folding element theory
UD	Unidirectional

LIST OF TABLES

Table 3.1 Foam properties used in numerical analyses [92] 47
Table 3.2 Analysis Results of T4E Model..... 50
Table 3.3 Analysis Results of T8E Model..... 53
Table 3.4 Comparison of mean force predicted by FE model and formula 54
Table 3.5 Analysis Results of T4FF Model Comparison of mean force predicted by model and formula 58
Table 3.6 Analysis Results of T8FF Model..... 61
Table 3.7 Comparison of mean force predicted by model and formula..... 63
Table 4.1 Material properties and tests..... 74
Table 4.2 Test specimen geometry for 0º fibre orientation 76
Table 4.3 Test specimen geometry for 90º fibre orientation 76
Table 4.4 Test results for 0 º fibre orientation..... 78
Table 4.5 Test results for 90 º fibre orientation..... 79
Table 4.6 Test specimen geometry for 0º fibre orientation 80
Table 4.7 Test specimen geometry for 90º fibre orientation 80
Table 4.8 Test results for 0º fibre orientation..... 82
Table 4.9 Test results for 90º fibre orientation..... 83
Table 4.10 Test results for 90 º fibre orientation..... 84
Table 4.11 Test results for [±45] fibre orientation..... 86
Table 4.12 Material properties and tests required for MAT_54..... 87
Table 4.13 Material parameters used in Ls-Dyna 92
Table 4.14 True stress- true effective plastic strain values defined in the MAT_24 card in Ls-Dyna [37] 94
Table 4.15 Comparison of energy absorption values between simulation and experimental results of Al tubes..... 96
Table 4.16 Comparison of energy absorption values between simulation and experimental results of GFRP tubes..... 98
Table 4.17 Comparison of energy absorption values between simulation and experimental results of hybrid tubes 102
Table 4.18 Comparison of energy absorption values between simulation and experimental results of honeycomb-filled hybrid tubes..... 105

LIST OF FIGURES

Figure 1.1 Safety devices of automobiles [1] 2

Figure 2.1 Deformation modes of metallic thin-walled tubes (a) ring mode (b) diamond mode [7] 12

Figure 2.2 Deformation modes of foam-filled thin-walled tubes (a) single tube (b) double tube [7] 13

Figure 2.3 The basic folding mechanism (a) Before deformation (b) After deformation (c) Side view [52] 20

Figure 2.4 Corner Elements of Structures (a) T shape (b) left corner (c) 3 panel type I (d) criss-cross (e) 3 panel type II [57] 21

Figure 2.5 Mean force Calculation Mechanism (a) a foam-filled tube (b) mean crush loads due to the non-filled tube Ptube, the foam-filler Pfoam, and the interaction effect Pinteraction [59] 22

Figure 2.6 Axial crashing modes of composite tubes [60] 24

Figure 2.7 Axial crashing modes of hybrid tubes (a) circular tubes (b) square tubes [60] 24

Figure 3.1 Geometry of the Multi-cell Tubes (a) Tube T4E (b) Tube T8E [42] 34

Figure 3.2 Empty and foam-filled test specimens for T4E and T8E tube configurations [42] 34

Figure 3.3 Progressive failure behavior of multi-cell test specimens (T4E) at different stages: x= 0 mm, x = 30 mm, x = 60 mm, x = 90 mm (a) test specimen T4E1(b) test specimen T4E2 (c) test specimen T4E2 [42] 35

Figure 3.4 Force-displacement graph of T4E multi-cell test specimens [42] 36

Figure 3.5 Progressive failure behavior of multi-cell test specimens (T8E) at different stages: x= 0 mm, x = 30 mm, x = 60 mm, x = 90 mm (a) test specimen T8E1(b) test specimen T8E2 (c) test specimen T8E3 [42] 37

Figure 3.6 Force-displacement graph of T8E multi-cell test specimens [42] 38

Figure 3.7 Progressive failure behavior of multi-cell test specimens (T4FF) at different stages: x= 0 mm, x = 30 mm, x = 60 mm, x = 90 mm (a) test specimen T4FF1(b) test specimen T4FF2 (c) test specimen T4FF3 [42] 39

Figure 3.8 Force-displacement graph of T4FF multi-cell test specimens [42] 40

Figure 3.9 Progressive failure behavior of multi-cell test specimens (T8FF) at different stages: x= 0 mm, x = 30 mm, x = 60 mm, x = 90 mm (a) test specimen T8FF1(b) test specimen T8FF2 (c) test specimen T8FF3 [42] 41

Figure 3.10 Force-displacement graph of T8FF multi-cell test specimens [42] 42

Figure 3.11 Finite element model of aluminum multi-cell rectangular tube 44

Figure 3.12 Mesh Analysis of tube elements for multi-cell rectangular tube 45

Figure 3.13 Mesh Analysis of foam elements for multi-cell rectangular tube 46

Figure 3.14 Curve-fit of analytical hardening curve to the experimental measurements [92] 47

Figure 3.15 Comparison of load-displacement curves between the experimental study and FEA simulation for empty multi-cell T4 tubes 48

Figure 3.16 Comparison of collapse modes of empty T4 tubes between experimental and FEA results 49

Figure 3.17 Comparison of load-displacement curves between the experimental study and FEA simulation for empty multi-cell T8 tubes 51

Figure 3.18 Comparison of collapse modes of T8E tubes between experimental and FEA results :(a) tests (b)FEM 52

Figure 3.19 Comparison of load-displacement curves between the experimental study and FEA simulation for foam-filled T4 tubes 56

Figure 3.20 Comparison of collapse modes of foam-filled T4 tubes between experimental and FEA results 57

Figure 3.21 Comparison of load-displacement curves between the experimental study and FEA simulation for foam-filled T8FF tubes 59

Figure 3.22 Comparison of collapse modes of foam-filled T8 tubes between experimental and FEA results 60

Figure 4.1 Empty test specimens (a) aluminum 6082 T6 tubes (b) GRFP Tubes (c) Hybrid Tubes 66

Figure 4.2 Chamfering of the hybrid tube 66

Figure 4.3 Hybrid tube with bottom plate 67

Figure 4.4 Honeycomb-filled hybrid specimens 67

Figure 4.5 Experiments of Aluminum Tubes 68

Figure 4.6 Experiments of GFRP Tubes 69

Figure 4.7 Experiments of Hybrid Tubes 70

Figure 4.8 Experiments of Honeycomb-Filled Hybrid Tubes 71

Figure 4.9 Force-displacement behavior of test specimens from experiments (a) Aluminum 6082 T6 Tubes (b) GRFP Tubes (c) Hybrid Tubes (d) Honeycomb-filled Hybrid Tubes 72

Figure 4.10 60 mm deformed specimens (a) Aluminum 6082 T6 Tubes (b) GRFP Tubes (c) Hybrid Tubes (d) Honeycomb-filled Hybrid Tubes 73

Figure 4.11 Tensile test specimens 75

Figure 4.12 Tensile test 77

Figure 4.13 Tensile test specimens after tensile tests 77

Figure 4.14 Stress-strain Graph of test specimens (a) 0 º specimens (b) 90 º specimens 78

Figure 4.15 Compression test specimens 79

Figure 4.16 Compression test 81

Figure 4.17 Compression test specimens after tests (a) 0º test specimens after test (b) 90º test specimens after test 81

Figure 4.18 Force-stroke Graph of test specimens (a) 0º test specimens after test (b) 90º test specimens after test 82

Figure 4.19 Shear test specimens 83

Figure 4.20 Shear test 84

Figure 4.21 Shear test specimens after tests 85

Figure 4.22 Stress-Strain Graph of the test specimens 85

Figure 4.23 Ratio of kinetic energy to internal energy of the tube. 88

Figure 4.24 FEM Model of Hybrid Tube 89

Figure 4.25 Trigger mechanism of tubes 90

Figure 4.26 Mesh size sensitivity analysis 91

Figure 4.27 Comparison of collapse modes of aluminum tubes between experimental and FEA results 95

Figure 4.28 Crushing load–displacement curves for aluminum tubes 95

Figure 4.29 Comparison of collapse modes of GFRP tubes between experimental and FEA results 97

Figure 4.30 Crushing load-displacement curves for GFRP crash boxes 97

Figure 4.31 Final failure views of GFRP Tubes 99

Figure 4.32 Comparison of collapse modes of hybrid tubes between experimental and FEA results 100

Figure 4.33 Crushing load–displacement curves for hybrid tubes 101

Figure 4.34 Final Views of Hybrid Tubes 103

Figure 4.35 Comparison of collapse modes of honeycomb-filled hybrid tubes between experimental and FEA results 103

Figure 4.36 Crushing load–displacement curves for honeycomb-filled hybrid tubes 104

Figure 4.37 Final Views of Honeycomb-filled Hybrid Tubes 105

CHAPTER 1

INTRODUCTION

Automobiles have taken an important place in our lives and the benefits they offer us have become increasingly indispensable in our lives. To ensure the safety of drivers and passengers in the case of an accident, numerous safety features are integrated into the automobile structures. Automobiles are equipped with passive safety devices like seat belts, airbags, and thin-walled tubes to prevent or minimize the damage of a crash.

Crash boxes, which are used in automobiles and located on the front bumper, are fasteners capable of absorbing the kinetic energy that occurs in frontal collision accidents by deforming them (see Figure 1.1). The inability of the crash boxes to absorb the impact forces in the event of an accident causes these forces to be transferred directly to the driver and passengers. The most often utilized elements as crash boxes are thin-walled designs that have a tubular structure and can absorb the energy produced by inelastic deformation during impact. Thin-walled energy absorption tubes dissipate the energy and collapse into plastic or ductile mode to minimize the damage to the main body of the vehicle. In this context, it is possible to reach detailed research on which part of the car and at what rate the crash energy will be absorbed in different crash situations by standard centers (such as Euro-Us NCAP) where vehicle safety is tested.

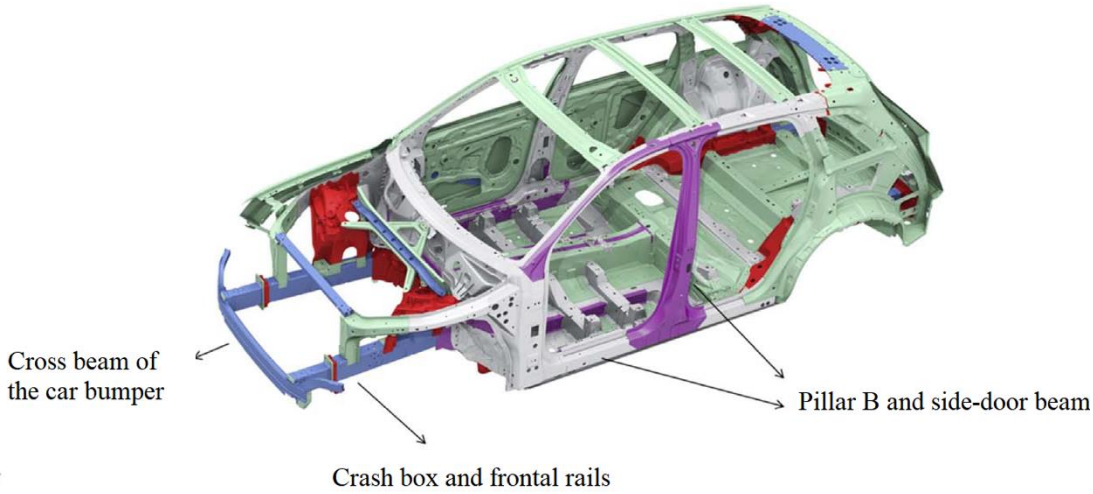

Figure 1.1 Safety devices of automobiles [1]

It is possible to reach many studies on thin-walled tubes in literature. Due to their excellent energy absorption capabilities and low cost, tubular structures built of aluminum and composite materials have recently been researched for this purpose.

Low density, lightweight, high strength, corrosion resistance, thermal, and electrical conductivity are the most important properties of aluminum. The chemical, physical and mechanical properties of aluminum alloys vary depending on the elements used in the alloy and its microstructure. The main alloys added to aluminum are copper, silicon, manganese, zinc, and magnesium. Aluminum alloys are divided into casting alloys and wrought alloys [2]. In comparison to the 2xxx and 7xxx Al alloy series, the 6xxx group of precipitation-hardening alloys has appropriate specific strength and toughness and is significantly less expensive. Slip and twinning are the main plastic deformation mechanisms for the 6xxx series Al alloys under quasi-static loadings (strain rates between 10^{-3} and 10^{-1} s^{-1}). Necking (for tensile loading) and buckling (for compression loading in slender samples) are frequently seen before the failure. On the other hand, shear strain localizations can accurately result in deformation and failure under dynamic impact loadings. Additionally, the material flow stress, which is a function of strain rate, and the dynamic deformation mode, which involves inertia forces, are highly correlated with the ductile structural dynamic plastic deformation mechanics [3].

Composite materials are more durable and rigid due to the greater strength of the fibers in the fiber direction. In the direction perpendicular to the fiber direction, the loads are borne by the matrix and the composites are weaker in this direction, as the matrix is not as durable as the fiber.

Composite materials can be categorized based on the shape of the components that form their structures. By distributing particles made of one or more different materials at random within a matrix made of a different material, *particle-reinforced composite* materials are created. Metal, ceramic, or polymer matrices are used. *Layered composites* are created by combining at least two layers with fibers oriented either one way or another. These layers may be made of wood, glass, metal, or plastic. Additionally, they can be produced using unidirectional fibers, randomly oriented fibers, or other fiber-reinforced matrix layers. It is the oldest and most widely used type of composite in use today. Fibers and appropriate matrix materials are combined to create *fiber-reinforced composite* materials. The fibers' orientation, location, and size inside the matrix have a significant impact on the composites' physical characteristics. High strength in the fiber direction and very low strength in the perpendicular direction to the fibers are obtained by aligning the long fibers in the matrix parallel to one another. It is feasible to achieve great strength in both directions when placing fibers in two perpendicular directions. Composites made of fiber reinforcement may have short or truncated fibers. Short fibers can be found arranged unidirectionally or randomly in the matrix and have a relatively large aspect-to-diameter ratio [3].

Numerous techniques have been devised to produce composite materials. Some of the existing techniques are automated because they were developed using an automation system, while others require manual labor. The size and shape of the component to be manufactured are taken into consideration while choosing the production process. The hand lay-up method, sometimes called the wet laying method, is manually impregnating the textiles (fiber) in a mold using a roller or brush. The fabrics that have been resin-impregnated are then allowed to dry at ambient temperature and atmospheric pressure. It is possible to make composites in suitable sizes because specific instruments are not required for their production. The reinforcement

components used in this procedure are typically chosen from dry fabric. For simple hand application, low-viscosity resins are employed as matrix material. The hand lay-up process can be used to create components including boat hulls, plates, and wind turbine blades. The composite material is created using the spraying method by applying it to a single-sided mold, much to the manual lay-up process. In contrast to the hand lay-up technique, the glue and chopped fibers are sprayed using a gun in this procedure. The gun sprays the fibers onto the application surface after removing the bundles of fibers from a reel, clipping them together with the matrix. Composites created after production are once more cured in an atmosphere. So it is affordable. Although it takes a lot of time, large parts can be made. In the vacuum infusion procedure, the mold where the textiles will be set initially receives a separator film to enable the plate to separate after production. To keep the textiles contained and to seal the mold, double-sided tape is wrapped across its surface. It is ready by trimming the fabric to the right size for the finished plaque. The fabrics are covered with a layer that will peel off, allowing for stripping using a bag and flow net. A hose is used to link the mold's one end to the resin and its other end to the vacuum pump to transfer the resin. Following the vacuum procedure, the fabric layers are allowed to dry before being taken from the mold as a plaque. It is a closed molding technique in which pre-cut reinforcement materials are sandwiched between two molds that are in opposition to one another but complementary in shape. Under pressure from the injection channels, the resin, the matrix material, is pushed into the mold. The number of injection channels, the amount of pressure employed, and the kind of reinforcement materials used all affect how the resin flows. Unidirectional fiber fabrics flow more quickly than braided fiber fabrics. The composite can be dried at room temperature or in an oven when the resin transfer is finished. As a result, the curing temperature affects how quickly pieces are produced. This approach produces excellent surface quality due to the usage of molds. There are created composites with good mechanical qualities and fiber ratios. Compared to hand lay-up and spraying procedures, mold and equipment expenses are significant. Large volume composites with random fiber arrays are produced using the compression molding technique. This approach makes use of reciprocal molds made comprised of lower and higher molds. The lower mold is covered with resin and reinforcement material. The space between the molds is

sealed, and the excess resin emerges from them with air bubbles still inside. The most common type of reinforcement material is short fibers. As a result, the materials made using this process have poor mechanical characteristics. In automotive applications and sheet metal molding, composites made using this technique can replace metal molds. The major benefits are their low cost, corrosion resistance, and lightweight. In filament winding, sometimes referred to as thread winding, resin-soaked filaments are wound at various angles on a revolving cylindrical mandrel to achieve the necessary mechanical qualities. The finished construction is then cured before the mandrel is eliminated. The filaments are pulled into the resin-filled polymer bath before being wrapped. Typically, wrapping is carried out automatically, and once the procedure is finished, it is left to cure in an oven or at room temperature. This technology is typically used to make hollow objects like pipelines and tanks. Continuous fibers are pre-treated in a resin solution before to pultrision, just like in the filament winding procedure. With the aid of specially designed drawing mechanisms, the fibers are dragged into the resin tank and finally into the molds. After undergoing the curing process, composites that take on their final shape are produced. This approach is both quick and cost-effective. The amount of resin is automatically controlled, which results in the production of high fiber density composites with outstanding mechanical properties [4].

Studies carried out in this context are generally on examining the deformation behavior of tube structures and increasing the absorbed energy values by applying different methods. With the developing computer technology, it has become almost mandatory to use finite element software to examine the failure behavior of thin-walled tubes in the deformation process of a crash. The numerical model of the tubes was developed using the widely used finite element programs Abaqus, Ls-Dyna, and Ansys in the literature.

1.1 Motivation

Developing safe and durable vehicles requires an understanding and exploration of the energy absorption capacity of components. It is necessary to know the mechanical properties of the material to model and develop a crashworthy structure. This work

seeks to determine the experimental and numerical performance of thin-walled tubes' crashworthiness under quasi-static conditions. This thesis consists of two parts: numerical and theoretical investigation of aluminum rectangular tubes and experimental and numerical investigation of circular GFRP (Glass Fiber Reinforced Polymer) and hybrid tubes.

In the first part, finite element analyses of empty and foam-filled rectangular multi-cell tubes are verified. The finite element model is validated through experiments based on the force–displacement behavior and the deformation views of the tubes.

In the second part, aluminum, composite and hybrid tubes are tested under quasi-static axial loading. Honeycomb materials are placed inside the hybrid tubes, which are used as passive safety system elements in automobiles, to increase their energy absorption capacity. A three-dimensional finite element (FE) model accounting for the damage in the constitutive equations is developed. It is validated through experiments based on the force–displacement behavior placement and the deformation views of the tubes. The sensitivity of the initial peak force, total energy absorption, specific energy absorption, and crush force efficiency to different mesh sizes, and the type of constitutive equations used are investigated in detail.

1.2 Objectives of Thesis

Within the scope of the motivation explained for this doctoral thesis, the following objectives are determined:

- To validate the test results of empty and foam-filled rectangular multi-cell tubes under quasi-static loading.
- To investigate the energy absorption characteristics of composite and hybrid tubes.
- To investigate the effects of wrapping composite over the aluminum tube to obtain hybrid tubes.
- To investigate the effect of honeycomb filling on hybrid tubes experimentally and numerically.

- To perform characterization tests of glass fiber-reinforced polymer material to determine the parameters that need to be defined in the finite element model.
- To investigate multi-layered composite modeling approaches in terms of energy absorption parameters.
- To determine the prediction capabilities of finite element models that can be used to model aluminum, composite and hybrid tubes under quasi-static loading conditions.

1.3 Thesis Structure

Chapter 2 provides background information on the thin-walled tubes used as energy absorbers.

Chapter 3 includes numerical and theoretical analysis of aluminum tubes to evaluate the success of the material model used for aluminum structures.

Chapter 4 includes experimental and numerical studies of aluminum, composite and hybrid tubes under quasi-static loading. This section contains characterization tests of composite tubes to determine the constitutive model parameters of the material used in the numerical study. The multi-layered composite modeling approaches are also investigated.

Chapter 5 summarizes the conclusion of the thesis work.

CHAPTER 2

LITERATURE REVIEW

2.1 Energy Absorbers

Current thin-walled tubes are made with a variety of strong materials, including metallic, synthetic, and hybrid composite fibers that are reinforced with various types of polymers.

2.1.1 Crashworthiness

The ability of a structure protecting to occupants by absorbing the applied energy in a case of an impact is known as the crashworthiness of a structure. Studies have been made to simulate the event of the crash, providing the ability to design the structures to absorb more energy. Crash processes are complex events where the interaction occurs due to the response of many components. Therefore researchers are confronted with difficulties in numerical modeling. As more composite structures are investigated, the need for both experimental guidelines and numerical tools to simulate them in crash conditions has become a significant issue. Many commercial finite element analysis programs exist and offer various design alternatives for composite failure initiation and propagation mechanisms although these models are still under development and refinement. Theoretical, experimental, and numerical research were conducted to understand the performance of the system to satisfy safety certification requirements.

Researchers are mostly interested in tube dimensions which contain the cross-section, length, and wall thickness of the tube. The effect of geometry and material properties is analyzed on the basis of the obtained failure modes and measured crashworthiness parameters. Various methods have been studied to absorb more energy by increasing the crush force efficiency while reducing the initial peak force.

The effect of geometry and material properties is analyzed on the basis of the obtained failure modes and measured crashworthiness parameters. These parameters may

include specific energy absorption (SEA), total absorbed energy (EA), initial peak force, mean force, and crush force efficiency (CFE), etc. The ultimate goal is therefore to absorb more energy while reducing the initial peak force. The ability of energy absorption is usually assessed by the following indicators [5].

Total absorbed energy (EA)

EA is obtained from the area under the load-displacement curve. Therefore, EA can be obtained using the following formula:

$$EA = \int_0^{x_c} F\, dx \tag{2.1}$$

where F is the crushing force, and x_c is the cut-off displacement.

Specific energy absorption (SEA)

For energy absorbers, energy absorption per unit weight is a significant design metric. It is named Specific Energy Absorption (SEA) and can be calculated as:

$$SEA = \frac{Total\ Energy\ \ Absorbed}{Total\ Weight} = \frac{EA}{m} \tag{2.2}$$

where m is the mass of the structure.

Initial peak force

Initial peak force (IPF) is the maximum force at which folding starts. The first peak at the load-displacement curve during crushing is used to determine the initial peak force.

Mean crush force

The mean crush force, F_m, is the ratio of the total absorbed energy, EA, to the cut-off displacement, x_c. The mean crush force (MF) is calculated by the following equation:

$$F_m = \frac{EA}{x_c} \tag{2.3}$$

Crush force efficiency (CFE)

The crush force efficiency, CFE, is defined as the ratio of the mean force, (F_m) to the peak force, (F_p). CFE is expressed as:

$$CFE = \frac{F_m}{F_p} \quad \textbf{(2.4)}$$

In literature SEA and initial peak force are used to measure the crashworthiness of the tubes under axial loading. Herein, in addition to SEA and initial peak force, EA and mean load is also used in both experimental and numerical studies.

2.1.2 Test methodologies

The majority of previous studies include the investigation of crash boxes under axial loading. Static and dynamic tests result in different failure modes and various energy absorption characteristics. Although some studies focus on lateral crushing, many of them investigate axial crush effects on crashworthiness although energy absorbers experience a combination of axial and oblique loads in real crash events, mostly.

2.1.3 Structural geometry

Extensive effort has been performed on understanding the effects of geometrical parameters and material types on the energy absorption performance of thin-walled tubes. Researchers are most interested in the effect of various types of specimen geometry on the energy absorption capability by varying the geometric parameters such as wall thickness, axial length, diameter, or circumference.

2.1.4 Crushing modes and mechanisms

The energy is typically absorbed by plastic deformation mechanisms in metallic crash boxes such as steel and aluminum. Fracture occurs after severe plastic deformation. Failure evolution can occur in metals with the formation of a neck or without a neck is observed [6].

The fiber composite, on the other hand, is naturally brittle and capable of releasing energy via a variety of collapse mechanisms including inversion or splitting deformation modes.

It is expected that the design and the material will have the ability to absorb energy to provide an acceptable level of deceleration acceleration. Composite materials absorb energy with a constant crushing load due to the simultaneous occurrence of different energy dissipation mechanisms. Catastrophic damage and progressive damage modes are the most frequent ways of collapse for composite materials in thin-walled tubes. A sudden increase in maximum load follows a load drop in catastrophic failure. After failure, the sample loses most of its ability to carry the compression load. Most catastrophic damage mechanisms result from uncontrolled crack propagation within or between layers within the material. Progressive damage can be obtained by creating a trigger at one end of the sample to initiate damage. As a result, a stable damage progression can be observed and the peak load can be reduced. Accordingly, in the case of progressive damage, the material does not lose its load-bearing ability after deformation starts.

In most experiments, with the contact of the striker, *matrix cracking* first occurs in the upper surface layer. When the striker crashes the upper surface layer, the matrix cracks in the impact zone and generally runs parallel to the fiber direction in layers composed of unidirectional (UD) fibers. Two types of matrix cracks, tension, and shear cracks, are observed in composite structures. Tensile cracks occur when in-plane normal stresses on the surface exceed the shear strength. Shear cracks, on the other hand, occur at a certain angle from the mid-plane due to transverse shear stresses. *Delamination* damage is a continuation of matrix crack. Delamination is the separation between two adjacent composite layers after the crack is observed in the case of a crash. In laminated composites, delamination occurs due to the difference in bending stiffness between layers and shear stresses. Layer thickness, stacking sequence, and material properties affect delamination damage. *Fiber cracks* occur after matrix deformation and delamination. Local tensile stresses that occur in the structure with extensive matrix cracking and delamination cause fiber cracks. Since fibers are the main load-

bearing part in composites, the strength of the structures decreases significantly after fiber cracks [4].

2.2 Aluminum Energy Absorbers

Over the past decades, many research efforts have been made to understand the collapse behavior of thin-walled metal tubes under static or dynamic axial loading. Early research mainly focuses on theoretical and experimental studies.

Thin-walled metallic circular structures exhibit two main folding behaviors under loading, the ring/concertina mode, which is axisymmetric, and diamond mode, which is non-symmetric mode as shown in Figure 2.1. Deformation shape depends on the ratio of diameter to thickness of the structure [1].



Figure 2.1 Deformation modes of metallic thin-walled tubes (a) ring mode (b) diamond mode [7]

While an accordion-like appearance is obtained after deformation in symmetrical folding, an appearance in the form of overlapping equilateral triangles emerges in diamond folding. However, most of the square and rectangular tubes do not undergo progressive collapse and they confront splitting or unexpected collapse modes. When exposed to axial loading, many of the foam-filled square or rectangular tubes bend externally and the tube splits along the corners resulting in the split mode as shown in Figure 2.2.

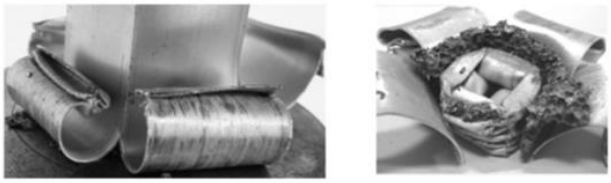

(a) (b)

Figure 2.2 Deformation modes of foam-filled thin-walled tubes (a) single tube (b) double tube [7]

2.2.1 Factors affecting energy absorption

The increase in the energy values absorbed by tubular structures is the main goal of many studies. The deformation mode of tubes is significantly influenced by loading velocity in addition to geometrical features [8]. The tubes are reinforced from inside and/or outside to absorb more energy. Metallic or polymer-based foams are generally used as internal reinforcement. These foams are preferred as reinforcement elements due to the ability of high displacement values at an approximately constant load value. They also have a much lower density than the tubes in which they are used. While closed-pore aluminum foams are generally used in metallic tubes, polyvinylchloride (PVC) and polystyrene (PS) are preferred foam types in polymer-based foams, especially polyurethane (PU). In numerous studies recently, glass fiber-reinforced polyamide has also been mentioned as a filler material [8].

To absorb more energy, many studies have investigated hybrid structures that combine both metallic and composite materials, such as composite-wrapped thin-walled metal tubes. The high strength-to-weight ratio of composites and the elasticity and progressive deformation mode of metals are two desirable features that are combined in hybrid structures.

Also, in square or rectangular tubes increasing the number of corners in the cross-section of a tube increases plastic deformation and, thus, total absorbed energy. Therefore, multi-cell tubes are investigated as energy-absorbing components [8].

2.2.2 Experimental Investigations

Due to the cost and complexity of dynamic tests, the crash boxes are tested in quasi-static test setups in most of the studies. To improve the crashworthiness of foam-filled tubes few researchers apply dynamic test conditions. An experimental investigation was carried out by Langseth et al. [9] to study the behavior of square thin-walled aluminum extrusions in alloy AA6060 subjected to axial loading. Both static and dynamic tests were performed and the primary variables were the wall thickness and temper of the square tubes and the impact velocity of the projectile. The mass of the projectile in the dynamic tests was 56 kg, while the impact velocity was in the range of 8 - 20 m/s. Galib et al. [10] aimed to present further experimental data and validate an existing theoretical prediction for static and dynamic axial crushing of circular aluminum extrusions in alloy A6060 temper T5. They searched the relationship between dynamic and static behavior to validate the numerical prediction of the crushing behavior using the experimental results obtained. In the study of Simhachalam et al. [11] compression behavior and energy absorption of aluminum alloy AA7005 and AA7003 tubes were investigated both experimentally and numerically. Ls-Dyna software was used for the static and dynamic simulations of AA7005, AA7003, AA6061, and high strength steel (DP800) tubes of equal dimensions. True stress–plastic strain curves at different strain rates were used in the dynamic simulations of AA7003 and DP800 tubes. Dynamic simulations were done with drop velocity from 7 to 15 m/s to understand the inertia and strain rate effects on energy absorption.

Thin-walled tubes in the form of multi-cell square, triangular, and hexagonal sections are investigated to absorb more energy. Nia and Parsapour [12] applied quasi-static loading to simple and multi-cell thin-walled aluminum tubes with triangular, square, hexagonal, and octagonal geometries. According to the study, the multi-cell tubes had a higher energy absorption capability than simple sections. Also, hexagonal and octagonal multi-cell tubes absorbed the highest energy per unit of mass.

Thin-walled tubes are reinforced by fillers to absorb more energy. Metallic [13, 14, 15, 16] or polymer-based foams are generally preferred as fillers due to lower density

than the tubes in which they are placed. While closed-pore aluminum foams are generally used in metallic tubes, polyvinylchloride, PU [17], and PS are the most preferred foams besides laterally graded foams [18] and honeycombs [19, 20].

To improve crashworthiness, researchers have been examining more effective materials and structural designs. Due to its reduced density compared to other metal foams, aluminum foam filling has drawn attention. Thin-walled tubes filled with foam have a greater potential to absorb energy than empty thin-walled tubes without considerably adding to their overall weight. Determining and improving the ability of thin-walled structures to absorb energy has thus been the subject of numerous studies. Under various loading angles, Gao et al. [21] presented a foam-filled elliptical tube and contrasted it with other hollow and foam-filled tubes with various cross-sections, including square, circular, and rectangular. They discovered that foam-filled elliptical tubes have higher SEA and absorption capacities than other cross-sectioned empty and foam-filled tubes. Similar to this, Kılıçaslan [22] investigated the axial dynamic crushing reactions of finite element models of empty corrugated circular tubes and corrugated single and double circular tubes loaded with aluminum foam. According to their investigation, the double-tube configurations filled with aluminum foam had longer corrugations and a greater SEA. Qi et al. [23] studied the oblique impact of thin-walled round and conical tubes that were empty and filled with foam. The best tube configurations were different for the various impact angles, and the conical tube had the greatest SEA values. Conical tubes filled with foam were subjected to quasi-static axial loads, and Ahmad et al. [24] investigated the axial crushing and energy absorption response. Investigations were done into the effects of the foam filler's density, semi-apical angle, and wall thickness. The studies showed the benefits of using foam-filled conical tubes as energy absorbers. The SEA has been utilized as a design criterion for the lightweight needs of thin-walled structures made of cellular materials or foam. Toksoy et al. [25] simulated the quasi-static crushing of both filled and empty tubes. Results were verified by an experimental quasi-static crushing test on both filled and empty commercial 1050H14 Al tubes with Alulight foam. Due to the axial and lateral displacement of the tube wall folds caused by the foam filler, partial foam filling of the tubes increased the SEA and mean load. Altın et al. [26] examined how the amount of foam fill affected the ability of square and circular tubes

with narrow walls to absorb energy. Under quasi-static test conditions, compression tests on aluminum tubes with circular cross sections and four different foam fill ratios (11.4%, 22.8%, 34.2%, and 100%) were performed. It is determined that the SEA of a foam-filled square design is five times more than the SEA of an empty square design. The SEA and CFE performances of the foam-filled square design can be improved by 87% and 42%, respectively, by altering the wall thickness.

2.2.3 Numerical Investigations

Daily improvements in computer systems and the creation of more robust finite element algorithms have made numerical calculations easier. The majority of studies have concentrated on creating numerical models that will make it easier to conduct expensive experimental studies. To do this, a variety of fundamental models, delamination methods, and damage initiation mechanisms are researched.

The crushing responses of aluminum 6060-T4 tubes with and without windows under axial and oblique loading were investigated by Nikkhah et al. [27]. The finite element package Ls-Dyna was used to simulate the dynamic crushing behavior of the tubes. According to the study, windowed tubes exhibit lower initial peak loads than simple tubes. For the majority of load angles, simple tubes absorbed more energy than windowed tubes, but circular and square windowed tubes absorbed more energy than other windowed tubes. In a similar manner, Zhang and Cheng [28] used Ls-Dyna to model foam-filled square and multi-cell square aluminum 6060 tubes. By adding a pre-crushed trigger to multi-cell columns, they were able to reduce the first peak force and improve the energy absorption of a multi-cell tube.

Few numerical studies about the axial crushing behavior of thin-walled tubes under quasi-static and dynamic conditions have been published in the literature, which also accounts for the failure of the FEA model. Aluminum AA7003-T7 tubes with rectangular, hexagonal, and octagonal cross-sections were tested and modeled by Kim et al. [29]. The center section experienced significant deformation and folding. The tubes with an octagonal cross section outperformed the others in terms of energy absorption performance and mean load. Square thin-walled columns made of the aluminum alloy AA6060 were subjected to tests by Reyes et al. [30] under oblique

load. On the ability to absorb energy, the effects of thickness and heat treatment were examined. Square thin-walled aluminum tubes with a variety of thicknesses, section sizes, and impact velocities were the subject of the research by Qiao et al. [31]. To validate the developed model, geometric flaws and a damage model were added. The collapse of a circular tube formed from the extruded aluminum alloy EN AW-7108 T6 was studied by Marzbanrad et al [32]. The ductile failure criterion and elastic and plastic boundary conditions were taken into consideration in the model. The results demonstrated that implementing an elastic boundary condition could alter the mode of deformation and reduce the peak force. Different numerical models were created for EN AW-7108 T6 based on Hooputra's ductile damage model [33] in the investigations of Allahbakhsh et al. [34] and Estrada et al. [35, 36]. These studies employed the Müschenborn-Sonne Forming Limit Diagram (MSFLD) and shear, ductile, and damage start criteria. The effects of cross-section on the multi-cell profiles' performance in terms of crashworthiness and the effects of circular hole discontinuities on the energy absorption capabilities of tubes were respectively the focus of the investigations [35, 37]. The peak load was reduced by up to 4.74% using circular hole discontinuities in comparison to a tube without them. The other work by Estrada et al. [37] focused on the progressive damage modeling of aluminum 6063-T5 bi-tubular structures having square, polygonal, and circular cross-sections, as well as circular discontinuities. With the use of the Johnson-Cook (J-C) failure model, bitubular structures were modeled. When the hole in the inner profile was in the middle, a buckling effect was seen.

Mirfendereski et al. [38] investigated the energy absorption performance of foam-filled straight and tapered tubes under static and dynamic conditions. They observed a decrease in initial peak load when they increase the number of oblique sides of the sections. Although foam density did not affect the initial peak force, total absorbed energy increased with the increasing density. Ahmad and Thambiratnam [24] explored that foam filling increased the initial peak load and energy absorption of conical tubes. Also, they found that the initial peak load increased when the foam density increased. Goel [39] compared the empty and foam-filled circular and square tubes under impact loading and determined that circular tubes absorbed more energy than square tubes with the foam filler. Metallic foams were modeled using different material models

such as MAT_5, MAT_26, MAT_63, and MAT_75 in Ls-Dyna. Hanssen et al. [16] evaluated these models and observed that these models cannot model the change of foam compressibility and density during deformation. Also, these models can not be enhanced to include the change in compressibility. Deshpande and Fleck [40] proposed the self-similar evolution model and differential hardening model. The self-similar evolution model specifying the shape of the initial yield surface was implemented into the material model (MAT_154) of Ls-Dyna [41]. Zhang and Cheng [28] modeled foam-filled square and multi-cell square tubes using the material model (MAT_154) for aluminum foam. The collapse mode of the tubes and absorbed energy are predicted consistently with the test results. Similarly, Altın et al. [4] investigated empty and partially foam-filled circular and square columns using MAT_154 to model foam. They observed that foam-filled square tubes performed the best energy absorption. The common determination of these investigations was the increase in the energy absorption of the tubes by using metallic foam inside.

In this thesis, the numerical modeling of aluminum rectangular tubes under axial compression has been studied. Modeling studies are based on experimental studies of Murat Altın [42]. The energy absorption performance of aluminum tubes under quasi-static loading was studied extensively in the literature. Usually, two-dimensional shell elements are used both in industry (automotive, aerospace, and related industries) and academia as well as in the mentioned references above to model thin-walled tubular structures. The numerical study was performed in order to model the energy absorption performance and deformation views of aluminum empty and foam-filled multi-cell tubes.

2.2.4 Theoretical Investigations

Numerous investigations are conducted to predict the energy absorption performance of thin-walled tubes. Alexander [43] studied the axial loading of cylinders as energy absorbers analytically. Experimental and theoretical investigations were carried out by Abramowicz and Wierzbicki [44, 45], Abramowicz and Jones [46, 47], and Andrews et al. [48] to study the energy absorption behavior of metallic tubes under static and dynamic loads. Folding energy was calculated for the tubes under axial loading. The

folding mechanism in tubes was similar; the peak occurs at the earlier stages of loading and oscillations occur with deformation. Wierzbicki and Abramowicz[44] calculated the mean force of a square column according to the Basic Folding Mechanism (BFM) that they introduced to model the deformation theoretically. They predicted the mean force of the rectangular and square columns considering the extensional and bending modes with the proposed theory using the Super Folding Element (SFE). Also, they predicted the mean force of the multi-cell tubes, considering the six deformation modes with more accuracy according to the formula below:

$$P_m = 9.56\,\sigma_0\,b^{1/3}\,t^{5/3} \qquad \textbf{(2.5)}$$

where σ_0 is the flow stress of the material, b and t are the width and thickness of the tube, respectively.

Santosa and Wierzbicki [49] calculated the mean force of the tubes with low-density filler material, such as honeycomb or aluminum foam. They investigated the effect of fillers on the energy absorption performance of a square tube under quasi-static loading. Honeycomb filling was found more weight efficient than aluminum foam under axial loading.

Hanssen et al. [50] investigated the effect of wall thickness and foam density on the deformation behavior of aluminum 6060 circular sections filled with aluminum foam under quasi-static and dynamic loading. They developed a formula that calculates the mean force of tubes consistent with experiments. Santosa et al. [51] calculated the mean force of the aluminum foam-filled steel tubes, based on the experiments and numerical simulations. The mean force of a filled tube increased with the increase of foam strength and geometry of the tube. Chen and Wierzbicki [52] proposed the Simplified Super Folding Element Theory (SSFE) simplifying the formula of Wierzbicki and Abramowicz [44] to predict the mean force of single-cell and multi-cell tubes with aluminum foam inside. The length of the folds was assumed to be constant during deformation. It was found that the interaction between the foam and the tube wall increases the total crushing resistance by amounts equal to 80% of the direct foam resistance. The geometry of the basic folding mechanism that they used in the formula is shown in Figure 2.3.

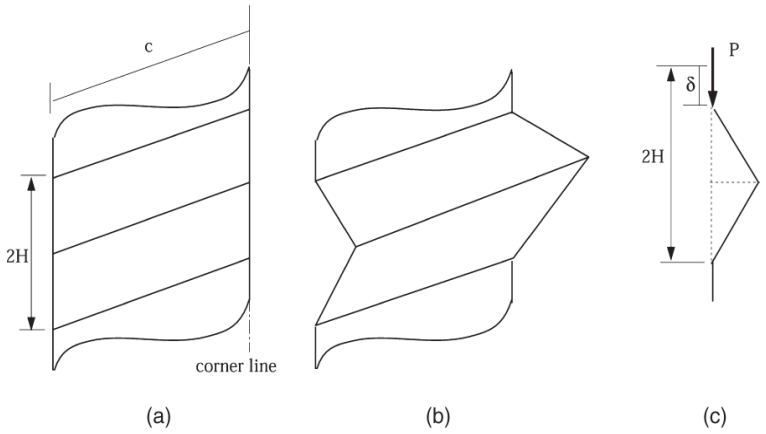

Figure 2.3 The basic folding mechanism (a) Before deformation (b) After deformation (c) Side view [52]

Niknejad et al. [53, 54] derived a formula to predict crushing force and absorbed energy during folding in square tubes with polyurethane foam inside under the axial loading. In the theoretical analysis, interaction between the polyurethane foam and tube wall was considered to predict the energy absorbed. Also, the crushing wavelength was considered as a constant parameter which is a function of column geometrical dimensions. Similarly, Abedi et al. [55] formulated absorbed energy and crush force of empty and polyurethane foam-filled rectangular and square tubes. They predicted the instantaneous folding force which is dependent on is dependent on the flow stress of the tube material (σ_0), wall thickness (t), and edge length of the tube cross-section (C). Sun et al. [56] studied aluminum 6061 square tubes with axial and lateral functionally graded thicknesses. They investigated the energy absorption of tubes experimentally, numerically, and theoretically under axial crushing load to compare with equivalent uniform thickness tubes of the same mass. In the present study, the mean crushing force of a square tube for uniform thickness is calculated as follows [56]:

$$P_m = 13.06\,\sigma_0\, b^{1/3}\, t^{3/5} \qquad \textbf{(2.6)}$$

where σ_0 is the flow stress of the material, b and t are the width and thickness of the tube, respectively.

Xie et.al. [57] calculated the mean force of empty multi-cell tubes according to the formula given. They applied to energy balance equation to formulate the mean force for multi-cell tubes.

$$F_m\, 2Hk = E_{Bending} + E_{Membrane} \quad \textbf{(2.7)}$$

where $F_m$is the mean force, k is the effective crush distance coefficient, $E_{Bending}$ is bending energy and $E_{Membrane}$ is membrane energy. External work due to compression is equal to the total of the plastic deformation of the membrane and bending. Xie et.al. [57] formulated mean force as:

$$P_{mean} = \frac{1}{2k}\sigma_0 t\sqrt{(4\mathrm{N}_T + 2\,\mathrm{N}_L + 3.65\mathrm{N}_I + 8N_C + 5.4\mathrm{N}_{II})\,\pi\,\mathrm{Lc}\,\mathrm{t}} \quad \textbf{(2.8)}$$

where Lc is the total length of all flanges, σ_0 is the flow stress of the material and t is the wall thickness. Also N_T is number of T shapes, N_L is number of left corners, N_I is number of 3 panel type I, N_C is number of criss-crosses and N_{II} is number of 3 panel type II elements of the structure. As shown in Figure 2.4.



(a) (b) (c) (d) (e)

Figure 2.4 Corner Elements of Structures (a) T shape (b) left corner (c) 3 panel type I (d) criss-cross (e) 3 panel type II [57]

The flow stress of the material is calculated as:

$$\sigma_0 = \sqrt{\frac{\sigma_y \sigma_u}{1+n}} \quad \textbf{(2.9)}$$

where σ_y is the yield stress, σ_u is the ultimate strength and n is the strain hardening exponent. Similarly, Zhang et al. [58] formulated the mean crush force of multi-cell square tubes that were divided into equal cells according to the formula given:

$$F_{mean} = \sigma_0 t\sqrt{(4\mathrm{N}_C + 2\,\mathrm{N}_T + N_O)\,\pi\,\mathrm{Lc}\,\mathrm{t}} \quad \textbf{(2.10)}$$

where N_T is number of T shapes, N_C is number of criss-cross sections, and N_O is number of corners.

Googarchin et.al. [59] formulated the mean force of the foam-filled tubes considering a combination of mean force due to the non-filled tube, the foam-filler, and interaction between them as shown in Figure 2.5.

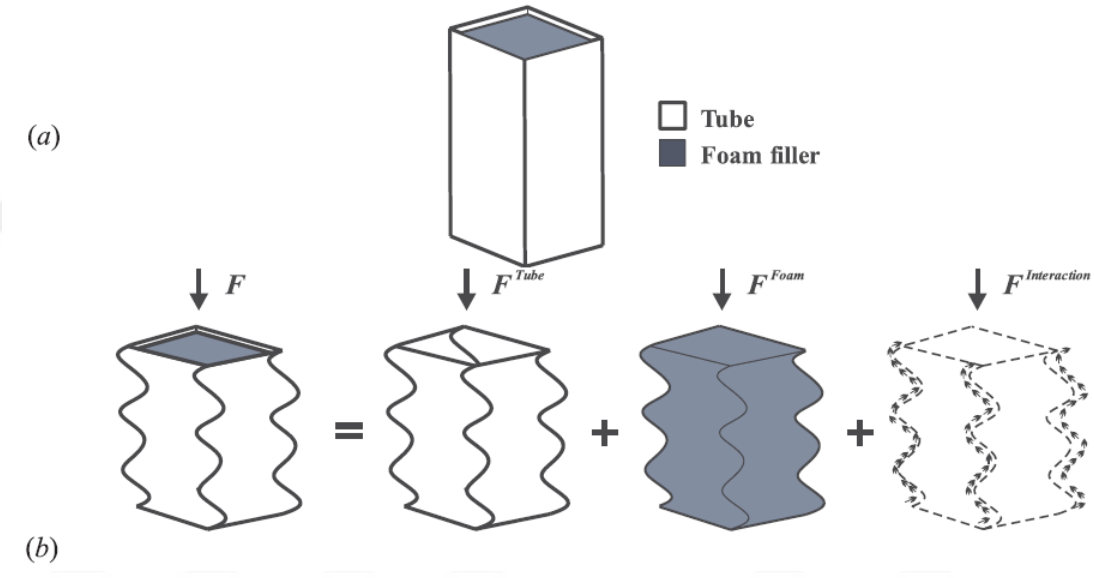

Figure 2.5 Mean force Calculation Mechanism (a) a foam-filled tube (b) mean crush loads due to the non-filled tube $\boldsymbol{P_{tube}}$, the foam-filler $\boldsymbol{P_{foam}}$, and the interaction effect $\boldsymbol{P_{interaction}}$ [59]

Googarchin et.al. [59] formulated mean force as:

$$P_{mean} = P_{tube} + P_{foam} + P_{interaction} \quad \textbf{(2.11)}$$

P_{foam} and $P_{interaction}$ can be calculated from the equations [59].

$$P_{foam} = \sigma_f \; a \; b \quad \textbf{(2.12)}$$

$$P_{interaction} = C_{avg} \sqrt{\sigma_f \; \sigma_0} \; c \; t \quad \textbf{(2.13)}$$

$$c = \frac{a+b}{2} \quad \textbf{(2.14)}$$

where σ_0 is the flow stress of the material, σ_f is the plateau stress, axb is the cross-section, t is the wall thickness and C_{avg} is the linear increasing function of deformation and equal to 5.5. Therefore mean force of the foam-filled tube can be calculated as:

$$P_{mean} = P_{tube} + \sigma_f \, a \, b + C_{avg} \sqrt{\sigma_f \ \sigma_0} \ \ c \, t \qquad \textbf{(2.15)}$$

Studies showed that there are significant enhancements in the energy absorption behavior of the foam-filled tubes compared to the non-filled ones.

2.3 Composite and Hybrid Energy Absorbers

Modern industrial design has recently changed with the invention and use of composite materials, along with technological advancements. They are highly preferred in equipment and construction systems because they may be made according to the intended application, contain the characteristics of the parts that make it up, and exhibit greater strength and performance. Due to their superior mechanical properties, fiber-reinforced composites are produced in the form of plates.

A high strength-to-weight ratio makes composite structures increasingly popular in automotive applications. Composite materials have been studied to understand their energy absorption mechanisms. Experiments were conducted to find the material with the best energy absorption characteristics based on different materials, lay-ups, and manufacturing processes. Composite materials have challenging crushing mechanisms and energy absorption systems, which led researchers to begin experimental investigations first.

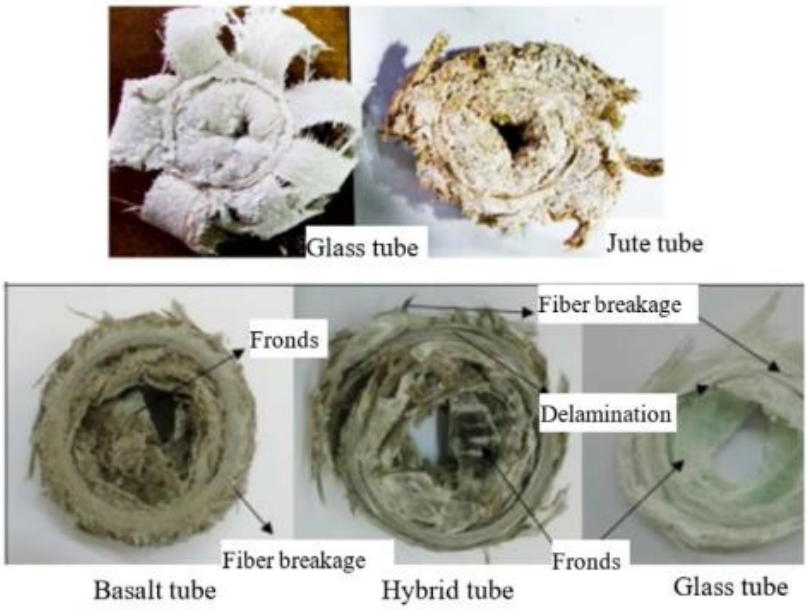

Figure 2.6 Axial crashing modes of composite tubes [60]

Fiber-reinforced composites show brittle fracture behavior and damage occurs due to fiber breaks as a result of the impact. These fractures also cause the initiation and propagation of damage on surfaces, and delamination damage as shown in Figure 2.6. Similar crushing behaviors are observed for the hybrid tubes fabricated with metal tubes externally wrapped with GFRP as shown in Figure 2.7.

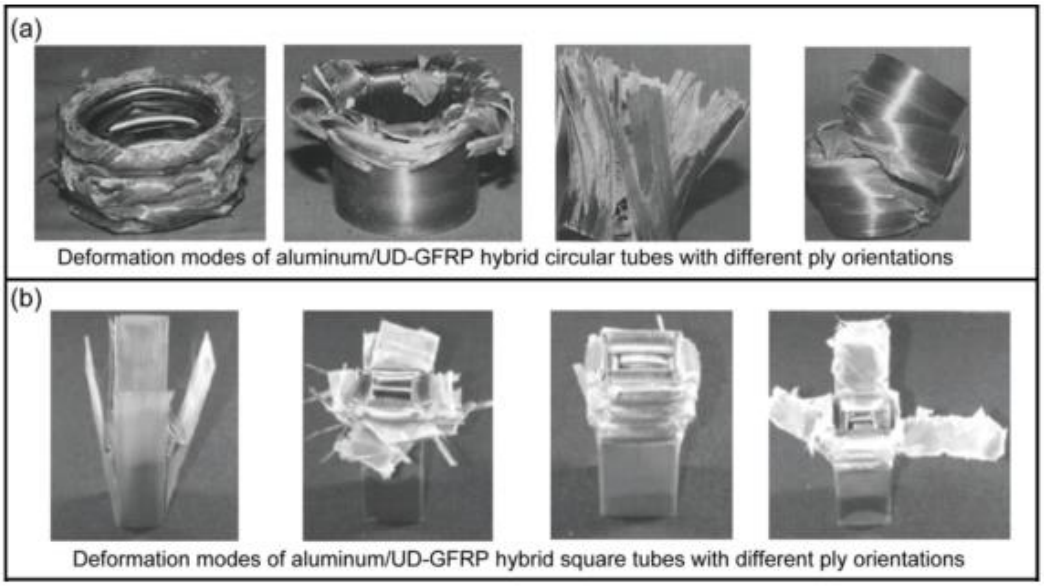

Figure 2.7 Axial crashing modes of hybrid tubes (a) circular tubes (b) square tubes [60]

2.3.1 Factors affecting energy absorption

The suitability of composite materials is determined by their impact properties as well as their energy absorption properties. The usual design parameters are taken into account when choosing the proper composite material. A composite structure's crashworthiness capability is impacted by its constituent phases and laminate layup because it transforms its mechanical properties. Material crashworthiness is also affected by temperature, which has a considerable impact.

When composites are investigated for impact strength, several elements play a role. Influence of fiber (type and characteristics) on composite materials is one of the variables. The local stress distribution during the impact could be defined by adjusting the fiber stiffness. Additional parameters influencing composite impact performance include volume percentage, fiber arrangement, and stacking sequence [61]. Geometry, layer order, matrix, and fiber characteristics, are only a few of the factors that affect fracture behavior and energy absorption performance.

2.3.1.1 Composite design

Composites have been produced using various methods that were created to meet certain design or application requirements. The right approach depends on the component design and the material characteristics. The type of fiber and resin used greatly influence the energy-absorbing properties of fiber-reinforced plastic (FRP) thin-walled tubes. In general, fiber reinforcement can be made of natural or synthetic materials, and the resin can be either thermosetting or thermoplastic. Fiber layouts such as uni-direction, woven fabric, and braided fiber reinforcement significantly influence the crushing behavior of FRP thin-walled tubes [60].

Fiber-reinforced composite materials consist of two or more components, fibers (carbon, aramid, glass) and matrices (epoxy, vinyl ester, polyester). Fibers are the main load-bearing elements, while matrices provide load transfer between fibers. Composite materials can be designed to meet the requirements by combining different fibers and matrices. Glass fiber composites are used in aviation, space, defense industry, etc. due to their higher durability, electrical resistance, and acid corrosion resistance. Glass

fibers are widely used due to their high tensile strength, high resistance to heat and moisture, and cheap cost. Glass fibers are available in the form of dry fiber cloth or prepreg [4].

The kind of material utilized and the laminate design were investigated to improve the crashworthiness of composite tubular components. Formerly, thermosetting resins such as epoxy were combined with carbon, glass, or aramid fibers to create composites. The most frequently employed energy absorbers are fabric-reinforced polymers because of their capacity to absorb energy.

In addition to combining different matrices and fibers, composite materials can also be produced by stacking in different directions to achieve the desired strength and stiffness. Unidirectional composites have maximum mechanical properties in the fiber direction. In fiber-reinforced composites, it is possible to obtain optimum mechanical properties in the desired direction by changing the fiber direction.

To form the resin and reinforcement, dies, molds, and mandrels are typically used for the composite fabrication procedures. Hand layup is a typical fabrication technique for crashworthy components, notably for thermoset composites. The hand layup technique involves stacking dry fabric layers, or plies, to produce a laminate. After the layup is complete, resin infusion is used. There are three types of hand lay-up wrapping: roll wrapping, wet wrapping, and hand lay-up wrapping. Various type of resin is suitable for composite production by methods such as hand lay-up, spraying, and vacuum infusion. Due to its different chemical structure than standard polyester and epoxy resins, vinyl ester has a much higher heat and chemical resistance [4].

2.3.1.2 Structural Design and Trigger Mechanism

Modern automobiles have a primary structure made of sophisticated composites, which presents some challenges for designers working to ensure occupant safety and crashworthiness. Due to their mechanical capabilities, fiber-reinforced plastic composite materials are used more frequently in automotive structures. Advanced composite vehicle designs must fulfill the criteria for crash certification in order to be a competitive design feature. Due to the sophistication of the crush failure

mechanisms, it is challenging to estimate the energy absorption produced by composite structures. Energy absorption tubular structures were designed in circular, square, and cone shapes to absorb big amounts of energy while progressively collapsing after impact.

In order to prevent catastrophic crushing, trigger systems are used in composite structures. The triggering mechanism provides progressive collapse and prevents load transfer to the entire component. As a result of diverse fracture mechanisms, including splaying, fracture modes, etc., an appropriate selection of triggering results in progressive crushing.

2.3.2 Experimental Investigations

Various failure mechanisms and energy absorption properties are obtained from the static and dynamic experiments. The effects of cross-section and material type are examined based on the identified crash behavior and energy absorption characteristics.

To absorb more energy while deforming progressively or catastrophically, circular, square, and cone composite components were used in automobile applications. Experimental research on the energy-absorbing properties of pultruded GFRP tubes subjected to axial dynamic loading was conducted by Palanivelu et al. [62] and Guades et al. [63]. In the experimental investigation by Guades et al. [63], the effects of loading parameters, such as the mass of the impactor, incident energy, and the number of impacts, on the crushing behavior of square pultruded GFRP tubes under repeated axial impacting conditions were evaluated. In the pre-collapse zone, the number of impacts significantly influenced the peak load evolution; however, in the post-collapse region, its influence is less pronounced.

The effect of temperature on the crashworthiness of GFRP tubes with circular cross-sections and foam filler within was examined by Wang et al. [64]. They collapsed brittle at temperatures between 20° and 50°C. The most absorbed energy can be achieved at temperatures as low as 50°C, according to experiments. The test environment's rising temperature had an adverse effect on the vehicle's capacity to withstand crashes. The crush force efficiency of the tube was increased by using foam

with a [0/90] fiber orientation angle and higher density for the GFRP structure. The effects of geometry and trigger type on the properties of energy absorption were assessed by Palanivelu et al. [65]. They studied single- and double-ply polyester resin tubes made by hand-laying up polyester resin. When compared to tubes with tulip triggers, the tubes with a 45° chamfer trigger performed with a higher peak force. Tubes with a square or hexagonal shape are distorted catastrophically. This study demonstrated how the geometry and the triggering mechanism significantly affect the SEA and crush efficiency. Additionally, to improve the crashworthiness of tubes, researchers investigated the capabilities of GFRP tubes with filler. PU foam filler's effectiveness in composite tubes was studied by Wang et al. [66], Othman et al. [67], and Chen et al. [68]. PU foam-filled GFRP tubes absorbed energy more than foam-filled Al tubes, according to research by Wang et al. [66]. The density of the foam had no effect on peak load, though. Compared to tubes with a [45] fiber orientation, tubes with a [0/90] fiber orientation showed a higher peak force. Square tubes fabricated of an E-glass/polyester composite were put through axial and oblique tests by Othman et al. [67]. The findings of the experiments showed that the composite tube filled with PU foam performed better crashworthiness than the empty composite tube. When the angle of the oblique load increased, they also noticed a drop in the mean force and absorbed energy. Lattice frame reinforcement for the GFRP tube with foam filler was suggested by Jin et al. [69] in their study. According to the study, syntactic foam and lattice frames increased energy absorption by 90%. Additionally, a mathematical model that forecasts the peak force in accordance with the outcomes of the experiments was proposed. A multi-cell geometry, epoxy resin-filled, syntactic foam core GFRP tube was tested by Wang et al. [70]. Results indicated that raising the number of the webs of GFRP tubes from 0 to 4 increased energy absorption by 48%.

In terms of cost and enhanced crashworthiness performance, the benefits of hybrid tubes were examined. Circular metal tubes wrapped with a glass/epoxy composite to create hybrid tubes were the subject of studies by Mirzaei et al. [71] and Song et al. [72]. The effects of orientation on the deformation process of aluminum/GFRP tubular sections were investigated by Mirzaei et al. [71]. They investigated an analytical model that accurately forecasts the mean force and folding length. The crashworthiness behavior of cylindrical metal tubes coated in glass/epoxy under dynamic loading was

investigated by Song et al. To evaluate the effects of the ply orientation, the specimens were constructed with $[15]_3$, $[45]_3$, and $[90]_6$ orientation by winding-up procedure. For the tubes with $[90]_6$ orientation, a higher energy absorption efficiency was obtained. Under quasi-static circumstances, Shin et al. [73] tested GFRP-wrapped aluminum tubes with [0], [90], [0/90], and [45] orientations. The tube with the [90] ply orientation has the highest energy absorption. Because of the composite covering, the aluminum tube did not fold during compression. In comparison to aluminum tubes, the hybrid tubes performed better in terms of mean force and absorbed energy. Tarafdar et al. [74] evaluated the performance of hybrid sandwich tubes with multi-cell geometry and hierarchical cores inside. They compared hybrid tubes consisting of Al and GFRP tubes under quasi-static loading. In Al tubes, the load declines after the peak force is observed and fluctuates at a lower mean force compared to GFRP tubes. The composite tube performed higher crush force efficiency than the Al tube. The crashworthiness performance of the GFRP tube increased when the crush length increased. Experimental research on the empty and epoxy foam-filled hybrid tubes with circle and square sections was conducted by Babbage and Mallick [75]. Investigations were done into how filler, composite thickness, and stacking order ([45] or [75]) affected the ability to absorb energy. The maximum amount of energy was absorbed by the hybrid circle tubes with foam filler and the thickest composite wrap. The effects of foam filling on the tubes when subjected to axial loading were examined by Guden et al. [76]. The force-displacement curve of the composite tubes was unaffected by foam. The total of crush force values of empty metal and composite tubes was less than the crush force values of empty hybrid sections. Although the foam filling caused the composite wrap to crack axially, crash force and energy absorption values were unaffected.

2.3.3 Numerical Investigations

The finite element method is a widely accepted alternative to overpriced tests for a variety of constructions, even though it requires validation for some complicated physical problems. Finite element analysis has recently been a popular method used by researchers to model and understand the energy absorption behavior of composite structures. It was necessary to conduct detailed analyses due to the complicated failure

mechanism of composite tubular sections. Composite materials are damaged by a mixed order of interrelated damage mechanisms such as fiber breakage, matrix breakage, and delamination. These are difficult to calculate numerically due to the complex nature of fracture behavior in composite materials. In order to do this, a variety of fundamental models, delamination methods, and damage initiation mechanisms are researched.

A commercial composite model can simulate composite crushing behavior by determining material characteristics using compression and tension tests. Using a finite element program subroutine from a commercial program, material models are improved to be more compatible with experimental results. The main purpose of composite damage modeling is to predict crush damage modes and evaluate its behavior during the crash.

With the developing computer technology, it has become almost mandatory to use finite element software in the market to calculate the mixed damage behavior of composite materials in a crash. By using the frequently preferred ABAQUS, Ls-Dyna, and RADIOSS finite element software, the numerical model of the sample used in the relevant experimental studies is created. Each layer in the sample is modeled with appropriate elements, and adhesive elements are defined between the layers to accurately model the deformation process.

The crash behavior of top-hat structures was quantitatively studied by Subbaramaiah et al. [77] using material model 54 in Ls-Dyna. FE model results and experiment responses were found consistent. El-Hage et al. [78] used material model 54 in Ls-Dyna to model hybrid square tubes constructed of aluminum and GFRP under axial loading. They focused on the tubes with fiber orientations ranging from [30] to [90]. The hybrid tube with a [90] stacking sequence displayed the greatest absorbed energy values. When it came to crushing resistance, the thinner aluminum tubes were more crashworthy than the thicker ones. Although the hybrid tubes had superior EA performance than the aluminum tubes, their SEA values were equal or lower. Using the material model 54 in Ls-Dyna, Han et al. [79] assessed the energy absorption behavior of hybrid tubes. They explored the deformation of hybrid tubes under quasi-

static and axial dynamic impact stresses. While deforming in the accordion type, the hybrid tubes absorbed energy. The $[0]_4$ orientation tube absorbed the most energy of any tube. Length, composite thickness, and loading condition had an impact on energy absorption. Zhang et al. [80] studied the effects of tube filler, tube shape, and tube thickness on the SEA of GFRP, metal, and hybrid tubes. Al foam filling in GFRP tubes didn't work as well as polyurethane foam filling. In the study, foam filler did not alter the failure mode of GFRP tubes.

Siromani et al. [81] simulated the crushing behavior of circular composite tubes with chamfer and combined failure trigger mechanisms using Ls-Dyna. Tong and Xu [82] introduced a chamfer external trigger restricting the space of the tube under compression by a semi-circle cavity to model the response of [0/90] biaxial braided circular tube under dynamic axial loading conditions. To simulate the failure, the circular tube was simulated by multi-layer shell elements with tie break contact definition of Ls-Dyna. Boria et al. [83, 84] reported the energy absorption capacity of composite conical and square thin-walled impact attenuators. FE model was implemented in Ls-Dyna with a multi-layered model to capture the deformation process. The increase in wall thickness affected energy absorption performance significantly.

McGregor et al. [85] simulated the axial crushing of square composite tubes with and without an external plug initiator in Ls-Dyna to model the failure mechanisms. Two-ply and four-ply square tubes were modeled using continuum damage mechanics (CDM) based model for composite materials in Ls-Dyna. Cherniaev et al. [86] investigated the predictive capabilities of composite material models – MAT054, MAT058, and MAT262 – of axial crushing of square CFRP energy absorbers with rounded corners and bevel-shaped crush initiators. Ying et al. [87] presented the axial collapse of fiber-reinforced tapered square metal thin-walled structures using Ls-Dyna. The effects of fiber orientation, wall thickness of fiber layer, and tapered angle of square tubes on the energy absorption of the tubes were investigated. Liu et al. [88] evaluated the effects of hole size, hole shape, and hole distribution on failure modes and mechanical behaviors of the square weave carbon fiber reinforced polymer (CFRP) tubes with open holes subjected to axial compression in Ls-Dyna. Shi et al.

[89, 90] developed a new shell-beam (SB) element method and pre-failure and post-failure model to improve the stability of triaxial braided composite square tubes. The enhanced continuum damage mechanics model using two sub-models with separate damage evolution laws for the pre-failure and post-failure regions was implemented as a user defined material model in Ls-Dyna. They modeled most of the damage modes and absorption responses of tubes in the longitudinal direction with and without a plug initiator. Zhang et al. [80] compared the crashworthiness of the tapered hollow, foam-filled composite, and hybrid tubes with single-shell and double-shell element models. Results of the circular tube specimen simulated in Ls-Dyna using Chang-Chang failure criterion were found consistent with the experimental data. SEA of circular tubes was found higher than the tapered and square tubes for hollow composite tubes. Although SEA was influenced negatively when the foam density was increased, low density foam filling could improve the energy absorption performance of GFRP tubes.

Studies showed that tubes with a large number of composite plies and short lengths exhibit larger peak loads. An increase in the number of plies enhances the energy absorption performance of the composite tubes. The number of composite layers is important for the energy absorption of the hybrid tubes. The hybrid configuration offers a higher energy absorption capacity for meeting crashworthiness requirements.

CHAPTER 3

NUMERICAL AND THEORETICAL ANALYSIS OF ALUMINUM TUBES

Extensive effort has been performed on understanding the effects of geometrical parameters and material types on the energy absorption performance of thin-walled tubes. Although quite a little research has been done on the axial crushing behavior of empty and foam-filled aluminum multi-cell tubes for a desirable crushing performance, the numerical investigation of multi-cell tubes with aluminum-based metallic foam is aimed in this thesis. The goal of the current study is to model the failure behavior of multi-cell tubes consistent with the experimental results of the Al 6061 tubes tested by Murat Altın [42].

3.1 Results of Experiments

The empty and aluminum-based metallic foam-filled tubes that were used in the experimental studies contained a rectangular cross-section. These tubes were made of aluminum alloy 6061-T6 with a cross-section of 71.5 mm x 86.5 mm, a wall thickness of 1.5 mm, and a length of 180 mm. Multi-cell tube T4E was designed by putting square tubes to the corners of a single-cell tube after it had been divided by four. Multi-cell tube T8E was designed by putting rectangular tubes to the corners of a single-cell tube after it had been divided by two. Also, the rectangular tubes in the middle part were divided into two tubes to create the multi-cell tube T8E. An image of the geometry of the tubes used in the experiments is shown in Figure 3.1.

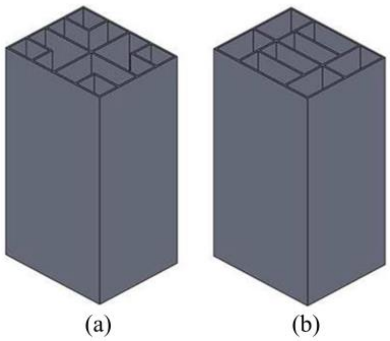

Figure 3.1 Geometry of the Multi-cell Tubes (a) Tube T4E (b) Tube T8E [42]

The tubes were manufactured using the wire erosion process to ensure the accuracy of the measurements in the thesis of Murat Altın [42]. An image of the empty and foam-filled multi-cell tubes used in the experiments is shown in Figure 3.2.

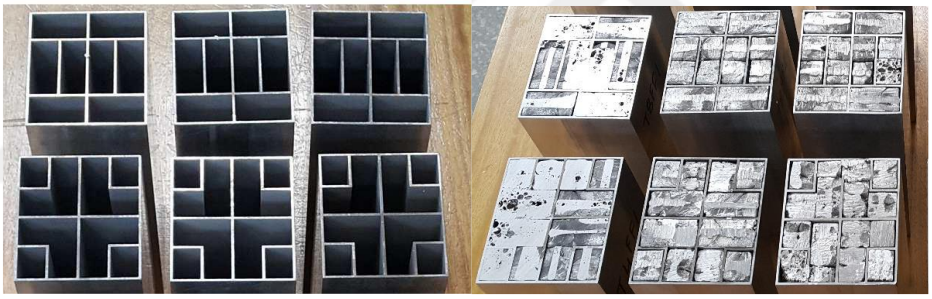

Figure 3.2 Empty and foam-filled test specimens for T4E and T8E tube configurations [42]

The deformation speed of the rigid plate was 2 mm/min in the quasi-static tests. Tubes were deformed until their half length (90 mm). The identical tests were carried out on three different specimens with the same cross-section to ensure the repeatability of the experiments. The deformation images of the T4E tubes against the applied load within 45 minutes are given in Figure 3.3 [42].

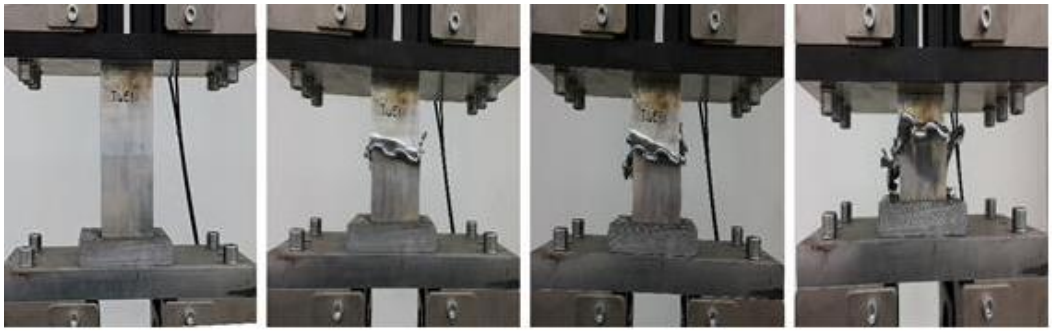

x=0 x=30 mm x=60 mm x=90 mm

(a)

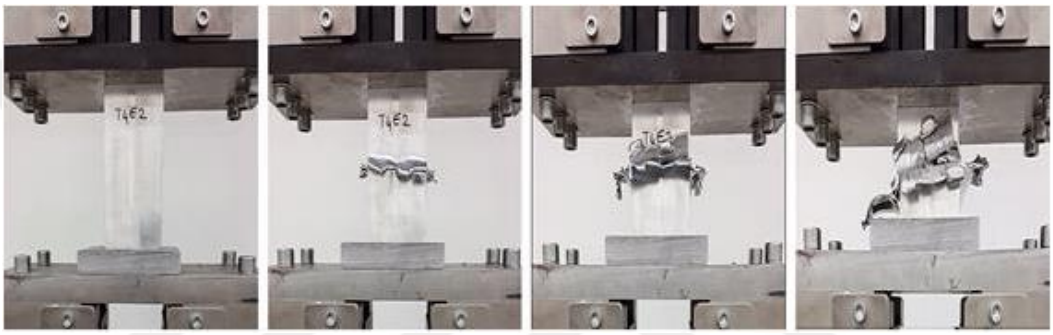

x=0 x=30 mm x=60 mm x=90 mm

(b)

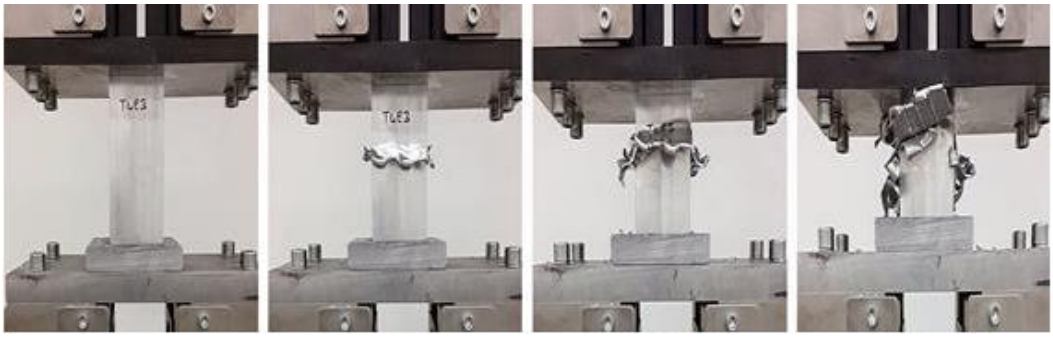

x=0 x=30 mm x=60 mm x=90 mm

(c)

Figure 3.3 Progressive failure behavior of multi-cell test specimens (T4E) at different stages: x= 0 mm, x = 30 mm, x = 60 mm, x = 90 mm (a) test specimen T4E1(b) test specimen T4E2 (c) test specimen T4E2 [42]

The deformation in T4E tubes started in the middle parts. With the continuation of the loading, it was observed that cracks started to occur in the middle parts of all T4E tubes after the deformation distance of 20 mm. The force-displacement graphs obtained from the experiments of empty multi-cell T4E tubes are given in Figure 3.4.

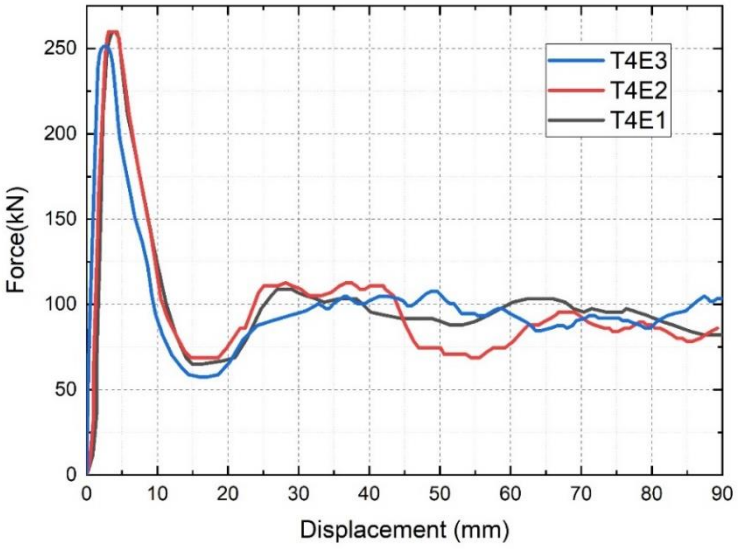

Figure 3.4 Force-displacement graph of T4E multi-cell test specimens [42]

The peak force occurs around 250 kN in T4E tubes. After the peak force, the crash force decrease to 60 kN. Split in the corners and rupture of the tubes cause the crash boxes not to deform by progressive folding. The crash force fluctuates between 50 kN and 125 kN until the end of the deformation. The decrease of crash force after the peak force causes limited energy absorption. By using the load-displacement graphs in Figure 3.4, the energy absorption parameters of the T4E tubes are calculated.

The identical tests were carried out on three different specimens with the same-cross section for T8E multi-cell tubes. The deformation images of the T8E tubes under the axial load within 45 minutes are given in Figure 3.5.

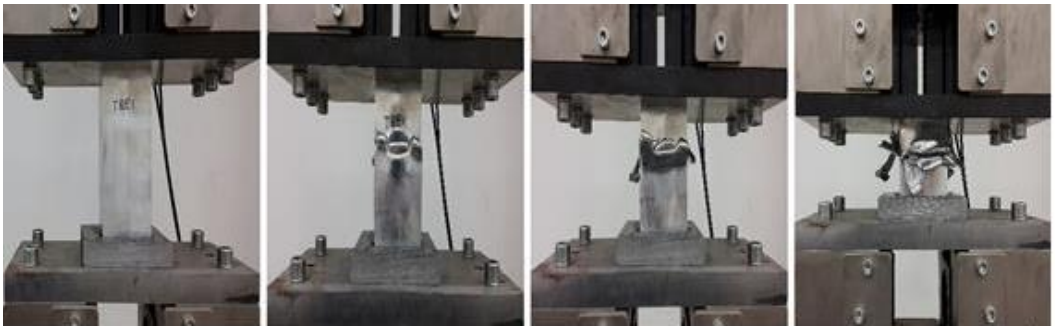

x=0 x=30 mm x=60 mm x=90 mm

(a)

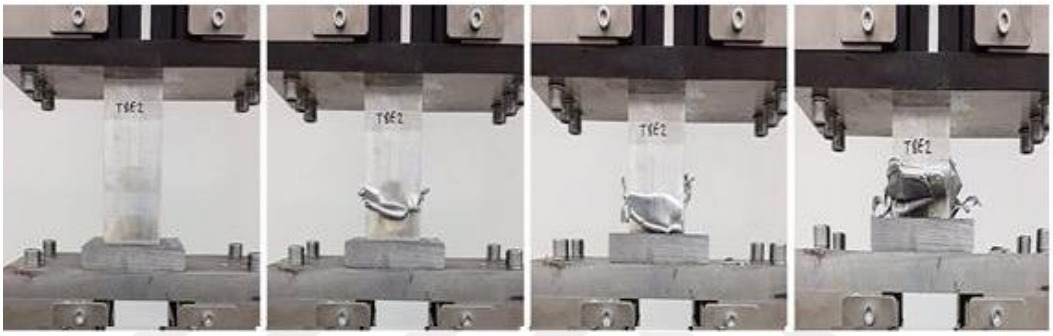

x=0 x=30 mm x=60 mm x=90 mm

(b)

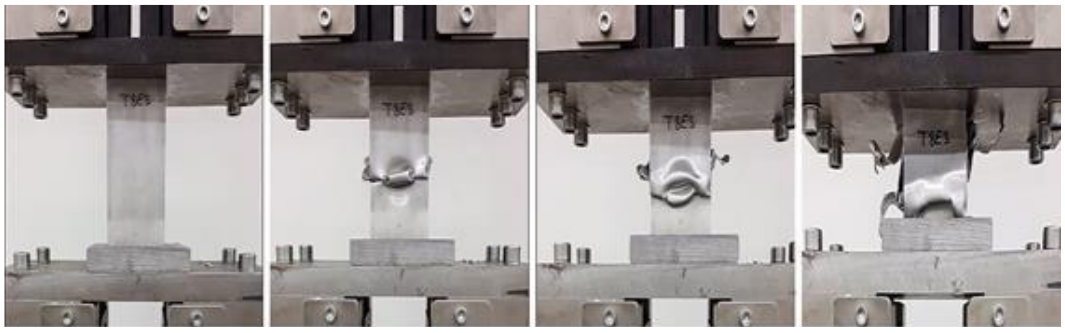

x=0 x=30 mm x=60 mm x=90 mm

(c)

Figure 3.5 Progressive failure behavior of multi-cell test specimens (T8E) at different stages: x= 0 mm, x = 30 mm, x = 60 mm, x = 90 mm (a) test specimen T8E1(b) test specimen T8E2 (c) test specimen T8E3 [42]

Cracks begin to form in the middle parts of T8E multi-cell tubes, as in T4E multi-cell tubes, after a deformation distance of approximately 20 mm. Due to these cracks, rupture and splitting begin in the middle of the tubes.

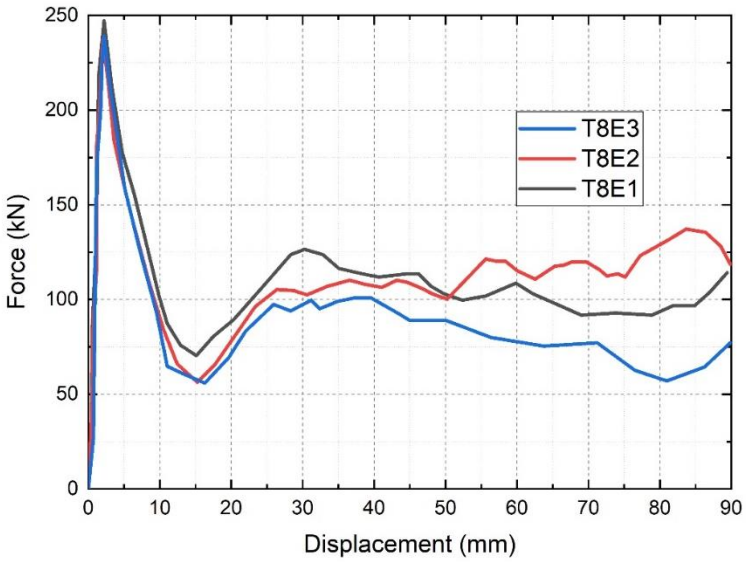

Figure 3.6 Force-displacement graph of T8E multi-cell test specimens [42]

The peak force occurs around 250 kN similar to T4E multi-cell tubes. After peak force, a decrease to 60 kN in the crash force is observed and the crash force fluctuates between 50 kN and 125 kN until the end of the deformation. By using the load-displacement graphs in Figure 3.6, the energy absorption parameters of the T8E multi-cell tubes are calculated.

Altın [42] inserted the aluminum foam material into the empty T4 and T8 multi-cell tubes to compare the effect of foam on the energy absorption performance. Aluminum alloy foam (AlMg1Si0.6TiH20.8) with a density of 0.628 g/cm^3 was placed inside the tubes. Similar quasi-static axial tests were carried out for foam-filled multi-cell tubes. As in the empty multi-cell tube tests, no change was made in the test conditions and the compression velocity was determined as 2 mm/min. The deformation images obtained within a compression distance of 90 mm for foam-filled T4 multi-cell tubes, which are named T4FF, are given in Figure 3.7.

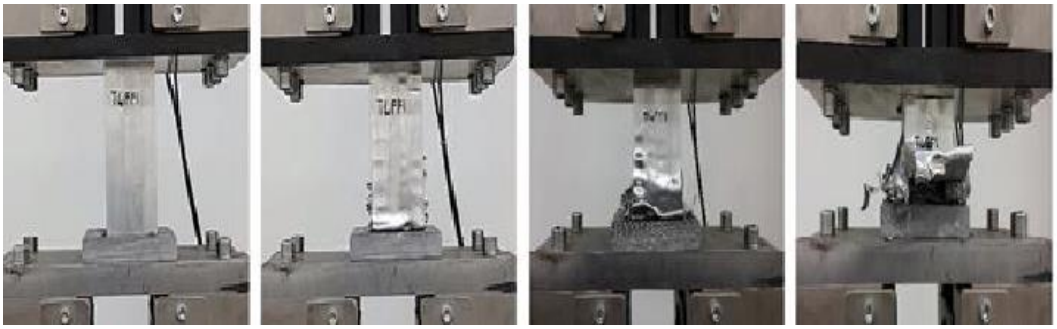

x=0 x=30 mm x=60 mm x=90 mm

(a)

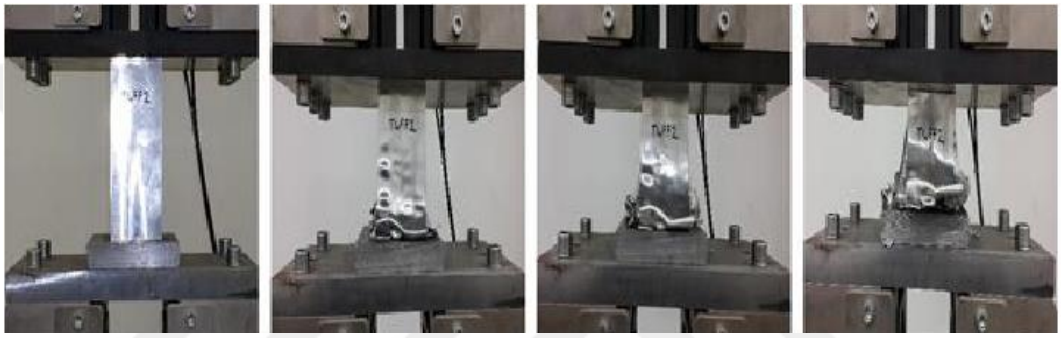

x=0 x=30 mm x=60 mm x=90 mm

(b)

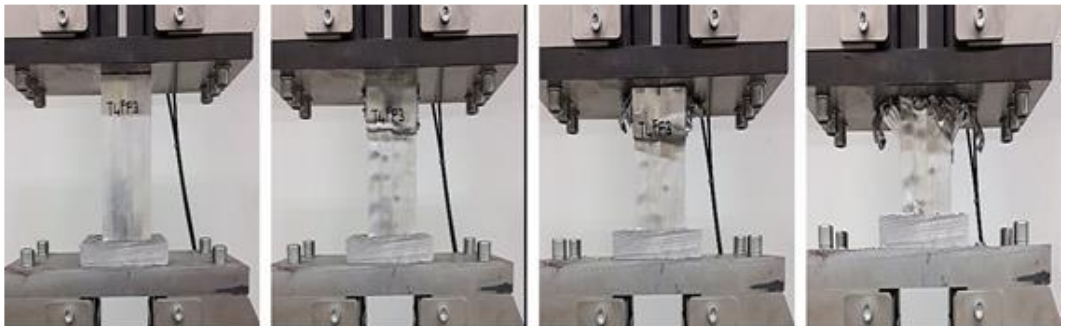

x=0 x=30 mm x=60 mm x=90 mm

(c)

Figure 3.7 Progressive failure behavior of multi-cell test specimens (T4FF) at different stages: x= 0 mm, x = 30 mm, x = 60 mm, x = 90 mm (a) test specimen T4FF1(b) test specimen T4FF2 (c) test specimen T4FF3 [42]

The force–displacement graphs obtained from the experiments of foam-filled multi-cell T4FF tubes are given in Figure 3.8. The peak force occurs around 325 kN in T4FF tubes. After this force, a decrease to 175 kN in the crash force is observed. Split and ruptures of the tubes cause the crash boxes not to deform by progressive folding. By using the load-displacement graphs in Figure 3.8, the absorbed energy amounts of the T4FF tubes are calculated.

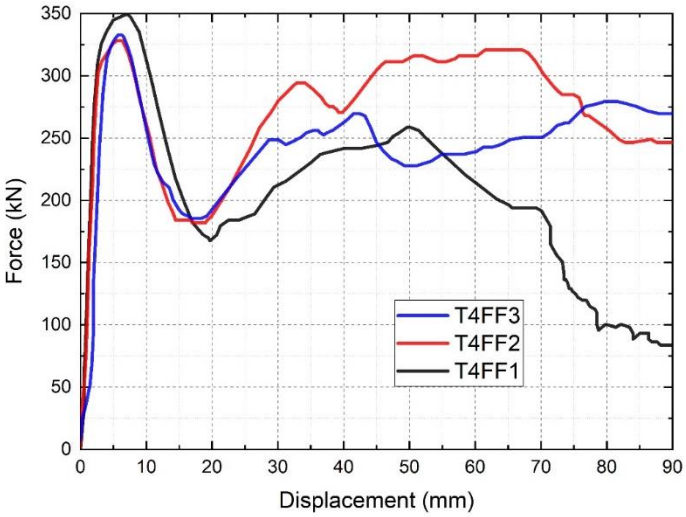

Figure 3.8 Force-displacement graph of T4FF multi-cell test specimens [42]

The deformation images obtained within a compression distance of 90 mm for foam-filled T8 multi-cell tubes, which are named T8FF, are given in Figure 3.9.

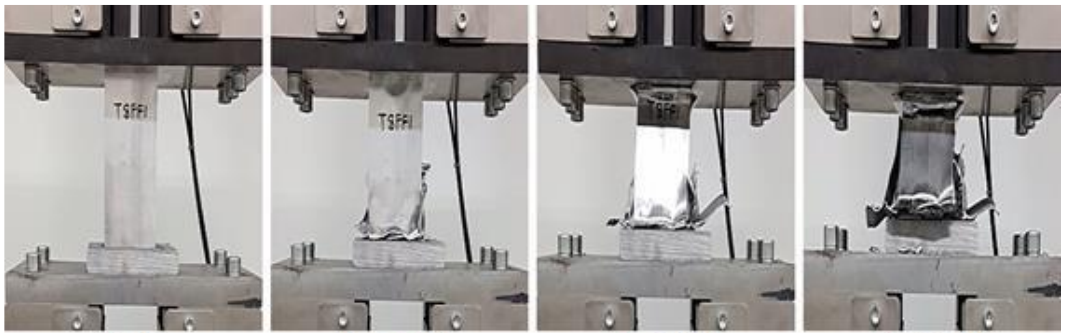

x=0 x=30 mm x=60 mm x=90 mm

(a)

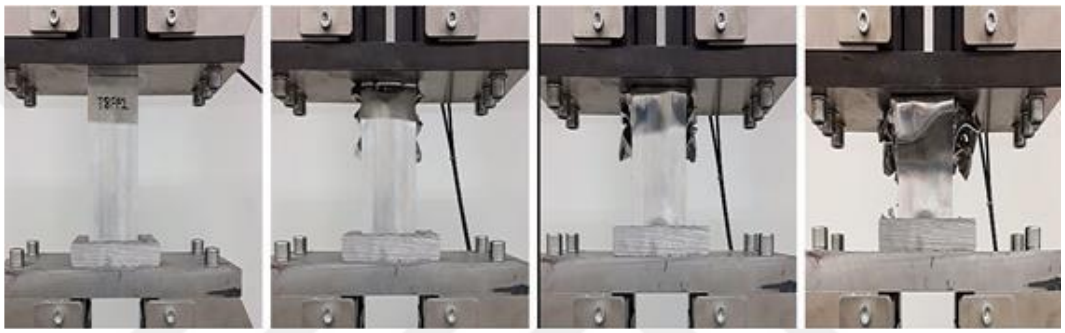

x=0 x=30 mm x=60 mm x=90 mm

(b)

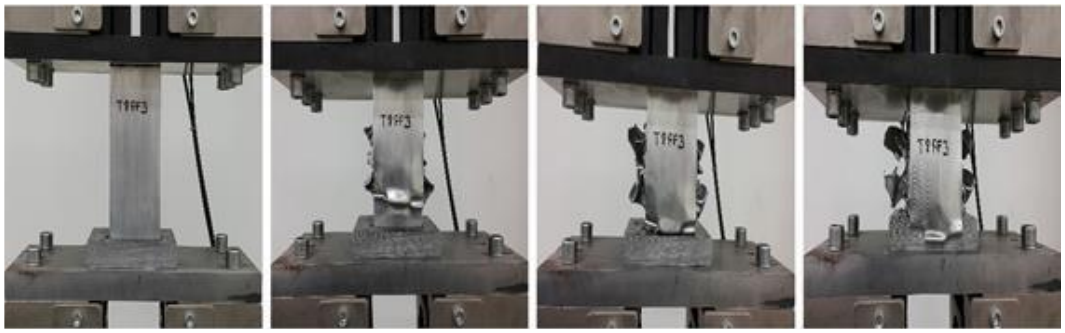

x=0 x=30 mm x=60 mm x=90 mm

(c)

Figure 3.9 Progressive failure behavior of multi-cell test specimens (T8FF) at different stages: x= 0 mm, x = 30 mm, x = 60 mm, x = 90 mm (a) test specimen T8FF1(b) test specimen T8FF2 (c) test specimen T8FF3 [42]

As can be seen from the pictures, T8FF multi-cell tubes start to fold from the middle after the peak force is reached. Tears begin to occur in the corners, as in other multi-cell tubes. This type of folding results in less energy absorption than predicted. The load-displacement graphs for foam-filled T8FF multi-cell tubes are given in Figure 3.10. The test was terminated for specimen 1 when the deformation distance was 80 mm since the tube T8FF1 entirely collapsed.

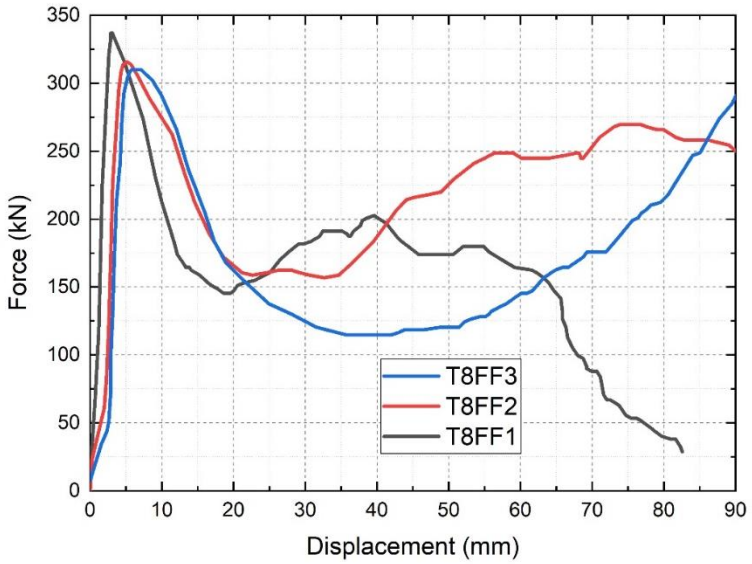

Figure 3.10 Force-displacement graph of T8FF multi-cell test specimens [42]

3.2 Numerical Analysis of Aluminum Tubes

3.2.1 Material Model

The material model of the aluminum tube is defined with MAT_18 (MAT_POWER_LAW_PLASTICITY) and the aluminum-based metallic foam material is defined with the MAT_154 (MAT_DESHPANDE_FLECK_FOAM) material card in Ls-Dyna [91].

In this material model, the aluminum tube is modeled with elastoplastic behavior with isotropic hardening. The yield stress, σ_y, is a function of plastic strain and obeys the equation:

$$\sigma_y = k\,\varepsilon^n = k\left(\varepsilon_{yp} + \bar{\varepsilon}^p\right)^n \quad \textbf{(3.1)}$$

where ε_{yp} is the elastic strain to yield and $\bar{\varepsilon}^p$ is the effective plastic strain. If σ_y is set to zero, the strain to yield is found by solving for the intersection of the linearly elastic loading equation with the strain hardening equation:

$$\sigma = E\,\varepsilon \quad \textbf{(3.2)}$$

$$\sigma_y = k\,\varepsilon^n \quad \textbf{(3.3)}$$

which gives the elastic strain at yield as:

$$\varepsilon_{yp} = \left(\frac{E}{k}\right)^{\left[\frac{1}{n-1}\right]} \quad \textbf{(3.4)}$$

If σ_y is nonzero and greater than 0.02 then:

$$\varepsilon_{yp} = \left(\frac{\sigma_y}{k}\right)^{\left[\frac{1}{n}\right]} \quad \textbf{(3.5)}$$

The material behavior of aluminum foam is modeled with a yield criterion:

$$\emptyset = \hat{\sigma} - \sigma_y \leq 0 \quad \textbf{(3.6)}$$

where $\emptyset$ denotes the yield surface, σ_y is the yield stress, and the equivalent stress and $\hat{\sigma}$ is expressed as

$$\hat{\sigma} = \sqrt{\frac{1}{\left[1+\left(\frac{\alpha}{3}\right)^2\right]}}\left({\sigma_e}^2 + \alpha^2\,{\sigma_m}^2\right) \quad \textbf{(3.7)}$$

where σ_e is the von Mises effective stress and σ_m is the mean stress, respectively. The yield surface is determined by using the parameter α:

$$\alpha^2 = \frac{9(1-2\vartheta^p)}{2(1+\vartheta^p)} \quad \textbf{(3.8)}$$

where ϑ^p is the plastic coefficient of contraction.

3.2.2 Model Setup

To model the axial crashing process of empty and foam-filled Al 6061 T6 tubes tested in Murat Altın's thesis [42] is aimed. The empty and aluminum foam-filled tubes tested in the experimental studies contained a rectangular cross-section. These tubes were made of aluminum alloy 6061-T6 with a wall thickness of 1.5 mm and a length of 180 mm. Numerical analyses are carried out using the commercial FE program Ls-Dyna to simulate the deformation process which includes splitting and tearing of the aluminum tubes. In the FE model, the aluminum tubes are discretized with shell elements, and foam is modeled with solid elements. The Al 6061 tube is subjected to axial loading and both the upper and lower platens are modeled as rigid parts as shown in Figure 3.11.

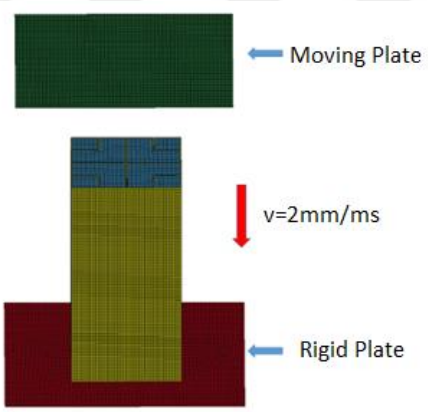

Figure 3.11 Finite element model of aluminum multi-cell rectangular tube

The boundary conditions are set as follows: the upper rigid wall is allowed to move only along the height of the tube and the lower rigid wall is constrained from all degrees of freedom.

The self-contact of the tube is modeled with the automatic single surface contact algorithm. The contact between the tube and other plates is modeled with the automatic surface to surface contact algorithm. The static and dynamic friction coefficients are taken as 0.3 and 0.2, respectively [92]. Also for foam-filled tubes, an automatic surface

to surface contact algorithm is used to simulate the contact between the aluminum foam and the multi-cell tube.

Fully integrated shell elements with five integration points through the thickness are employed to model aluminum tubes. To investigate the effect of mesh, different element sizes (2.0 mm, 2.5 mm, 3.0 mm, and 3.5 mm) are used to discretize the multi-cell T4E tube. Figure 3.12 shows the predicted mean forces of T4E multi-cell tubes for different mesh sizes. The convergence study shows that the element size of 2.5 mm is feasible for its acceptable accuracy and computational cost.

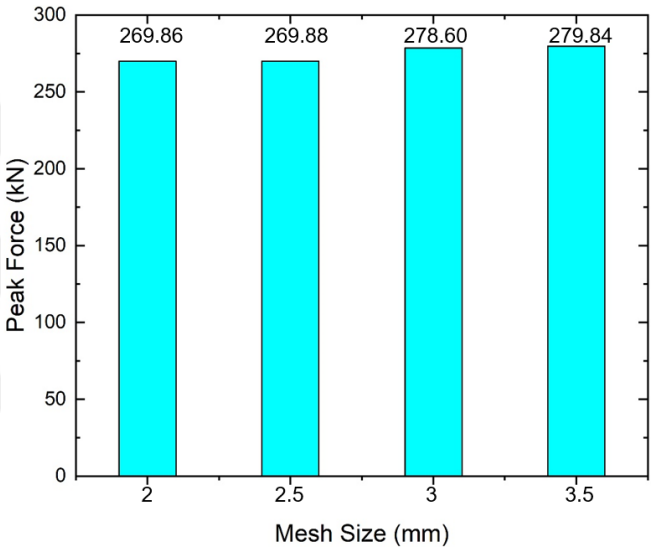

Figure 3.12 Mesh Analysis of tube elements for multi-cell rectangular tube

Constant stress solid elements (default) with hourglass control are employed to model aluminum foam. To investigate the effect of mesh, different element sizes (3.0 mm, 3.5 mm, 4.0 mm, and 4.5 mm) are used to discretize the foam. Figure 3.13 shows the predicted mean forces of multi-cell T4FF tubes for different mesh sizes. The convergence study shows that the element size of 3.5 mm is feasible for its acceptable accuracy and computational cost.

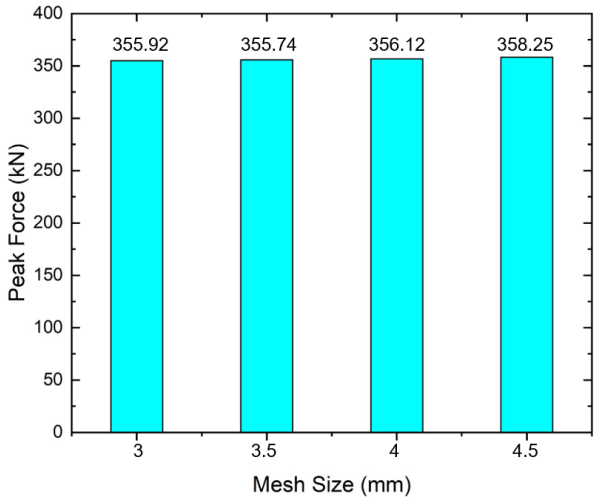

Figure 3.13 Mesh Analysis of foam elements for multi-cell rectangular tube

The rectangular tube material is Al 6061-T6. Tubes are modeled using a power law plasticity material model named MAT_18 in Ls-Dyna. The elastic properties are as follows: Young's modulus is 68.9 GPa; Poisson's ratio is 0.33, material density is 2700 kg/m^3, strength coefficient is 0.3788, hardening exponent is 0.050692 [93]. The plastic failure strain for element deletion is set to 0.48 applying a parametric study to validate experimental results.

The aluminum-based metallic foam material is defined with the MAT_154 material card in Ls-Dyna ignoring strain rate effects.

For aluminum foam, ϑ^p is equal to zero [42]. The current yield stress in Eq. (3.6) is expressed as following when α = 2.12 when ϑ^p = 0 [91]:

$$\sigma_y = \sigma_p + \gamma \frac{\hat{\varepsilon}}{\varepsilon_D} + \alpha_2 \ln\left(\frac{1}{1-\left(\frac{\hat{\varepsilon}}{\varepsilon_D}\right)^{\beta}}\right) \quad \textbf{(3.9)}$$

where σ_p is the plateau stress, and γ, α_2 and β are hardening parameters. The densification strain (compaction strain) is defined from uniaxial compression as [91]

$$\varepsilon_D = -\frac{9+\alpha^2}{3\,\alpha^2} \ln\left(\frac{\rho_f}{\rho_0}\right) \quad \textbf{(3.10)}$$

where ρ_f is the density of the foam material, and ρ_0 is the density of the column material.

Foam properties used in the simulations for the aluminum foam are listed in Table 3.1 [92].

Table 3.1 Foam properties used in numerical analyses [92]

ρ_f (g/cm^3)	σ_p (GPa)	α	α_2	β	γ (GPa)	ε_D	SIGP (GPa)
0.628	0.806	2.12	2.1273	9.66	0.0175	1.4584	0.015

By fitting the test data, one can determine the empirical constants that constitute the foam model's parameters. Altın et.al. [92] used a particle swarm optimization code in MATLAB software to find these constants by minimizing the deviation between the mathematical material model and the test data. Figure 3.14 depicts the curve fitting used to model foam with the density of 0.628 g/cm^3 [92].

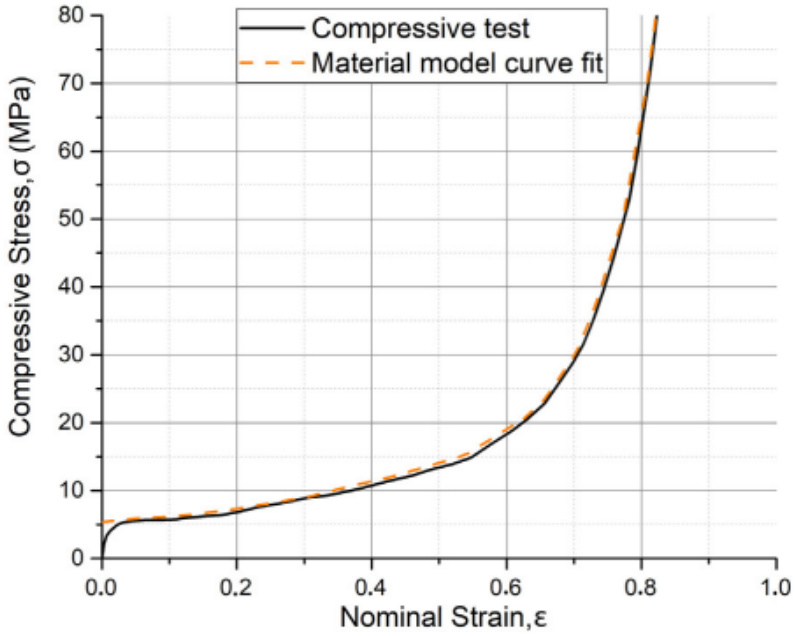

Figure 3.14 Curve-fit of analytical hardening curve to the experimental measurements [92]

3.3 Theoretical and Numerical Analysis of Aluminum Tubes

3.3.1 Empty Rectangular Tubes

3.3.1.1 FEM Results

A comparison of load-displacement curves obtained from the experiments and the FE model for T4 multi-cell tubes are provided in Figure 3.15. The images of the empty rectangular tubes during experiments and the finite element analysis are shown in Figure 3.16.

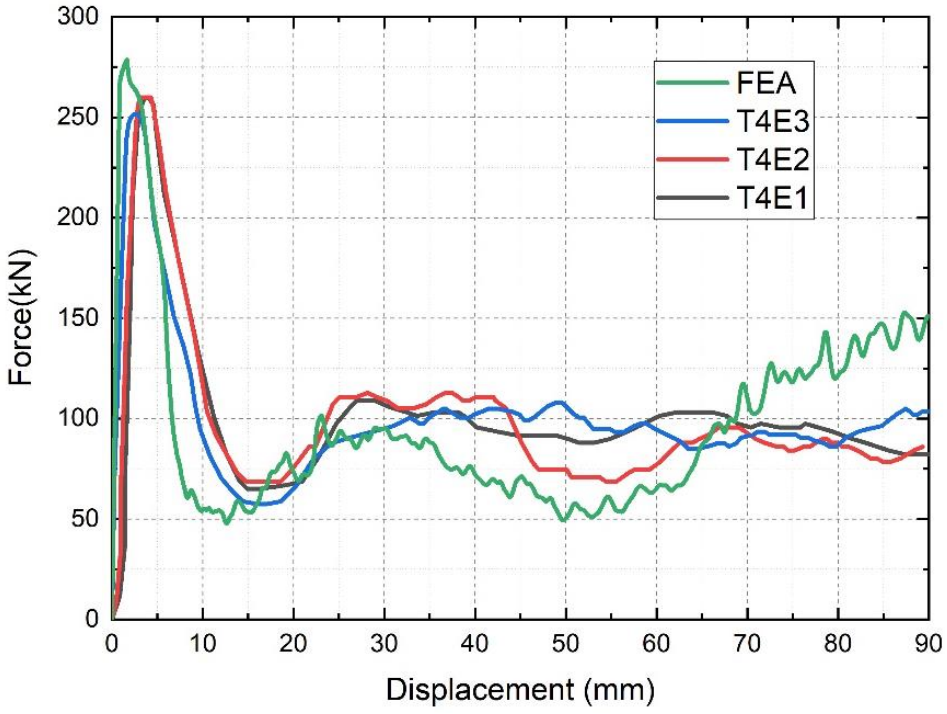

Figure 3.15 Comparison of load-displacement curves between the experimental study and FEA simulation for empty multi-cell T4 tubes

As can be seen in Figure 3.15, deformations start to occur in the tubes when the compression load reaches the level of approximately 250 kN. However, the cracks at mid height reduce the crash force after peak force is observed. Cracks cause force fluctuation between 50 kN and 125 kN. The deformation process of multi-cell T4E tubes taken at specific locations of deformation also displays unusual characteristics.

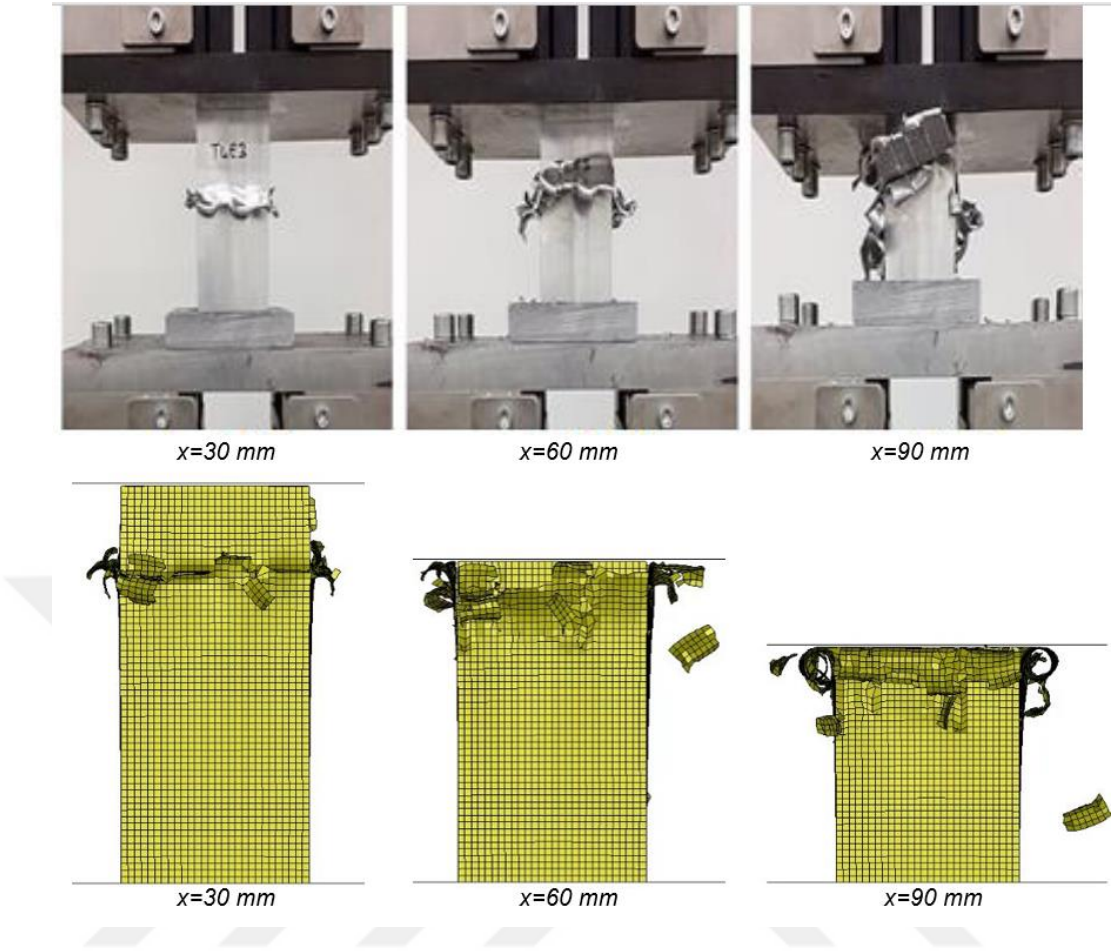

Figure 3.16 Comparison of collapse modes of empty T4 tubes between experimental and FEA results

After the deformation begins, tearing and splitting of the tube walls are seen at the specimens' midpoint in both experiments and the FE model. It is observed that the cracks on the tube cause the tubes to rupture and fail catastrophically after a while. At the end of the deformation period, the energy absorption amounts were calculated for the T4E multi-cell tubes using the load-displacement graphs which are given in Figure 3.15.

Table 3.2 Analysis Results of T4E Model

	Peak force (kN)	Mean force (kN)	CFE	EA (kJ)	Mass (kg)	SEA (kJ/kg)
TE1	259.87	102.56	0.39	9.230	0.447	20.649
TE2	259.87	97.98	0.38	8.818	0.446	19.771
TE3	251.20	99.94	0.40	8.995	0.436	20.630
Ave	256.98	100.16	0.39	9.014	0.443	20.350
FEA	269.88	93.98	0.35	8.458	0.452	18.712
Error (%)	5.02	-6.17	-10.26	-6.17	2.03	-8.05

The average EA of test specimens is 9.014 kJ, with a -6.17% error, as compared to the EA obtained via FEA, which is 8.458 kJ. The average SEA of test specimens is 20.350 kJ/kg, with a -8.05 % error, as compared to the SEA obtained via FEA, which is 18.712 kJ/kg. The FEA results deviate from the experimental results by 6.17%, 5.02%, −10.26% , and 8.05% for EA, IPF, CFE, and SEA for T4E tubes, respectively.

A comparison of load-displacement curves obtained from the experiments and the FE model for T8E multi-cell tubes is provided in Figure 3.17.

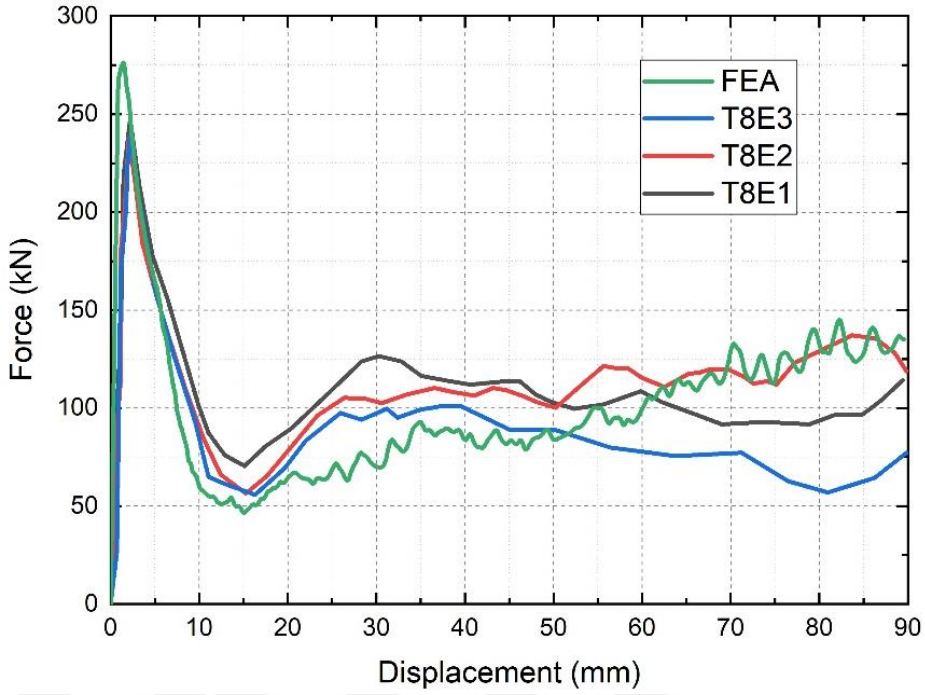

Figure 3.17 Comparison of load-displacement curves between the experimental study and FEA simulation for empty multi-cell T8 tubes

Figure 3.17 shows that when the crash force reaches around 250 kN, cracks begin to take place in the tubes. However, after the peak force is observed, the mid-height cracks lessen the crash force. Between 50 and 125 kN of force, variation is observed due to the cracks. The images of the deformed views of test specimen and the the finite element model are shown in Figure 3.18. Multi-cell T8E tubes also show unusual characteristics in their deformation process.

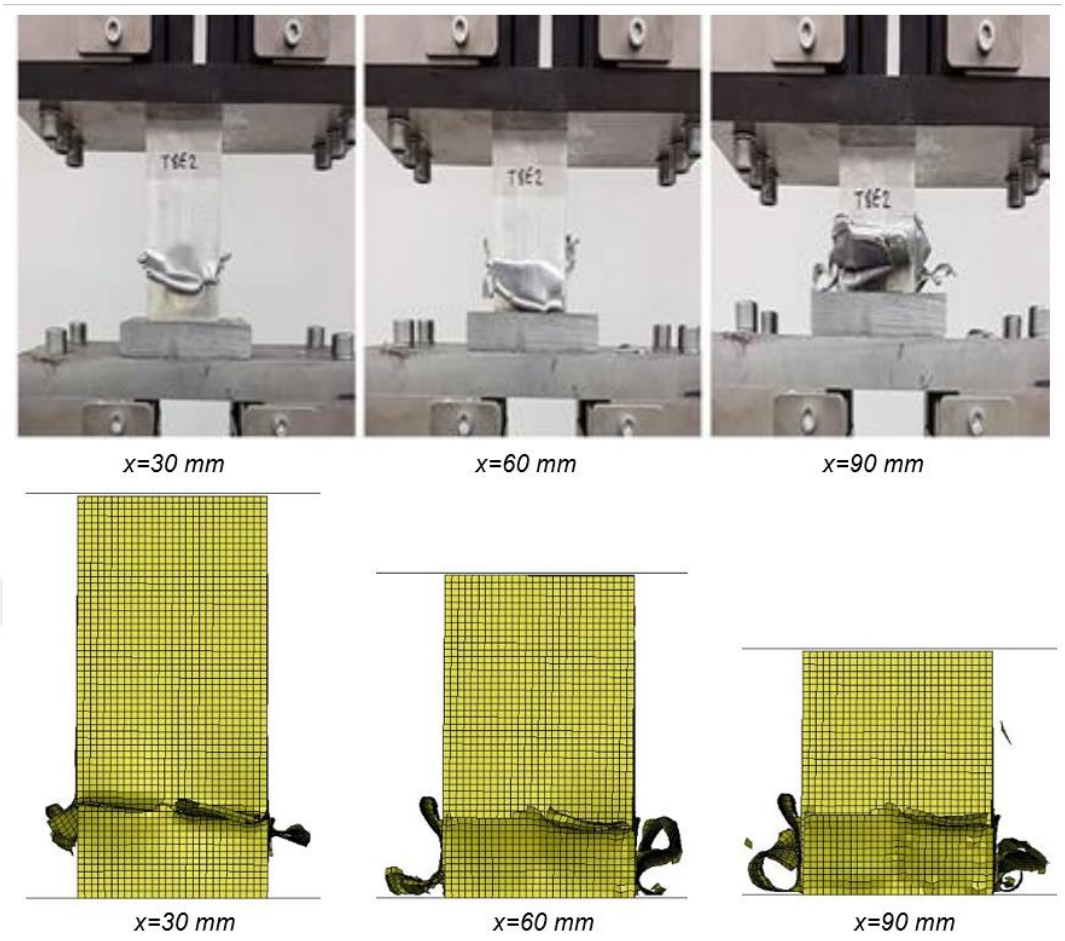

Figure 3.18 Comparison of collapse modes of T8E tubes between experimental and FEA results :(a) tests (b)FEM

The deformed shapes of the empty multi-cell tubes T4E and T8E obtained experimentally and numerically are presented in Figure 3.16 and Figure 3.18, respectively. They are seen to be similar, and the tube's center section experiences significant plastic deformation with just one fold. The numerical model successfully captures the fracture that occurs at the folded region's corners. At the end of the deformation period, the energy absorption amounts calculated for the T8E multi-cell tubes using the load-displacement graphs are given in Figure 3.17.

Table 3.3 Analysis Results of T8E Model

	Peak force (kN)	Mean force (kN)	CFE	EA (kJ)	Mass (kg)	SEA (kJ/kg)
T8E1	246.41	108.16	0.44	9.734	0.435	22.377
T8E2	238.04	112.28	0.47	10.105	0.431	23.446
T8E3	240.45	89.27	0.37	8.034	0.429	18.727
Ave	241.63	103.24	0.43	9.291	0.432	21.507
FEA	269.55	93.68	0.35	8.431	0.452	18.653
Error (%)	11.55	-9.26	-18.60	-9.26	4.63	-13.27

The average EA of test specimens is 9.291 kJ, with a -9.26% error, as compared to the EA obtained via FEA, which is 8.431 kJ. The average SEA of test specimens is 21.507 kJ/kg, with a -13.27% error, as compared to the SEA obtained via FEA, which is 18.653 kJ/kg. The FEA results deviate from the experimental results by -9.26%, 11.55%, −18.60%, and -13.27% for EA, IPF, CFE, and SEA for T8E tubes, respectively.

The model accounting for the shell elements is found to be in good agreement with the test results for the multi-cell tubes T4E and T8E when the crashworthiness parameters are compared. It can be observed that acceptable variation in FEA exists. The FEA simulations are therefore considered to be within a reasonable range. Notably, multi-cell tubes do not differ significantly from one another when CFE and SEA are evaluated. The force-displacement curves for the T4E and T8E tubes have a similar overall tendency, but they are not identical to each other.

3.3.1.2 Theoretical Results

For aluminum 6061 T6 tubes σ_u is 310.0 MPa and σ_y is 276 MPa [94]. σ_0 can be calculated as:

$$\sigma_0 = \sqrt{\frac{\sigma_y \sigma_u}{1+n}} = \sqrt{\frac{310*276}{1+0.05}} = 285.457\ MPa \quad \textbf{(3.11)}$$

where n is equal to 0.05 for aluminum 6061 tubes [95]. Therefore;

$$P_{mean} = \frac{1}{2k}\sigma_0 t \sqrt{(4\mathrm{N}_T + 2\ \mathrm{N}_L + 3.65\mathrm{N}_I + 8N_C + 5.4\mathrm{N}_{II})\ \pi\ \mathrm{Lc}\ \mathrm{t}} \quad \textbf{(3.12)}$$

Effective crush distance of multi-cell tubes k is assumed equal to 0.65 [59] for aluminum 6061 multi-cell tubes.

For the tube T4E; Lc =316 mm, N_T=12, N_C=1, N_L=8 and t=1.5 mm.

$$P_{mean} = 104.811\ kN \quad \textbf{(3.13)}$$

For the tube T8E; Lc =316 mm, N_T=10, N_C=2, N_L=4 and t=1.5 mm.

$$P_{mean} = \frac{1}{2k}\sigma_0 t \sqrt{(4\mathrm{N}_T + 2\ \mathrm{N}_L + 3.65\mathrm{N}_I + 8N_C + 5.4\mathrm{N}_{II})\ \pi\ \mathrm{Lc}\ \mathrm{t}} \quad \textbf{(3.14)}$$

$$P_{mean} = 101.682\ kN \quad \textbf{(3.15)}$$

Calculated mean forces are 104.811 kN and 101.682 kN for T4E and T8E multi-cell tubes, respectively. Table 3.4 displays the mean crush force that the simulation and empirical formula predict.

Table 3.4 Comparison of mean force predicted by FE model and formula

Geometry	Mean Force (kN)	Simulation Result (kN)	Error (%)	Empirical Formula (kN)	Error (%)
T4E	100.16	93.98	-6.17	104.81	4.64
T8E	103.24	93.68	-9.26	101.68	-1.51

The mean force according to empirical formula is 104.81 kN, with a 4.64% error, as compared to the mean force obtained via tests, which is 100.16 kN for T4E tubes. The mean force according to the empirical formula is 101.68 kN for T8E tubes, with a -1.51% error, as compared to the mean force obtained via tests, which is 103.24 kN for T4E tubes. The simulation values coincide with the mean forces derived from the empirical formula and experimental results.

3.3.2 Foam-filled Rectangular Tubes

3.3.2.1 FEM Results

Similar to the empty tubes, foam-filled multi-cell tubes T4FF and T8FF are modeled in Ls- Dyna with the same contact algorithms and material tube properties.

A comparison of load-displacement curves obtained from the tests and FE model for T4FF multi-cell tubes is provided in Fig. 3.19. The deformed images of the T4FF multi-cell tubes obtained in experiments and the predicted results of the finite element analysis are compared in Fig. 3.20. Figure 3.19 shows that when the crash force reaches around 325 kN, cracks begin to take place in the tubes. However, force-displacement graphs become distinct for test specimens after the decrease in crash force is observed.

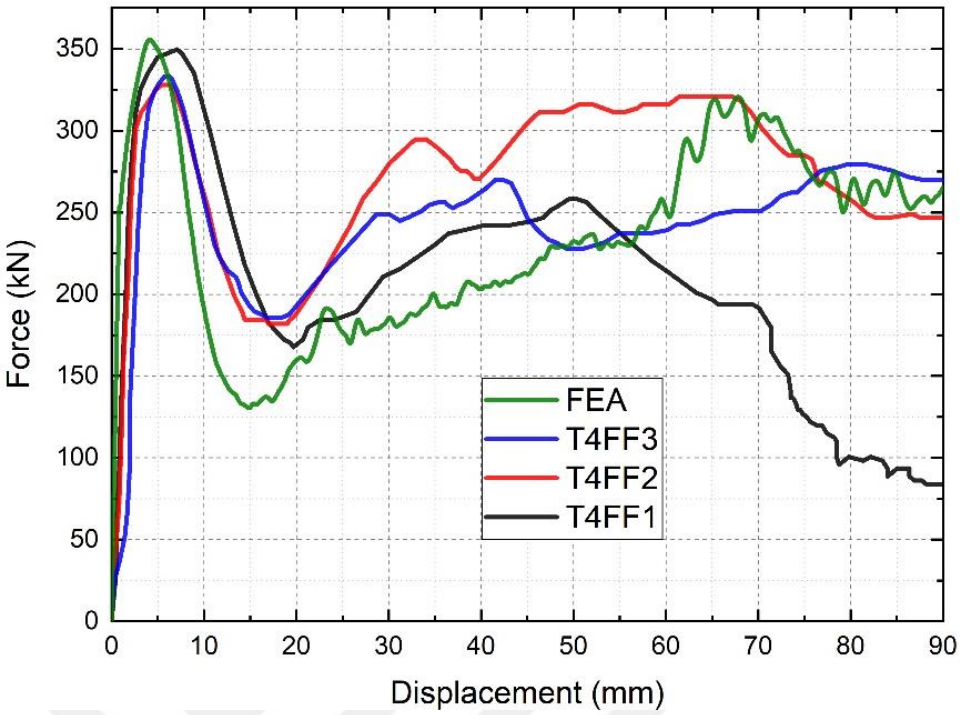

Figure 3.19 Comparison of load-displacement curves between the experimental study and FEA simulation for foam-filled T4 tubes

The images of the deformed views of the test specimen and the finite element model are shown in Fig. 3.20. Multi-cell T4FF tubes do not show progressive deformation in both experiments and FE predictions. Splitting at mid height and fracture due to the applied force are observed.

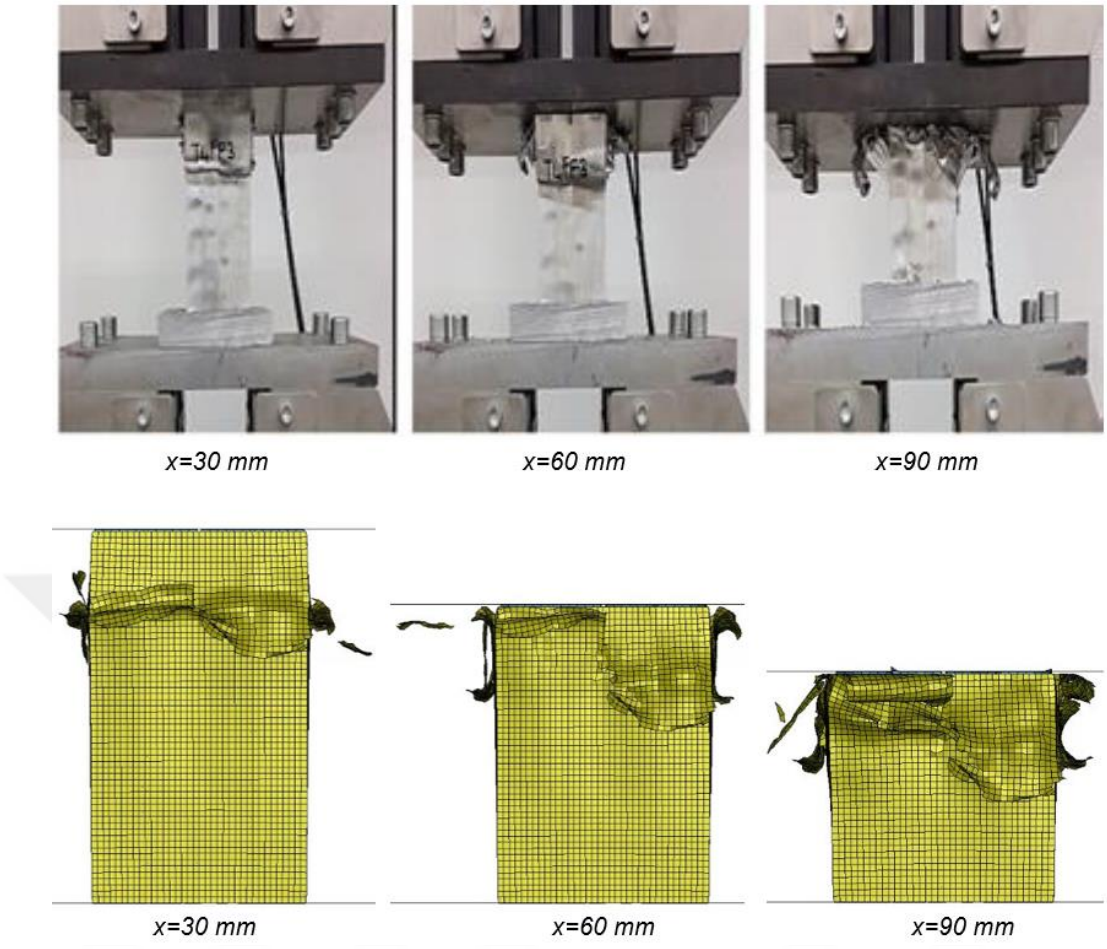

Figure 3.20 Comparison of collapse modes of foam-filled T4 tubes between experimental and FEA results

At the end of the deformation period, the energy absorption amounts calculated for the T4FF multi-cell tubes using the load-displacement graphs are given in Table 3.5. The SEA obtained via FEA is 20.536 kJ/kg, with a 0.96% error, as compared to the SEA of test specimens, which is 20.340 kJ/kg. The EA obtained via FEA is 21.255 kJ, with a -2.06% error, as compared to the EA of test specimens, which is 21.703 kJ.

Table 3.5 Analysis Results of T4FF Model Comparison of mean force predicted by model and formula

	Peak force (kN)	Mean force (kN)	CFE	EA (kJ)	Mass (kg)	SEA (kJ/kg)
T4FF1	349.70	204.99	0.59	18.449	1.010	18.266
T4FF2	328.10	274.40	0.84	24.696	1.156	21.363
T4FF3	333.0	244.03	0.73	21.963	1.036	21.200
Ave	336.93	241.14	0.72	21.703	1.067	20.340
FEA	355.74	236.17	0.66	21.255	1.035	20.536
Error (%)	5.58	-2.06	-8.33	-2.06	-3.00	0.96

A comparison of load-displacement curves obtained from the tests and FE model for foam-filled T8 multi-cell tubes is provided in Fig. 3.21. The images of the T8FF test specimen and the results of the finite element analysis with compression are shown in Fig. 3.22.

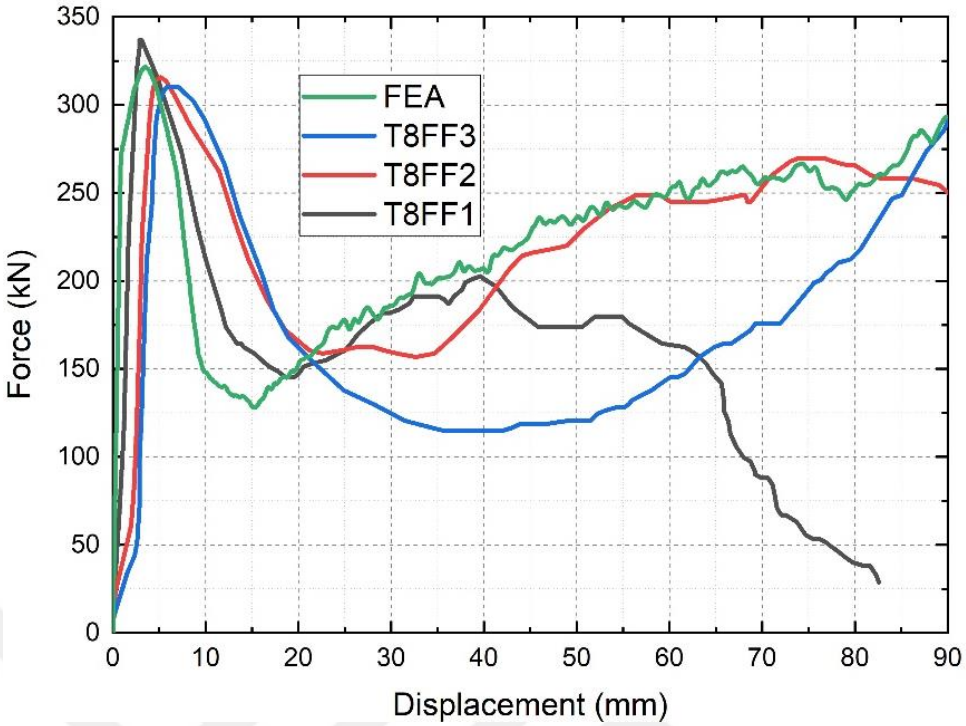

Figure 3.21 Comparison of load-displacement curves between the experimental study and FEA simulation for foam-filled T8FF tubes

Figure 3.21 shows that after the crash force reaches around 325 kN, the crash force decreases due to cracks and splitting. Also, force-displacement graphs differ for test specimens after the decrease is observed.

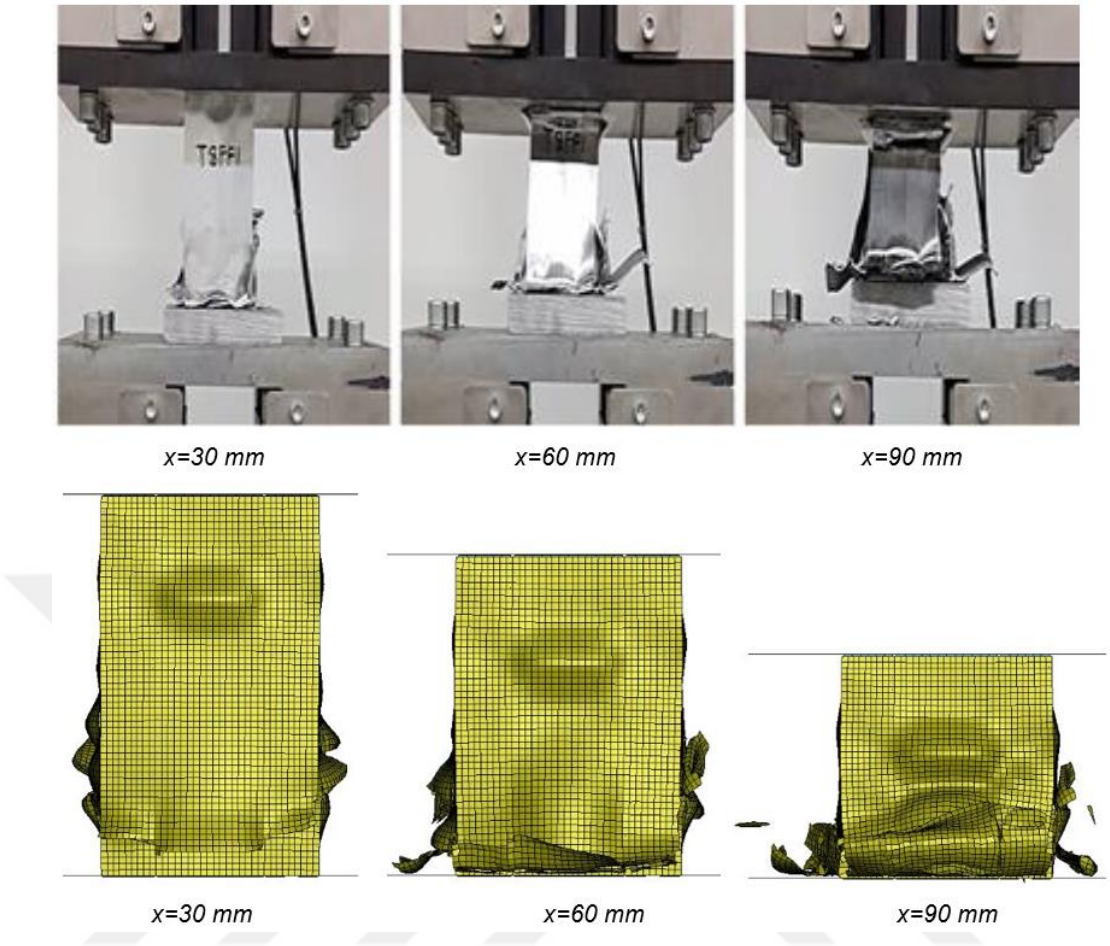

Figure 3.22 Comparison of collapse modes of foam-filled T8 tubes between experimental and FEA results

As can be seen from Fig. 3.22, T8FF multi-cell tubes start to deform from the ends after the peak force is reached. Due to increasing deformation distance, the folding occurs not properly, and tears are observed in the corners in both test specimens and the FE model.

The deformed views of the T4FF and T8FF tubes obtained experimentally and numerically are presented in Figs. 3.20 and 3.22, respectively. Deformation behaviors are similar, and the tubes experience significant plastic deformation with cracks. The numerical models also successfully capture the splitting that occurs at the folded region's corners.

Since tube T8FF1 completely collapsed, the test was stopped for specimen 1 when the deformation distance reached 80 mm. Therefore energy absorption parameters are calculated for 80 mm displacement for foam-filled T8 tubes as given in Table 3.6. The SEA obtained from the FEA is 16.906 kJ/kg, with a 15.86% error, as compared to the SEA of test specimens, which is 14.592 kJ/kg. The EA of the FEA is 14.942 kJ, with a 17.11% error, as compared to the EA of test specimens, which is 14.942 kJ.

Table 3.6 Analysis Results of T8FF Model

	Peak force (kN)	Mean force (kN)	CFE	EA (kJ)	Mass (kg)	SEA (kJ/kg)
T8FF1	336.80	165.94	0.49	13.275	0.987	13.450
T8FF2	315.70	221.67	0.70	17.735	1.046	16.955
T8FF3	310.0	172.71	0.56	13.817	1.038	13.311
Ave	320.83	186.78	0.58	14.942	1.024	14.592
FEA	321.52	218.72	0.68	17.498	1.035	16.906
Error (%)	0.21	17.10	17.24	17.11	1.07	15.86

The crashworthiness results are compared in Table 3.5 for foam-filled multi-cell tubes T4FF and Table 3.6 for foam-filled multi-cell tubes T8FF. A good agreement between FEA and the experimental results is achieved.

3.3.2.2 Theoretical Results

For foam-filled tubes mean force is calculated as:

$$P_{mean} = P_{tube} + \sigma_f \, a \, b + C_{avg} \sqrt{\sigma_f \ \sigma_0} \ \ c \, t \qquad \textbf{(3.16)}$$

where σ_f the foam plateau stress and c can be calculated:

$$c = \frac{a+b}{2} \quad \textbf{(3.17)}$$

where a and b are the cross-section of the rectangular tube.

P_{tube} was calculated 104.811 kN for empty multi-cell tube T4E. The mean force of T4FF tube can be calculated as:

$$P_{mean} = P_{tube} + \sigma_f\, ab + C_{avg} \sqrt{\sigma_f\ \sigma_0}\ [\frac{a+b}{2}]\, t \quad \textbf{(3.18)}$$

where $a = 68\, mm$, $b = 82\, mm$, $t = 1.5mm$ and $\sigma_f = 12.8MPA$, C_{avg} is a linear increasing function of deformation and equal to 5.5 [59].

$$P_{mean} = 213.586\, kN \quad \textbf{(3.19)}$$

Mean force of T8FF tube can be calculated as:

$$P_{mean} = P_{tube} + \sigma_f\, a\, b + C_{avg} \sqrt{\sigma_f\ \sigma_0}\ c\, t \quad \textbf{(3.20)}$$

where σ_f the foam plateau stress and c can be calculated:

$$c = \frac{a+b}{2} \quad \textbf{(3.21)}$$

where a and b are the dimensions of the multi-cell tube and P_{tube} was calculated 108.682 kN for empty multi-cell tube T8E. Mean force of T8FF tube can be calculated as:

$$P_{mean} = P_{tube} + \sigma_f\, a\, b + C_{avg} \sqrt{\sigma_f\ \sigma_0}\ c\, t \quad \textbf{(3.22)}$$

where $a = 68\, mm$, $b = 82\, mm$, $t = 1.5mm$ and $\sigma_f = 12.8MPA$, C_{avg} is a linearly increasing function of deformation and equal to 5.5 [59].

$$P_{mean} = 215.457\, kN \quad \textbf{(3.23)}$$

The mean crush forces that the simulation and empirical formula estimated are shown in Table 3.7. The simulation results match the mean forces calculated using the empirical formula and the experimental data.

Table 3.7 Comparison of mean force predicted by model and formula

Geometry	Mean Force (kN)	Simulation Result (kN)	Error (%)	Emprical Formula (kN)	Error (%)
T4FF	241.14	236.17	-2.06	213.59	-11.42
T8FF	186.78	218.72	17.10	215.46	15.35

The mean force according to emprical formula is 213.59 kN, with a -11.42% error, as compared to the mean force obtained via tests, which is 241. 41 kN for T4FF tubes. The mean force according to emprical formula is 215.46 kN for T8FF tubes, with a 15.35% error, as compared to the mean force obtained via tests, which is 186.78 kN for T8FF tubes. The simulation values coincide with the mean forces derived from the empirical formula and experimental results.

3.4 Results and Discussion

This work investigates the crashworthiness of multi-cell aluminum tubes under quasi-static conditions numerically and theoretically. In the numerical model, every specimen folds at mid-height. The material behavior of the tubes during the deformation in the numerical model is characterized using the power law material model and its complementary damage model. The multi-cell tubes' crashworthiness performances are assessed using a variety of criteria, including energy absorbed, specific energy absorption, initial peak force, and crush force efficiency. The simulation results match the mean forces that are calculated using the empirical formula and the experimental results.

The effective and sustainable results can be listed as follows:

- The material model used in the FE model is essential for accurately simulating the crash tests of thin-walled aluminum multi-cell tubes.
- Defining appropriate contact mechanisms and boundary conditions for the FE model result in consistent energy absorption parameters with experimental values.
- Emprical formula can predict the mean force values of both empty and foam-filled multi-cell tubes when foam properties and geometrical properties are defined.
- The averages of the CFE, EA and SEA of the T8E tubes are higher than T4E tubes and the peak force of the T4E tube is higher than the peak force of the T8E tube.
- Similarly the average of the peak force of the T4FF tubes is higher than the average of the peak force of the T8FF tubes.
- The average SEA of the T8E tubes is 5.69 % higher and CFE of the T8E tube is 10.26 % higher than the T4E tubes.
- Although putting aluminum foam inside the T4 multi-cell tube does not improve the SEA for 90 mm deformation, it enhances the EA and CFE by 140.77% and 84%, respectively.

CHAPTER 4

EXPERIMENTAL AND NUMERICAL STUDIES OF ALUMINUM, COMPOSITE AND HYBRID TUBES UNDER QUASI-STATIC LOADING

4.1 Introduction

Composite structures usually exhibit better crashworthiness performance than metals due to their lightweight and energy absorbing capability through progressive crushing by a combination of several mechanisms including fiber fracture, matrix fracture, bending, delamination, splitting, and friction. The overall deformation during the forming process is a combination of all those deformation modes.

4.2 Fabrication of Tubes

Composites have been manufactured by various techniques which were developed to satisfy specific design or application needs. Appropriate method depends on the material property and the part design. Most of the composite fabrication processes require kind of tools like die, mold or mandrel, to shape the resin and reinforcement. The common and economic fabrication method for crashworthy structures is hand layup. The hand layup method composes of laying dry fabric layers or plies to form a laminate stack. Also, prepreg materials can be used to manufacture the tubes. Circular tube specimens are fabricated through hand layup technique including 6 plies with a stacking sequence of $[\pm 75]_3$. GFRP tubes are produced with a wall thickness of 2.76 mm, a length of 100 mm, and a diameter of 85.52 mm. Aluminum tubes are alloy 6082-T6 with a wall thickness of 2 mm, a length of 100 mm, and a diameter of 80 mm. Aluminum tubes with the same cross-section are used to produce hybrid tubes. Hybrid tubes include an aluminum tube inside with a wall thickness of 2 mm, a length of 100 mm, and a diameter of 80 mm and GFRP tube wrapping with a wall thickness of 2.76 mm, a length of 100 mm, and a diameter of 85.52 mm. All the empty tubes are shown in Figure 4.1.

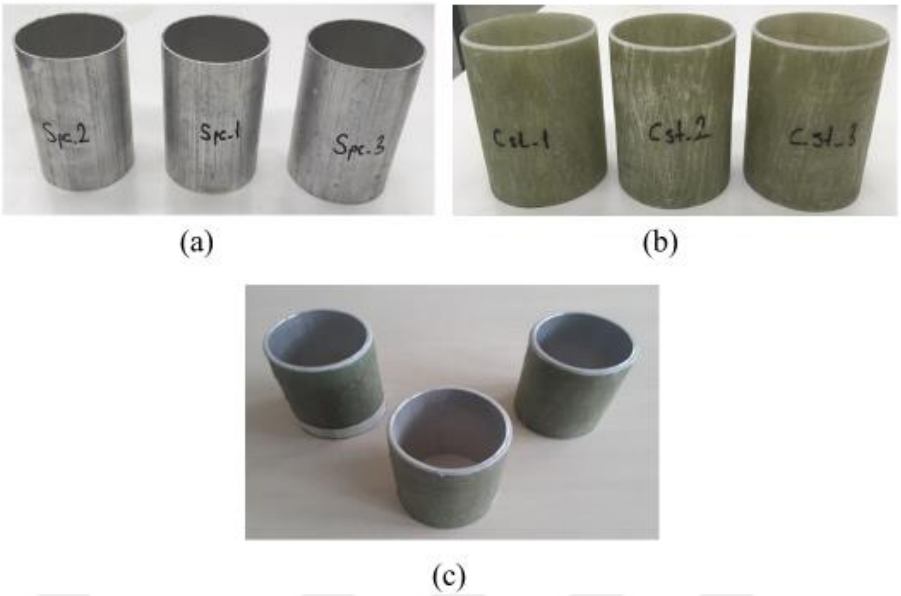

Figure 4.1 Empty test specimens (a) aluminum 6082 T6 tubes (b) GRFP Tubes (c) Hybrid Tubes

GFRP and hybrid tubes filed to have chamfer before the crash tests to deform progressively. Details of the chamfering can be seen in Figure 4.2.



Figure 4.2 Chamfering of the hybrid tube

4.3 Experimental Setup

Aluminum, GFRP, empty and honeycomb-filled hybrid tubes compressed axially under quasi-static loading conditions. Each test was carried out within 30 minutes for the 60 mm (3/5 of the overall specimen's length) deformation distance of the crash boxes and the displacement rate was 2 mm/min. All experiments were repeated three

times to ensure the accuracy of the test results for the GFRP, aluminum, empty and honeycomb-filled hybrid crash boxes.

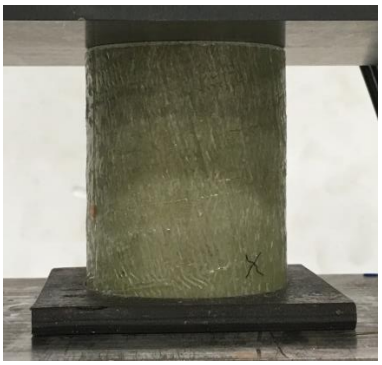

Figure 4.3 Hybrid tube with bottom plate

The tests were carried out on the INSTRON 600 LX compression test device, which has a maximum system pressure of 8.3 bar, and a load capacity of 600 kN in the Mechanical Test Laboratory at the Technology Center of TOBB University of Economics and Technology. A bottom plate with a depth of 5 mm, which is compatible with the tubes, was produced by an industrial type CNC milling machine to make the tubes stable between the two blocks during the tests. The crash boxes were fixed to the floor, and they did not shift during the press as shown in Figure 4.3.

To enhance the energy absorption capacity of empty hybrid tubes, aluminum honeycomb sections were inserted to empty hybrid tubes as shown in Fig 4.4.



Figure 4.4 Honeycomb-filled hybrid specimens

The test conditions in honeycomb-filled tube experiments were taken the same as in the other tubes. Compression speed was set as 2 mm/min and compression force was applied to the boxes for 30 minutes, causing them to undergo 60 mm deformation.



x =0 *x=20 mm* *x=40 mm* *x=60 mm*

Figure 4.5 Experiments of Aluminum Tubes

Under the specified test conditions, firstly, the empty aluminum tubes were tested. Separate tests were applied to each tube. All aluminum test specimens are deformed progressively with the same deformation behavior. The deformation images of specimen 1 are given in Figure 4.5. Crash boxes undergo regular and homogeneous plastic deformation under the applied compressive loads. Tearing or splitting on the surfaces of the crash boxes does not occur during the loading.

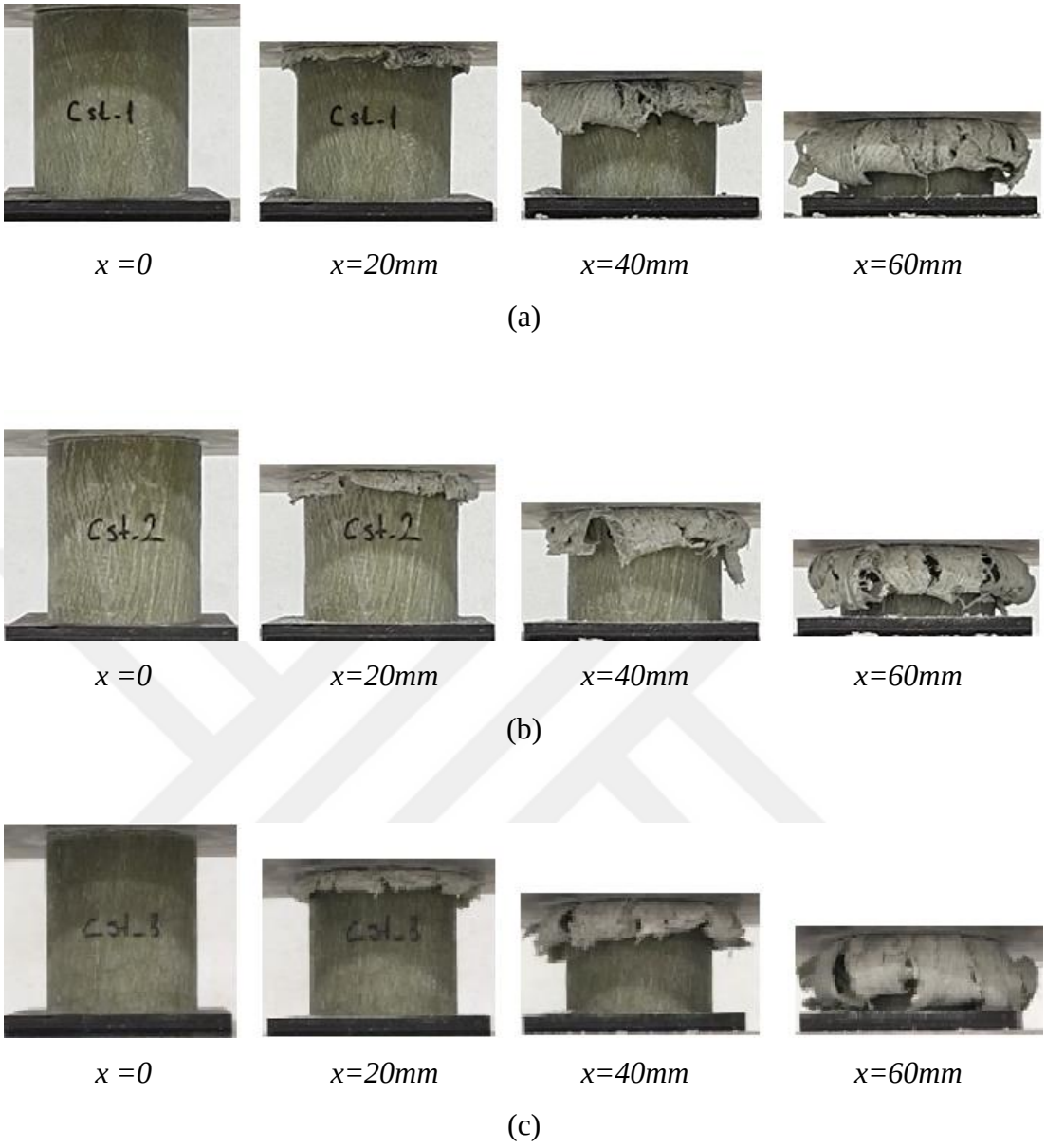

x =0 *x=20mm* *x=40mm* *x=60mm*

(a)

x =0 *x=20mm* *x=40mm* *x=60mm*

(b)

x =0 *x=20mm* *x=40mm* *x=60mm*

(c)

Figure 4.6 Experiments of GFRP Tubes

The deformation images of the GFRP tubes under axial compression are given in Figure 4.6. In the compression tests, it is observed that the deformation starts to occur after the peak force is reached and first occurs in the upper parts of the GFRP tubes. Under the axial compressive loads, tubes collapse plastically in a predictable and homogeneous manner. The surfaces of the crash boxes are not damaged or split while being loaded. All test specimens made of GFRP experience progressive deformation with similar deformation characteristics.

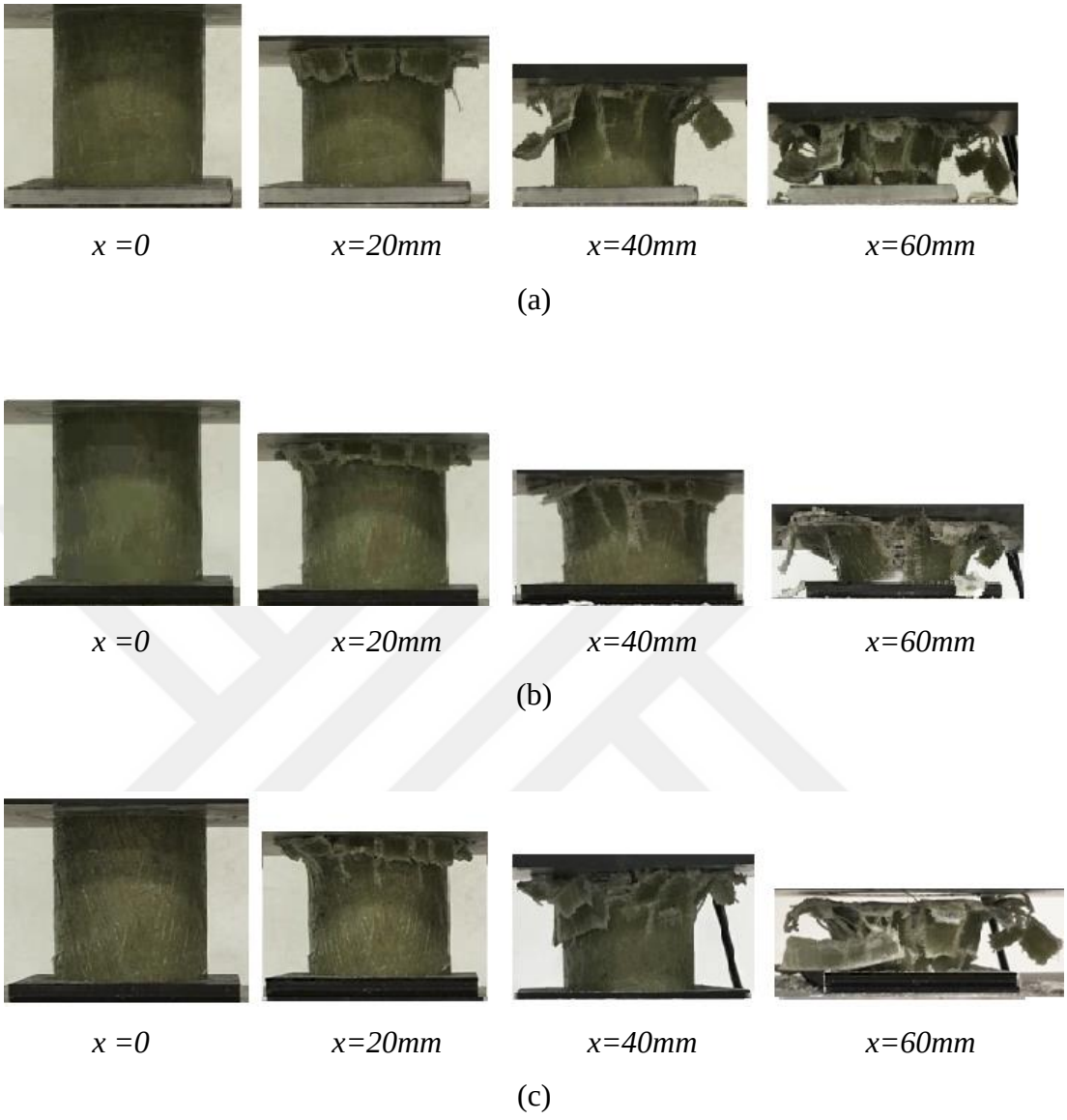

Figure 4.7 Experiments of Hybrid Tubes

Figure 4.7 shows the deformation images of the hybrid tubes under axial compression. As in the composite boxes, the first deformations in hybrid tubes also occur in the upper part of the tubes. Due to the compression, cracks start to occur for all hybrid specimens before the deformation distance of 20 mm. The deformation behavior is similar for all hybrid test specimens, and it is progressive.



x =0 *x=20mm* *x=40mm* *x=60mm*

(a)



x =0 *x=20mm* *x=40mm* *x=60mm*

(b)



x =0 *x=20mm* *x=40mm* *x=60mm*

(c)

Figure 4.8 Experiments of Honeycomb-Filled Hybrid Tubes

Deformed views of honeycomb-filled hybrid tubes are shown in Figure 4.8. Similar to empty hybrid tubes, the upper portion of honeycomb-filled hybrid tubes experiences the earliest deformations. Before the 20 mm deformation distance, all honeycomb-filled hybrid specimens begin to crack due to compression. For all hybrid boxes, the deformation behavior is similar which includes progressive failure with cracks.

The force-displacement curves of the tubes s taken from the quasi-static experiments are presented in Figure 4.9. It can be seen that GFRP wrapping to aluminum tubes increases energy absorption significantly.

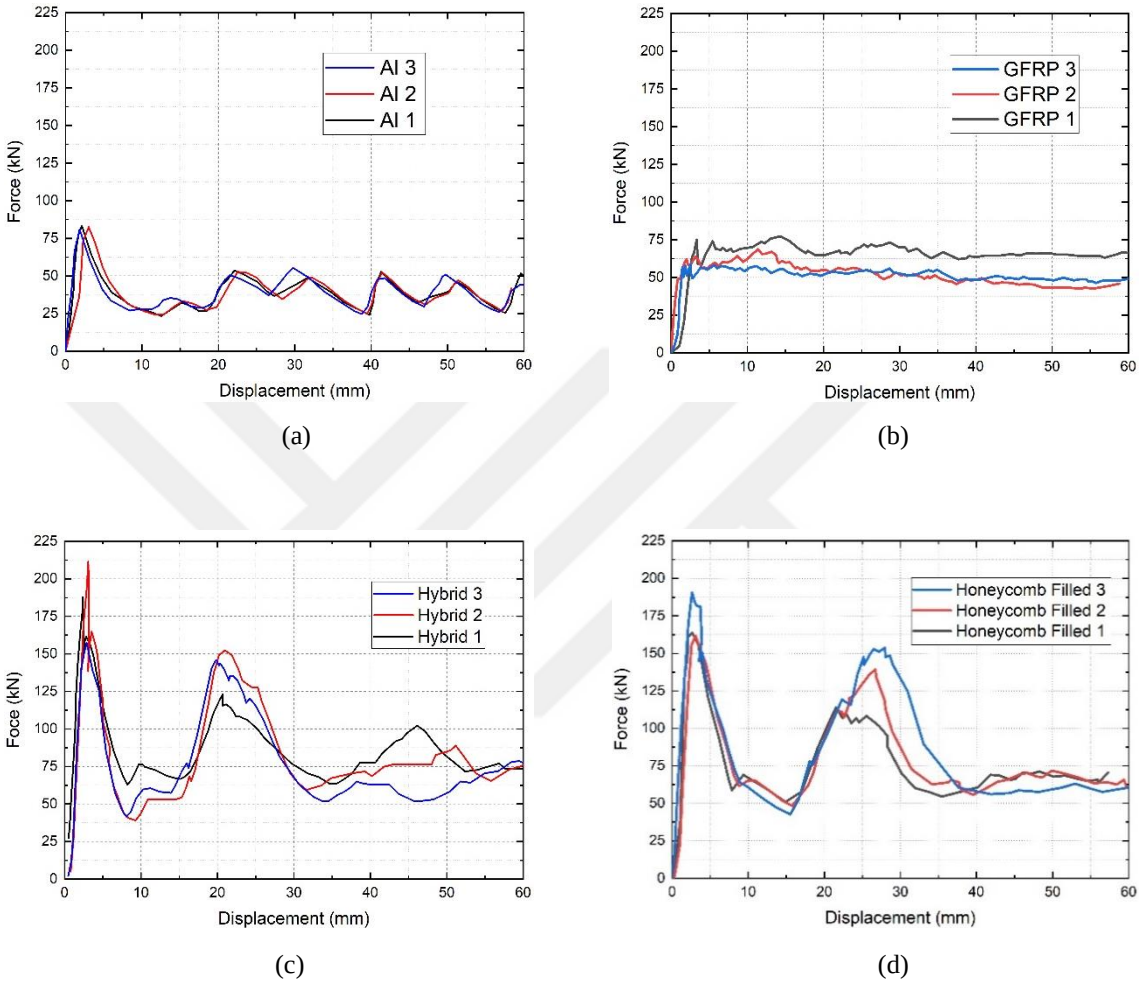

Figure 4.9 Force-displacement behavior of test specimens from experiments (a) Aluminum 6082 T6 Tubes (b) GRFP Tubes (c) Hybrid Tubes (d) Honeycomb-filled Hybrid Tubes

Deformations start to occur in all profiles when the compression load reaches maximum force. At the end of the deformation period, the energy absorption amounts are calculated for the tubes using the load-displacement graphs given in Fig. 4.9. Energy absorption values of test specimens are compared with FE model predictions. Deformed views of the boxes are shown in Figure 4.10. Test specimens are found consistent with each other.

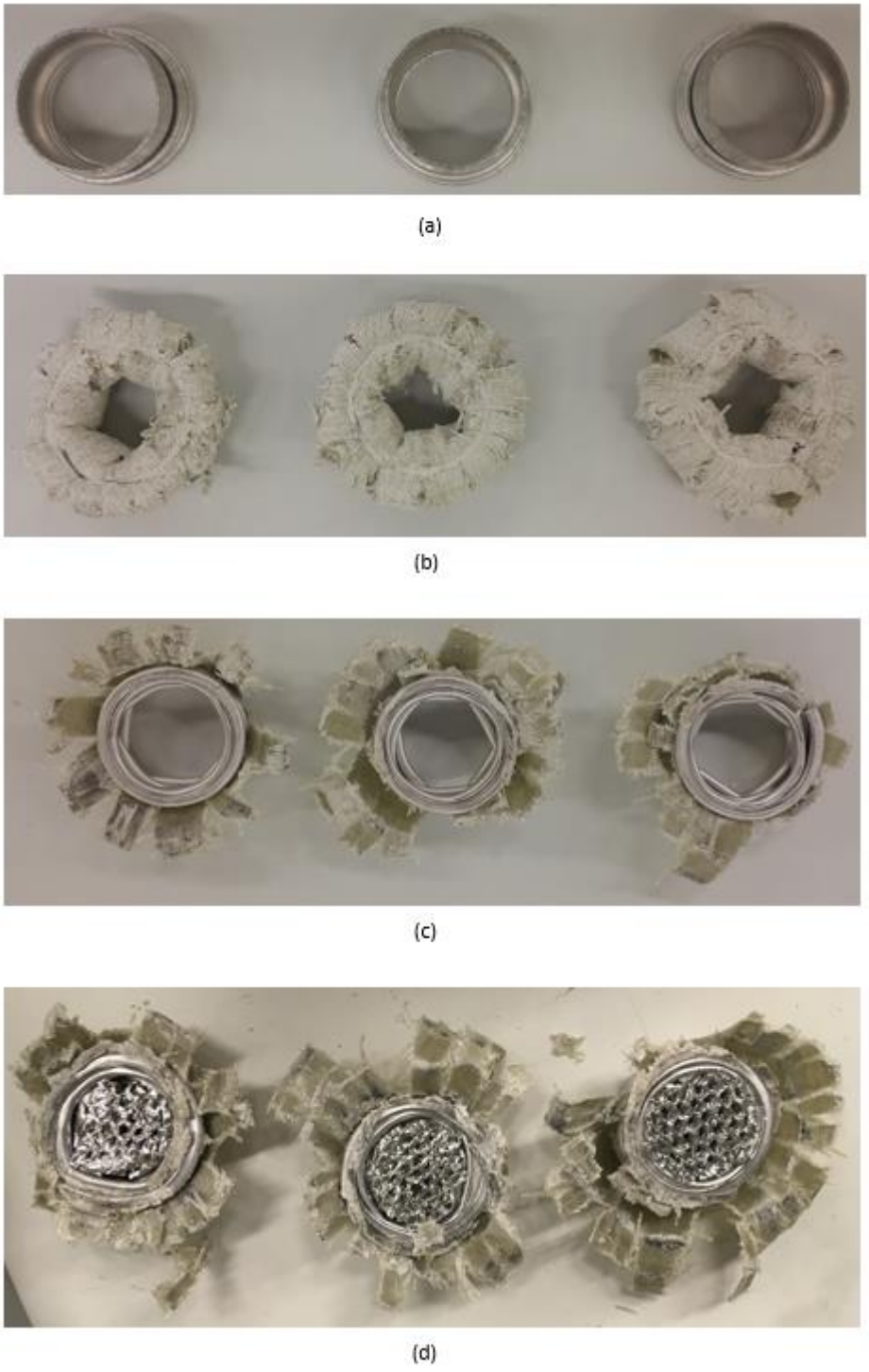

Figure 4.10 60 mm deformed specimens (a) Aluminum 6082 T6 Tubes (b) GRFP Tubes (c) Hybrid Tubes (d) Honeycomb-filled Hybrid Tubes

4.4 Determination of Mechanical Properties

Composite materials have been the subject of interest in the automotive industry for vehicle designs with better crashworthiness and lightweight. MAT_54 allows the user to create a local material coordinate system to specify the orientation of each ply in Ls-Dyna. The parameters in MAT_54 need to be specified, some are physical parameters and some are numerical parameters. From the physical parameters, 10 parameters are material constants, the values of which can be obtained from material characterization tests. ASTM standards are applied for the tensile, compression, and shear tests. ASTM standards used to obtain material properties of GFRP tubes are given below in Table 4.1.

Table 4.1 Material properties and tests

	Description	**Test**	**Standard**
EA	Modulus in longitudinal (fiber) direction	0º tensile test	ASTM D3039
EB	Modulus in transverse direction	90º tensile test	ASTM D3039
PRCA	Major Poission's ratio	0º tensile test	ASTM D3039
PRBA	Minor Poission's ratio	90º tensile test	ASTM D3039
XT	Longitudinal tensile strength	0º tensile test	ASTM D3039
YT	Transverse tensile strength	90º tensile test	ASTM D3039
XC	Longitudinal compressive strength	0º compression test	ASTM 6641
YC	Transverse compressive strength	90º compression test	ASTM 6641
SC	Shear strength	Shear Test	ASTM D3518
G12	Shear Modulus	Shear Test	ASTM D3518

The five physical parameters needed in the model are the tensile and compressive failure strains (element deletion strains) in the fibre direction (DFAILT and DFAILC), the matrix and shear failure strains (DFAILM and DFAILS), and the effective failure

strain (EFS). A comprehensive parametric study is performed to calibrate these parameters to simulate load-displacement behavior of test specimens.

In order to determine the properties of GFRP tubes mechanical tests were applied. Tensile test, compression test, and shear test were applied to obtain the material properties needed for MAT_54 used in Ls-Dyna. All tests were repeated minimum of five times to ensure the accuracy of the test results. The manufacturer prepared six specimens for some of the tests. Therefore results of the all specimens were given in the tables below. Material density and fiber volume fraction values were given by the manufacturing company as 1.5 g/cm^3 and 33%, respectively.

In-Plane Tensile Test

According to ASTM International, Standard Test Method for Tensile Properties of Polymer Matrix Composite Materials D3039 tensile tests were applied to test specimens with 0 and 90 º fibre orientation with the velocity of 2 mm/min.

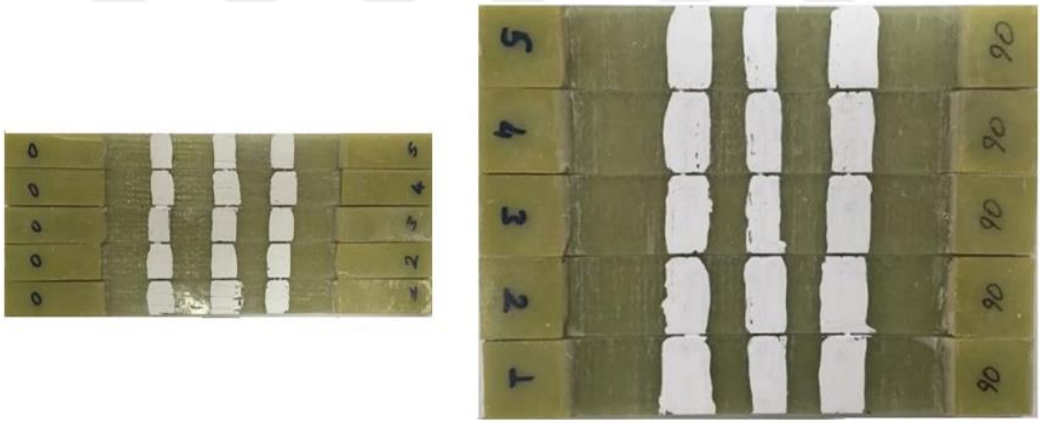

(a) 0 º test specimens (b) 90 º test specimens

Figure 4.11 Tensile test specimens

Test specimen geometry was determined according to ASTM D3039 as 250 mm x 15 mm x 2 mm for 0º fibre orientation and 175 mm x 25 mm x 2 mm for 90º fibre orientation as shown in Fig.4.11. Test specimens consist of two regions: gauge length, in which failure is expected to occur, and the two end regions with tabs which are

clamped to the test machine. All experiments were repeated five times to ensure the accuracy of the test results for the tensile tests.

Table 4.2 Test specimen geometry for 0º fibre orientation

Sample No	Thickness (mm)	Width (mm)
1	2.29	14.83
2	2.41	14.91
3	2.39	14.95
4	2.34	14.82
5	2.32	14.83

Geometric details of the specimens are given in Table 4.2 and Table 4.3 for 0 and 90 º fibre orientations, respectively.

Table 4.3 Test specimen geometry for 90º fibre orientation

Sample No	Thickness (mm)	Width (mm)
1	2.67	24.99
2	2.48	24.98
3	2.69	24.99
4	2.54	25.02
5	2.56	24.99

A view of the test specimen during the tensile test is given in Figure 4.12.



Figure 4.12 Tensile test

Deformed tensile test specimens are given in Figure 4.13. Although crack is expected in the mid height of the specimens, cracks are observed near the tab in all specimens.

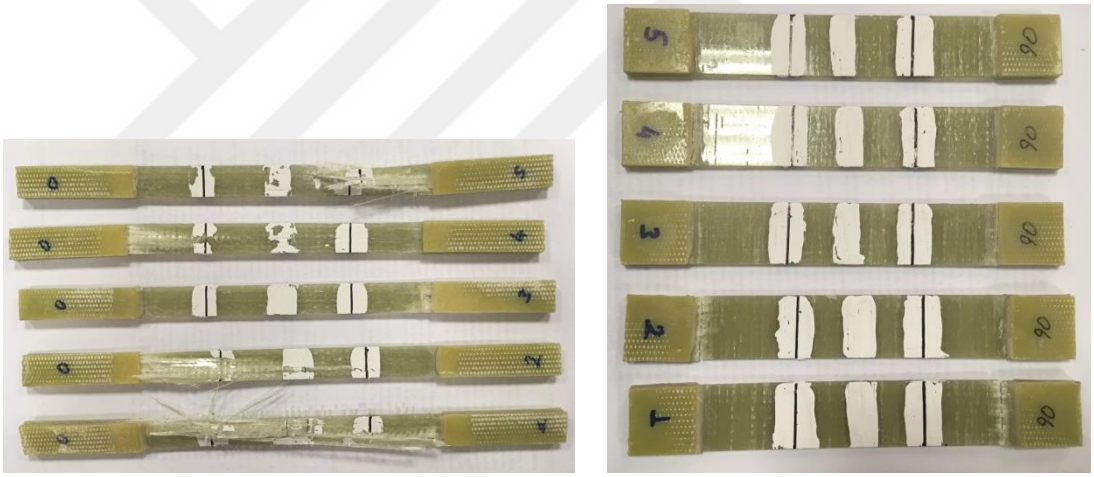

(a) 0º test specimens after test (b) 90º test specimens after test

Figure 4.13 Tensile test specimens after tensile tests

Figure 4.14 shows stress-strain curves obtained from the tensile tests. These curves are used to calculate tensile strength and elastic modulus.

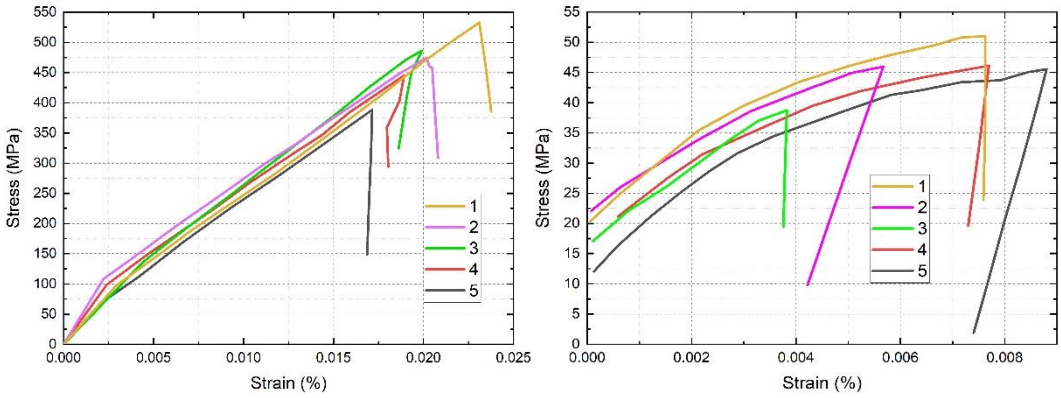

Figure 4.14 Stress-strain Graph of test specimens (a) 0 º specimens (b) 90 º specimens

Tensile test results are given in Table 4.4 and Table 4.5 in detail. Average tensile strength was found 469.1 MPa and 45.8 MPa for the specimens with 0 and 90 º fibre orientation, respectively.

Table 4.4 Test results for 0 º fibre orientation

Sample No	Tensile Strength (MPa)	Elastic Modulus (GPa)	Strain at Break (%)	Poisson's Ratio
1	536.9	21.54	2.30	0.19
2	487.9	21.63	1.98	0.28
3	392.5	21.49	1.70	0.38
4	447.9	21.20	1.88	0.20
5	480.3	21.90	2.02	0.18
Avg.	**469.1**	**21.55**	**1.97**	**0.24**
St. Dev. (±)	**53.3**	**0.2**	**0.2**	**0.08**

Table 4.5 Test results for 90 º fibre orientation

Sample No	Tensile Strength (MPa)	Elastic Modulus (GPa)	Strain at Break (%)	Poisson's Ratio
1	45.8	7.88	0.88	0.15
2	51.3	7.25	0.76	0.13
3	46.3	6.56	0.77	0.09
4	46.5	6.55	0.56	0.12
5	39.2	6.40	0.37	0.17
Avg.	**45.8**	**6.92**	**0.66**	**0.13**
St. Dev. (±)	**4.3**	**0.6**	**0.2**	**0.03**

In-Plane Compression Test

According to ASTM International, Standard Test Method for Compressive Properties of Polymer Matrix Composite Materials Using a Combined Loading Compression (CLC) Test Fixture - D6641 compressive tests were applied to test specimens with 0º and 90º fibre orientation with the velocity of 2 mm/min. Test specimens can be seen in Figure 4.15.

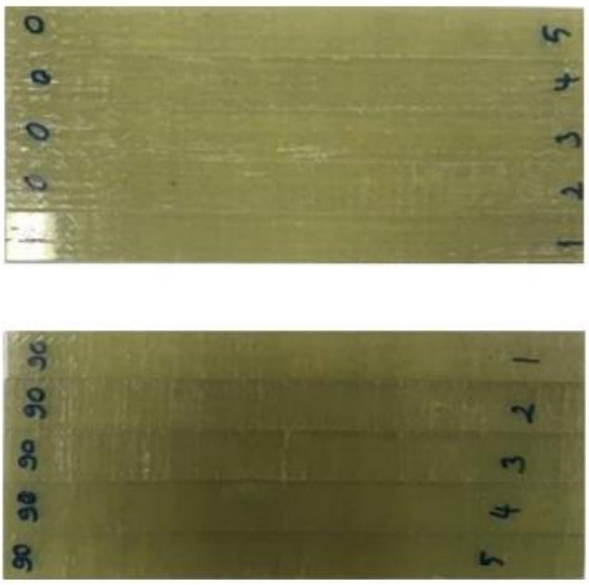

Figure 4.15 Compression test specimens

Test specimen geometry was determined according to ASTM 6641 as 140 mm x 12 mm x 2 mm for the specimens with 0 and 90º fibre orientation as shown in Table 4.6 and Table 4.7.

Table 4.6 Test specimen geometry for 0º fibre orientation

Sample No	Thickness (mm)	Width (mm)
1	2.32	11.94
2	2.49	11.98
3	2.40	11.90
4	2.44	11.91
5	2.37	11.93
6	2.46	11.96

To guarantee the accuracy of the test findings for the tensile tests, each experiment was carried out six times.

Table 4.7 Test specimen geometry for 90º fibre orientation

Sample No	Thickness (mm)	Width (mm)
1	2.47	12.01
2	2.52	11.98
3	2.54	11.97
4	2.47	12.01
5	2.49	12.01
6	2.57	12.02

A view of the specimen during the compression test is given in Figure 4.16.



Figure 4.16 Compression test

Compressed test specimens are shown in Figure 4.17. Deformation is observed at the mid height of the specimen as expected.

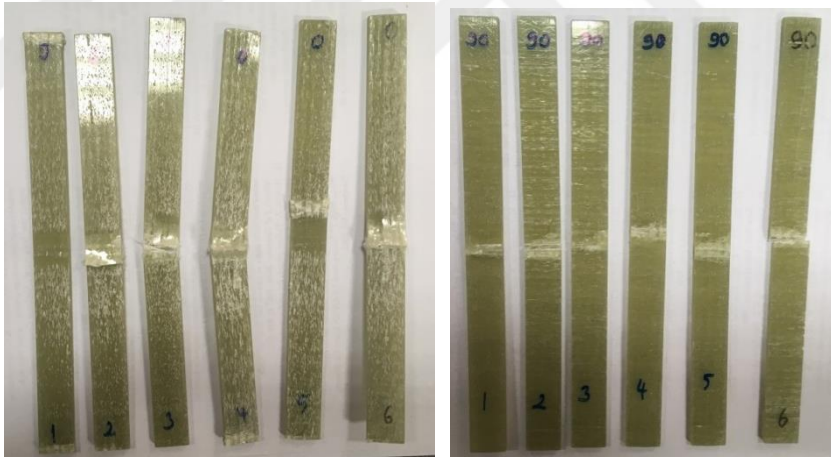

(a) (b)

Figure 4.17 Compression test specimens after tests (a) 0º test specimens after test (b) 90º test specimens after test

Figure 4.18 shows the force-stroke curves obtained from the compression tests. These curves are used to calculate compression strength.

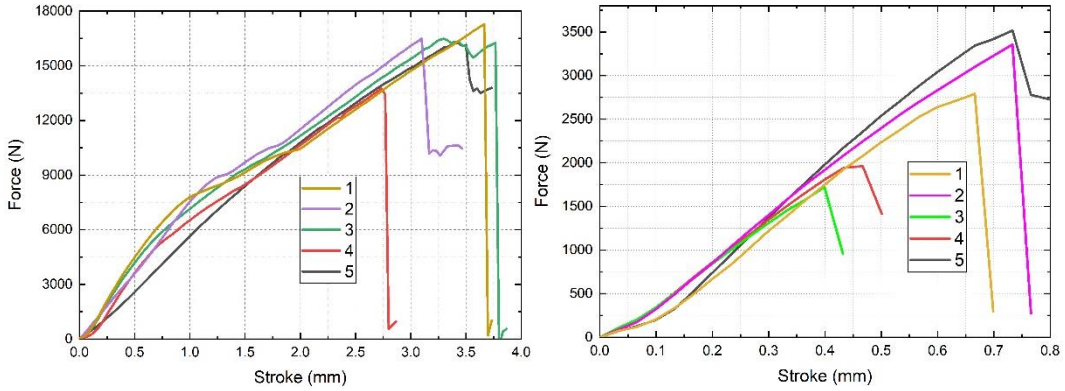

(a) (b)

Figure 4.18 Force-stroke Graph of test specimens (a) 0º test specimens after test (b) 90º test specimens after test

Compression test results are given in Table 4.8 and Table 4.9 in details. Avearage compression strength is found 542.51 MPa and 82.70 MPa for the specimens with 0º and 90º fibre orientation, respectively.

Table 4.8 Test results for 0º fibre orientation

Sample No	Compression Strength (MPa)	Maximum Force (N)
1	587.24	16267
2	461.09	13754
3	468.69	13385
4	567.19	16482
5	583.35	16493
6	587.47	17284
Avg.	**542.51**	**15610**
St. Dev. (±)	**60.62**	**1622.92**

Table 4.9 Test results for 90º fibre orientation

Sample No	Compression Strength (MPa)	Maximum Force (N)
1	118.51	3515
2	65.00	1962
3	56.68	1723
4	113.14	3356
5	93.36	2792
6	49.51	1529
Avg.	**82.70**	**2479**
St. Dev. (±)	**29.71**	**858.10**

Shear Test

According to ASTM Standard Test Method for In-Plane Shear Response of Polymer Matrix Composite Materials by Tensile Test of [±45] Laminate - D3518 shear tests were applied to test specimens with [±45] fibre orientation with the velocity of 2 mm/min. Test specimens prepared for the shear test can be seen in Figure 4.19

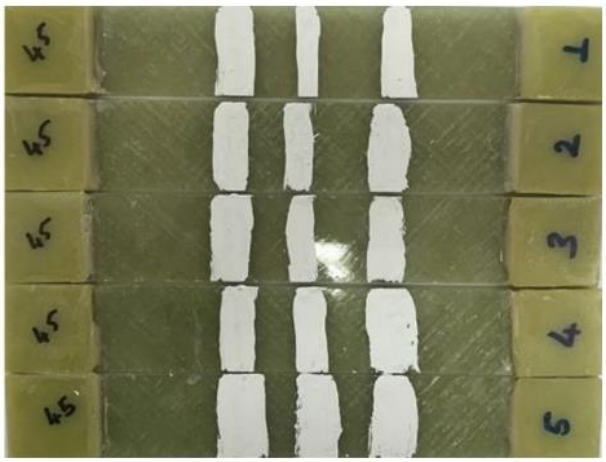

Figure 4.19 Shear test specimens

Test specimen geometry was determined according to ASTM 3518; 175 mm x25 mm x 2 mm for [±45] fibre orientation as shown in Table 4.10. To guarantee the correctness of the test findings for the shear tests, every experiment was carried out six times.

Table 4.10 Test results for 90 º fibre orientation

Sample No	Thickness (mm)	Width (mm)
1	2.48	24.98
2	2.55	24.97
3	2.56	24.89
4	2.55	24.97
5	2.58	24.97
6	2.57	24.96

View of the specimen during the shear test was given in Figure 4.20.



Figure 4.20 Shear test

All the test specimens are shown in Figure 4.21. Deformation is observed at the mid height of the specimens as expected.



Figure 4.21 Shear test specimens after tests

Figure 4.22 shows strain-stress curves obtained from the shear tests. These curves are used to calculate shear strength and elastic modulus.

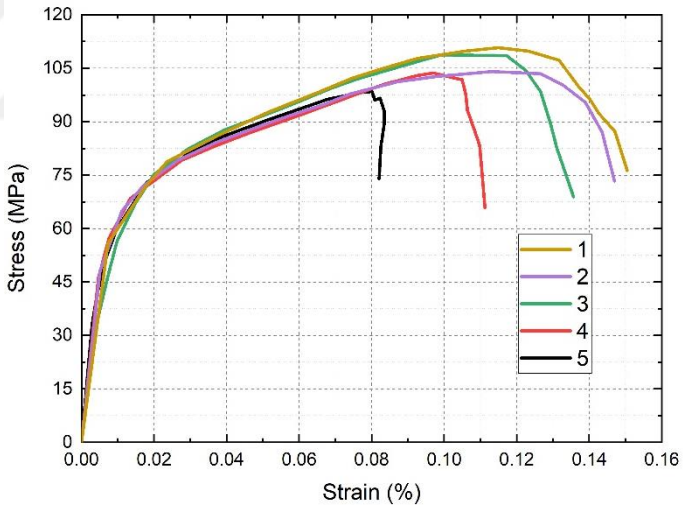

Figure 4.22 Stress-Strain Graph of the test specimens

Shear test results are given in Table 4.11 in detail. Average tensile strength is found 101.9 MPa for the specimens with [±45] fibre orientation.

Table 4.11 Test results for [±45] fibre orientation

Sample No	Shear Strength (MPa)	Elastic Modulus (GPa)	Strain at Break (%)
1	41.25	5.74	6.35
2	55.5	5.21	14.88
3	52	5.30	11.02
4	52.35	5.65	14.40
5	49.5	5.25	8.21
6	55.3	5.77	13.82
Avg.	**50.95**	**5.48**	**11.44**
St. Dev. (±)	**10.5**	**0.2**	**3.5**

4.5 Numerical modeling approach of composite structures under progressive failure

The commercial program Ls-Dyna is utilized to create the finite element model. Using this program, numerous studies examine the crushing response of fiber-reinforced plastic tubes.

4.5.1 Simulation Setup

MAT_54 and MAT_55 are used to model composite structures and they are very close in their formulations. Material 54 uses Chang matrix failure criterion (as Material 22), and material 55 uses the Tsay-Wu criterion for matrix failure. Material properties used to define the GFRP tube in MAT_54 are given below in Table 4.12.

Table 4.12 Material properties and tests required for MAT_54

Property	Description	Test	Standard
EA	Modulus in longitudinal (fiber) direction	0º tensile test	ASTM D3039
EB	Modulus in transverse direction	90º tensile test	ASTM D3039
PRCA	Major Poisson's ratio	0º tensile test	ASTM D3039
PRBA	Minor Poisson's ratio	90º tensile test	ASTM D3039
XT	Longitudinal tensile strength	0º tensile test	ASTM D3039
YT	Transverse tensile strength	90º tensile test	ASTM D3039
XC	Longitudinal compressive strength	0º compression test	ASTM 6641
YC	Transverse compressive strength	90º compression test	ASTM 6641
SC	Shear strength	Shear Test	ASTM D3518
G12	Shear Modulus	Shear Test	ASTM D3518

4.5.2 Finite Element Modeling

Three layers are used to model the composite tube in Ls-Dyna. Fully integrated shell elements with four nodes are used for the composite layers. The fully integrated elements are subject to hourglass control. Two through-thickness integration points defining two distinct stacking sequences are modeled for each layer. The upper and lower platens are modeled as two rigid surfaces during the deformation; the lower platen is mounted to the ground while the higher one is compressed at a speed of 0.2 mm/ms. Mass scaling is used to shorten the computational run time while ensuring that the model exhibits quasi-static deformation, where kinetic energy is less than 5% of internal energy as shown in Fig. 23 [96].

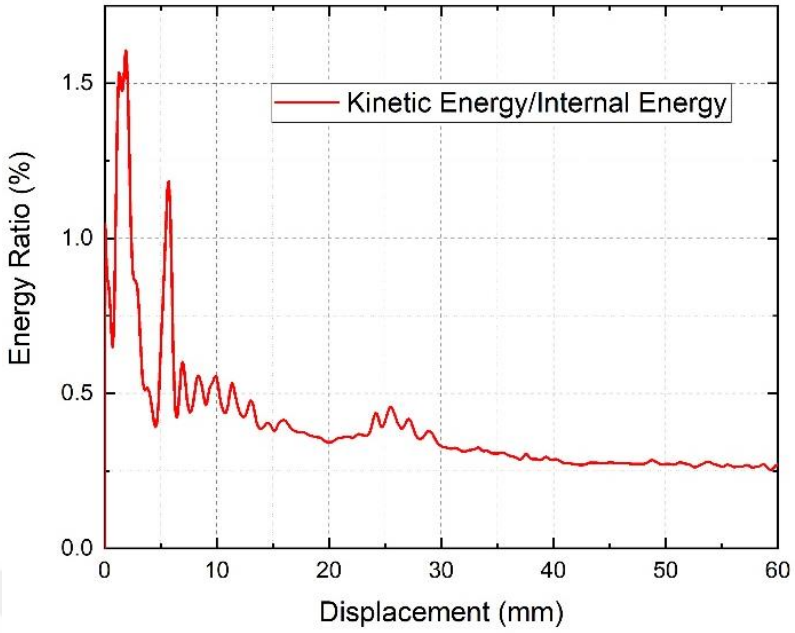

Figure 4.23 Ratio of kinetic energy to internal energy of the tube.

Fully integrated shell elements are used for the aluminum tube. The fully integrated elements with two through-thickness integration points are subjected to hourglass control.

Belytschiko-Tsay elements are used for the honeycomb. These elements with five through-thickness integration points are subjected to hourglass control.

The finite model of honeycomb-filled hybrid tubes, which was employed in the simulation, is depicted in Figure 4.24.

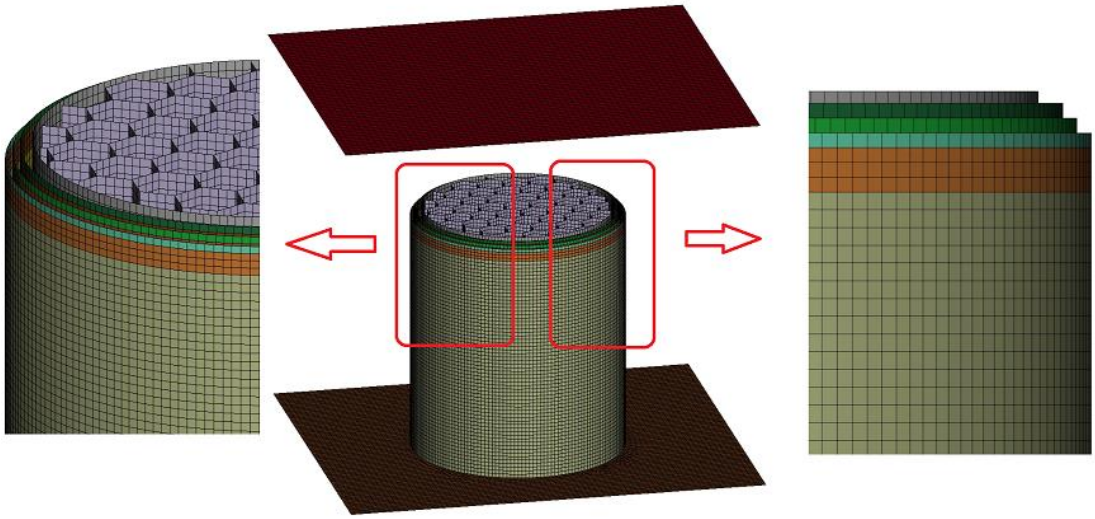

Figure 4.24 FEM Model of Hybrid Tube

Researchers employ the chamfer and trigger mechanism to generate a progressive deformation (Atthapreyangkul et al. [97], Siromani et al. [81], Huang and Wang [98], and Tong and Xu [82]). In the Ls-Dyna numerical models, the trigger mechanisms were included to improve progressive crushing. The orthotropic material model was utilized by Huang and Wang [98], Boria et al. [83, 84], Zhang et al. [80], Reuter et al. [99], Meriç and Gedikli [100], and Siromani et al. [81] using the MAT_54 "mat enhanced composite damage" card and the Chang-Chang failure criteria, whereas Tong and Xu [82] employed the material model 58 “mat_laminated_composite_fabric”. Huang and Wang [98] and Rabiee and Ghasemnejad [101] used trigger mechanisms in their models to control the crushing initiation.

Similar trigger mechanisms have been applied in the works of Huang and Wang [98] and Rabiee and Ghasemnejad [101], as well as in our investigation. In general, trigger mechanisms are used to reduce the initial peak force and achieve progressive failure. As shown in Fig. 4.25, one row element is designated as a trigger (length 1.25 mm) and three row elements are specified as neighbors of the trigger (length 3.75 mm) to be consistent with experimental results.

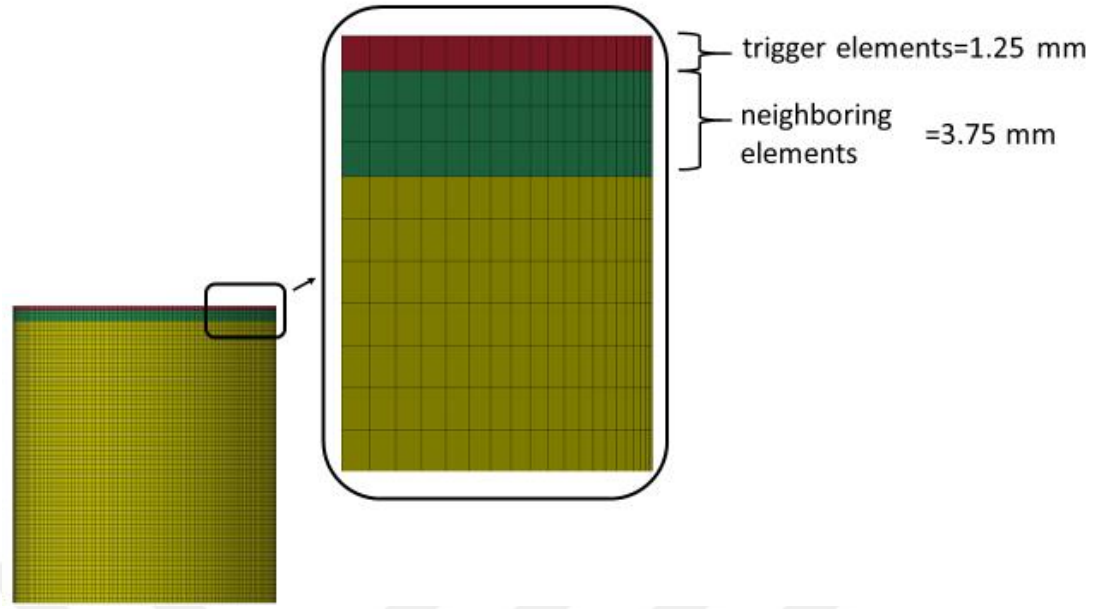

Figure 4.25 Trigger mechanism of tubes

The chamfer on the upper half of the tube that defines the trigger mechanism has a thickness of 0.8 mm. Although the investigation of Rabiee and Ghasemnejad [101] included 5°, 10°, and 15° inward-chamfering mechanisms, FEA results converged to experimental data when a 0° trigger chamfering mechanism is used.

The mesh size needs to be selected carefully in order to simulate the crushing behavior observed in simulations. To determine the appropriate mesh size for the accurate and efficient model, a mesh size sensitivity analysis is carried out. As illustrated in Fig. 4.26, the acceptable result was produced with elements of 1.5 mm in size for composite layers. For the elements maximum aspect ratio is equal to 1.01, minimum jacobian is found 1.0, maximum warpage is 0, minimum and maximum angle are 90 in the model. Also 90657 nodes and 92813 shell elements are created in foam-filled hybrid tube model.

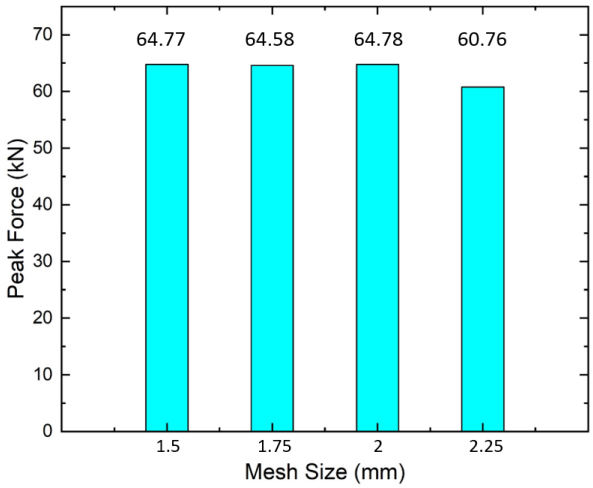

Figure 4.26 Mesh size sensitivity analysis

The automatic single surface contact algorithm puts the tube in contact with itself, while the automatic surfaceto-surface contact algorithm puts the upper plate and tube in contact. Additionally, the surface to surface contact method is used to simulate the interaction between the honeycomb and the aluminum tube. The friction coefficients for surface to surface contact algorithms are 0.25 for both static and dynamic friction. To specify how layers interact while simultaneously preventing interpenetration, tiebreak contact algorithms are used. The friction coefficients for tiebreak contact algorithms are 0.4 for both static and dynamic friction.

With choosing option 8, delamination between tube layers is modeled using the CONTACT_AUTOMATIC _SURFACE_TO_SURFACE_TIEBREAK card. This contact method states that failure occurs when the distance (PARAM), normal (NFLS), and shear (SFLS) stress levels all reach predetermined levels. Following a parametric study for the three-layer model, the tiebreak contact's maximum normal stress is set to 65 MPa, and its shear contact stress is set to 90 MPa. The contact distance parameter is set to 0.11 mm. Only for tiebreak contact between aluminum and GFRP tube, NFLS is set to 27 MPa and SFLS is set to 50 MPa to obtain consistent results with experiments for the hybrid tube model.

The deformation pattern of GFRP tubes is simulated using the MAT_ENHANCED_COMPOSITE_DAMAGE (MAT_54) material model in Ls-

Dyna. In MAT_54, data obtained from material tests are used, and numerical parameters are calibrated to model the deformation characteristics of crash boxes. Table 4.13 lists the material properties discovered through mechanical tests to use in the material model.

Table 4.13 Material parameters used in Ls-Dyna

Property	Description	Tests
ρ	Density	1.53 g/cm^3
EA	Modulus in longitudinal (fiber) direction	21.55 GPa
EB	Modulus in the transverse direction	6.92 GPa
G12	Shear modulus	5.48 GPa
PRCA	Major Poisson's ratio	0.24
PRBA	Minor Poisson's ratio	0.13
XT	Longitudinal tensile strength	469.1 MPa
XC	Longitudinal compressive strength	542 MPa
YT	Transverse tensile strength	45.8 MPa
YC	Transverse compressive strength	82.7 MPa
SC	Shear strength	50.95 MPa
Vf	Fiber volume fraction	33%

According to Chang- Chang criteria failure begins when the criteria given below are met [36]:

For the tensile fiber mode,

$$\left(\frac{\sigma_1}{XT}\right)^2 + \beta\left(\frac{\tau_{12}}{SC}\right)^2 - 1 \qquad \begin{cases} \geq 0 & failed \\ < 0 & elastic \end{cases} \tag{4.1}$$

For the compressive fiber mode,

$$\left(\frac{\sigma_1}{XC}\right)^2 - 1 \qquad \begin{cases} \geq 0 & failed \\ < 0 & elastic \end{cases} \tag{4.2}$$

For the tensile matrix mode,

$$\left(\frac{\sigma_2}{YT}\right)^2 + \left(\frac{\tau_{12}}{SC}\right)^2 - 1 \qquad \begin{cases} \geq 0 & failed \\ < 0 & elastic \end{cases} \tag{4.3}$$

For the compressive matrix mode,

$$\left(\frac{\sigma_2}{2SC}\right)^2 + \left[\left(\frac{Y_C}{2SC}\right)^2 - 1\right] + \frac{\sigma_2}{YC} + \left(\frac{\tau_{12}}{SC}\right)^2 - 1 \qquad \begin{cases} \geq 0 & failed \\ < 0 & elastic \end{cases} \tag{4.4}$$

where XT is longitudinal tensile strength, XC is compressive tensile strength, SC is shear strength, and YT is transverse tensile strength.

Strain parameters and non-physical tunable parameters are the majority of the failure parameters in material card. When the failure criterion is reached, the element is kept under control until the failure strain is surpassed, at which point it is removed. The maximum strain for fiber compression (DFAILC), maximum strain for fiber tension (DFAILT), maximum strain for matrix straining (DFAILM), and maximum tensorial shear strain (DFAILS) are the four material model characteristics that are studied during the calibration process. It should be noted that the maximum matrix strain is determined for both compression and tension. If the maximum strains are defined in the material card, the strain-to-failure criterion is activated. In order to prevent the elements from being eliminated, it is usually advisable to set the maximum strains. Low values of DFAILM drastically affect the stability of the crush simulation, whereas raising DFAILM significantly above the level that produces a stable model has no negative effects on the crush simulation. The failure strains DFAILS and DFAILT are variables that are related to stability. In terms of the force-displacement curve and deformation views, these parameters are raised until consistency is noticed. The DFAIL values are confirmed to be as follows DFAILC = -0.7, DFAILM = 0.85, DFAILT=0.05, and DFAILS = 0.3. The adopted values are TFAIL=0 and EFS=0.

To employ the laminated shell theory in the estimations of laminate stiffness through the thickness, the LAMSHT variable on the CONTROL_SHELL card is activated. BETA and ALPH are both set to 0. When the matrix fails, the compressive and tensile strengths are reduced in the direction of the fiber using the strength-decreasing equations YCFAC and FBRT. The adopted values are FBRT = 1.0 and YCFAC = 2.0 [29]. NFAIL parameters are activated for element deletion in the FE model.

In the experiments, aluminum tubes made of the 6082-T6 material are employed, and MAT_24 (PIECEWISE_LINEAR_PLASTICITY) is used to model in Ls-Dyna[1]. The material has a density of ρ=2.6 kg/m^3, a Poisson's ratio of υ=0.3, and Young's modulus of E = 69 GPa [37]. Additionally, the data given in Table 4.14 is used in MAT_24 to define the true stress- true effective plastic strain curve. Similar to that, aluminum honeycomb which has a cell size of 10.39 mm is modeled using MAT-24 material card. The mechanical properties are provided by the manufacturer as; yield strength σ_y=150 MPa, the Poisson's ratio was υ=0.3, and the Youngs modulus was E=298 MPa.

Table 4.14 True stress- true effective plastic strain values defined in the MAT_24 card in Ls-Dyna [37]

σ_t (MPa)	145	149	157	168	171
ε_P	0.0	0.0158	0.0331	0.586	0.0664

4.5.3 Simulation Results

For the purpose of comparing the results obtained from FEA and experiments, energy absorption results and force-displacement graphs are provided. The findings shown in tables and figures demonstrate how well the FEA results can predict the crashworthiness capacity of the GFRP and hybrid tubes under quasi-static loading.

Images are taken at different time intervals while compressing the aluminum tubes. These images are then compared with the images obtained by the finite element model in Ls-Dyna and images are given in Figure 4.27.

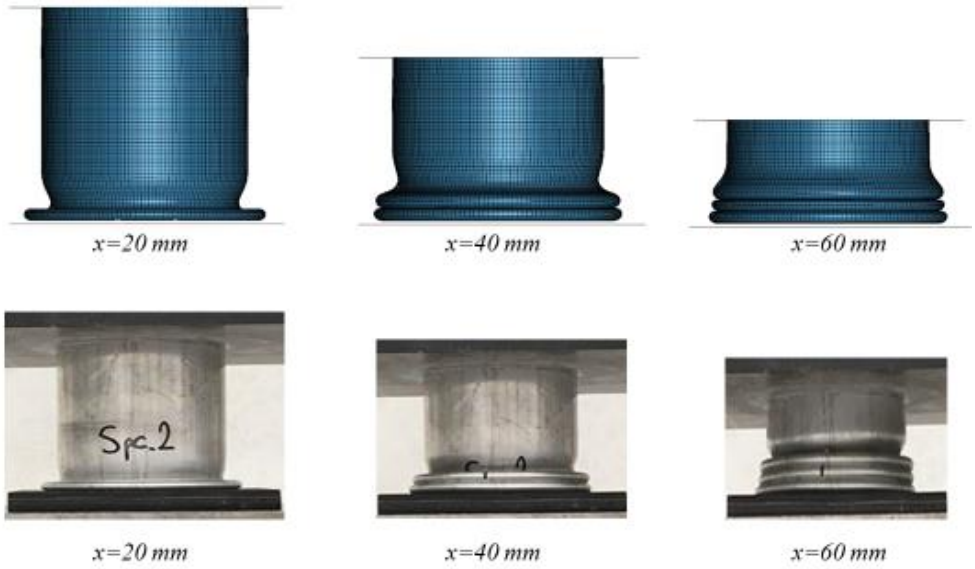

Figure 4.27 Comparison of collapse modes of aluminum tubes between experimental and FEA results

The load-displacement graphs of aluminum tubes shown in Figure 4.28 are used to calculate the energy absorption values given in Table 4.15. The FEA curve is sufficiently consistent with the experimental results.

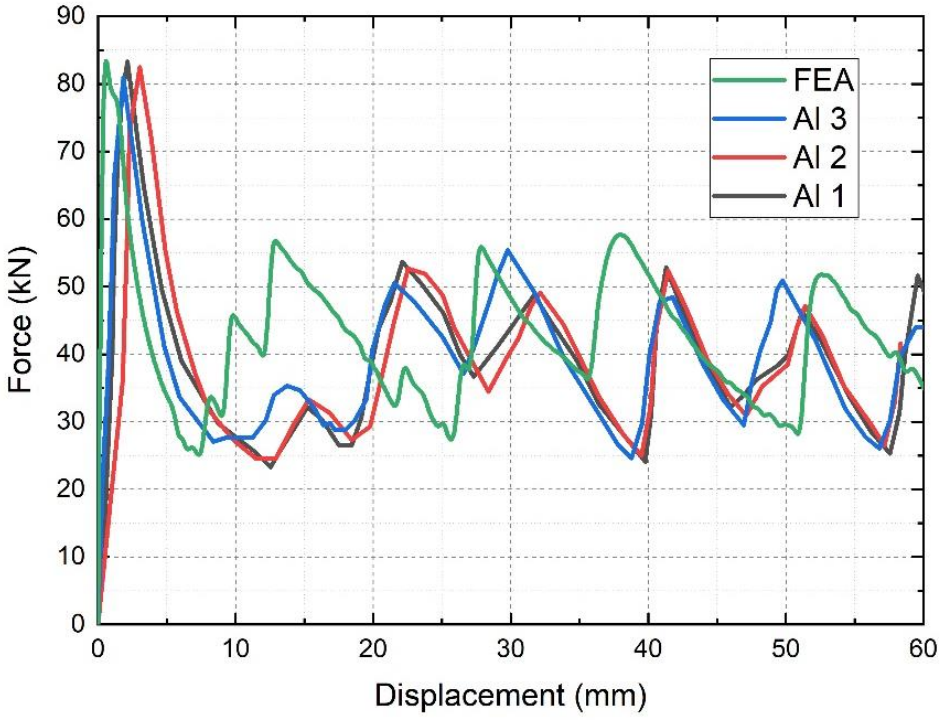

Figure 4.28 Crushing load–displacement curves for aluminum tubes

Table 4.15 compares the FEA results with the experiments and shows that the FE model is consistent with the experiments. The average energy absorption value for the aluminum tubes is 2.308 kJ for the experiments and 2.565 kJ is calculated according to the FE model. FE model has errors of -8.5% and 11.1% for CFE and SEA, respectively.

Table 4.15 Comparison of energy absorption values between simulation and experimental results of Al tubes

	Peak force (kN)	Mean force (kN)	CFE	EA (kJ)	Mass (kg)	SEA (kJ/kg)
Al1	83.28	39.38	0.46	2.363	0.123	19.21
Al2	82.45	36.67	0.46	2.200	0.127	17.32
Al3	80.88	39.35	0.48	2.361	0.125	18.89
Ave	82.20	38.46	0.47	2.308	0.125	18.47
FEA	82.36	42.75	0.51	2.565	0.125	20.52
Error (%)	-1.4	11.1	-8.5	11.1	0	11.1

Under axial loading, three GFRP circular tubes with 2.76 mm wall thickness were tested. As a result of the compression, bundle fracture and fronds develop as can be seen in Figure 4.29. Laminate bundles curved in and out along the middle of the wall. Similar to the results of the research conducted by Chen et al. [38], crushing energy is dissipated by transverse shearing and crack propagation between the bundles and the upper plate. Delaminations, fragmentations, and fractures of fiber bundles are observed in lamina fronds.

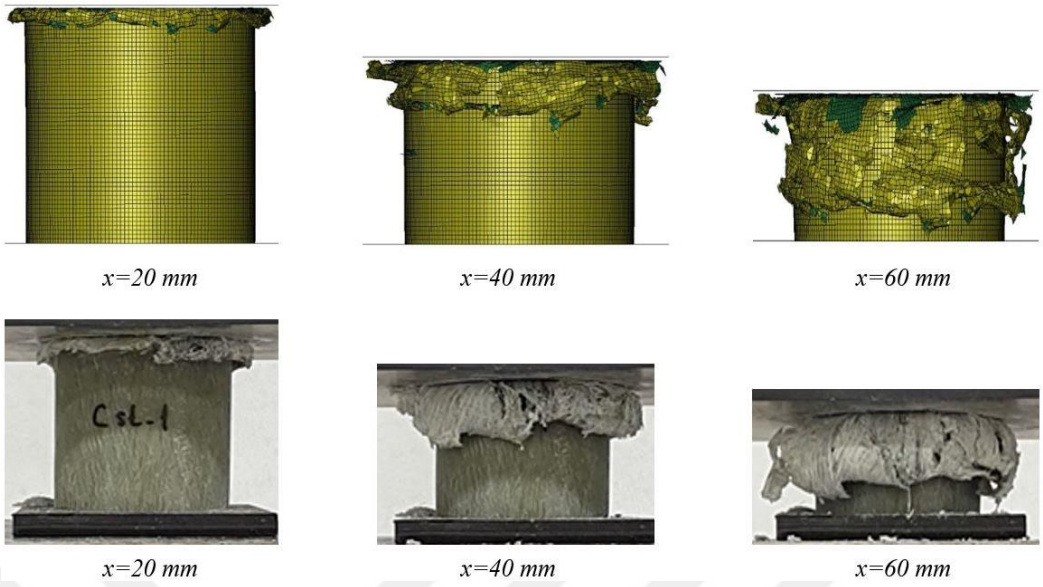

Figure 4.29 Comparison of collapse modes of GFRP tubes between experimental and FEA results

A comparison of the deformation images of GFRP tubes acquired through models and experiments is shown in Figure 4.29. The force-displacement behavior of specimen #1 was incompatible with the other two specimens, despite the fact that deformation patterns were similar for all three GFRP specimens. As a result, it wasn't taken into account while calculating the crashworthiness metrics' average values. The force-displacement graphs are compared in Figure 30.

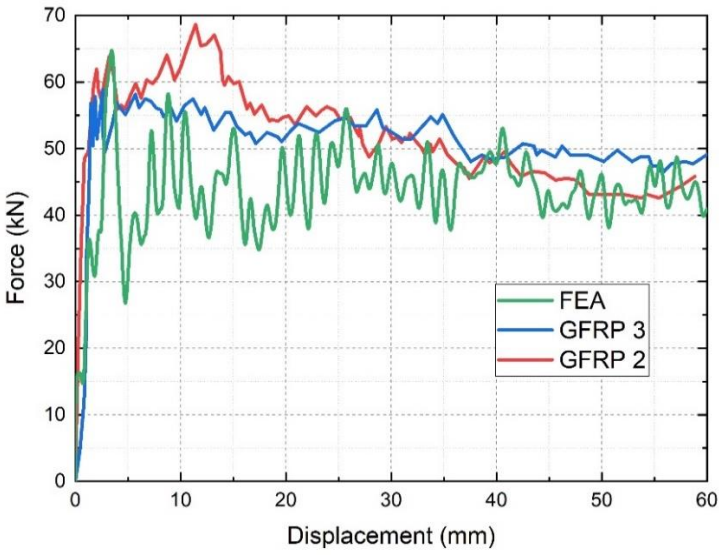

Figure 4.30 Crushing load-displacement curves for GFRP crash boxes

The results of the experiments and the FE model are compared in Table 4.16. The FE model exhibits good accuracy when compared to experimental crashworthiness properties. The SEA of the model is 25.236 kJ/kg while the average SEA of the test specimens is 29.276 kJ/kg, and the relative error is 13.8%. The EA of the model is 2.675 kJ whereas the EA of the test specimens is 3.074 kJ, and the relative error is 13%.

Table 4.16 Comparison of energy absorption values between simulation and experimental results of GFRP tubes

	Peak force (kN)	Mean force (kN)	CFE	EA (kJ)	Mass (kg)	SEA (kJ/kg)
GFRP1	74.96	66.07	0.88	3.964	0.116	34.172
GFRP2	61.96	50.68	0.82	3.041	0.104	29.240
GFRP3	56.81	51.08	0.91	3.108	0.106	29.320
Ave	59.39	51.23	0.86	3.074	0.105	29.276
FEA	64.77	44.58	0.69	2.675	0.106	25.236
Error (%)	9.1	-13.0	-19.8	-13.0	0.95	-13.8

According to bundle formation and delamination seen in FEM, specimens show a crushing failure process. According to the test results for 60 mm deformed views presented in Fig. 4.31, collapse mechanisms for GFRP tubes are determined to be compatible. Both in the test specimens and the finite element model, lamina fronds and fiber bundle fractures are visible. Inward and outward deformation occur in the lamina bundles. There is a steady progression of damage. FEM is consistent with the test results in terms of failure and delamination modes.

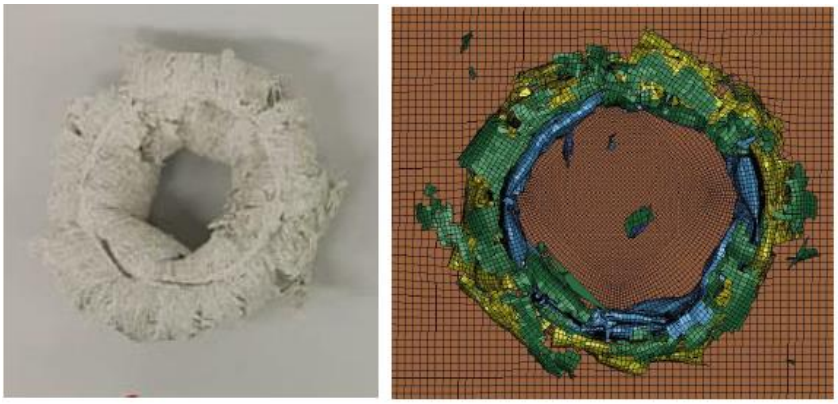

Figure 4.31 Final failure views of GFRP Tubes

Hybrid Tubes

The deformed views of hybrid specimens at displacements of 20, 40, and 60 mm are shown in Fig. 4.32. Cracks and bundles begin at the top of the tubes. Due to the presence of an aluminum tube inside, the lamina bundles deform outward. The FEA model also exhibits delamination and fracture that spread along the axial direction. A longitudinal inter-laminar crack causes brittle deformation of the hybrid tube. Additionally, the load reduction following the measured peak force is the main distinction between the force-displacement behavior of the GFRP and the hybrid tubes. In hybrid tubes, the second peak force comes at a 20 mm tube deflection caused by the internal aluminum tube folding. Although the third peak is not clearly visible for specimen 3, the third folding of an aluminum tube results in the third peak force for hybrid tube specimens 1 and 2.

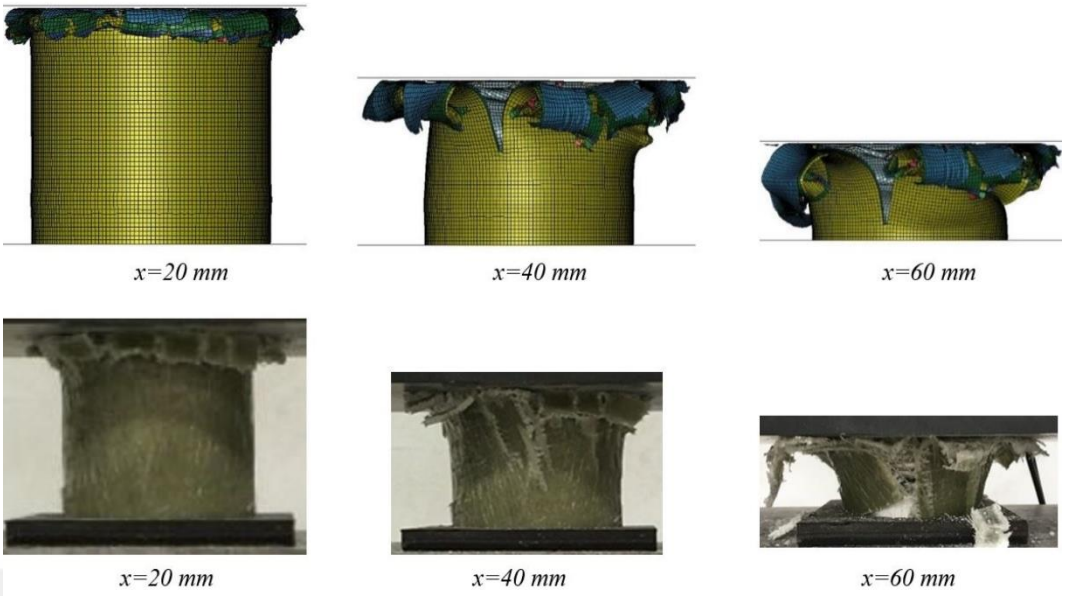

Figure 4.32 Comparison of collapse modes of hybrid tubes between experimental and FEA results

As seen in Fig. 4.33, all specimens have a consistent force-displacement graph. The presence of aluminum tube inside causes the crushed lamina bundles to deform outward. Additionally, comparable to the test specimens, the FEA model exhibits delamination and fracture that progressed in the axial direction. Longitudinal inter-laminar cracks spread throughout the hybrid tube when it deforms in a brittle manner. In contrast to GFRP tubes, which exhibit bundles as a result of gradual failure, hybrid tubes achieve energy absorption through both crack formation and outward delamination.

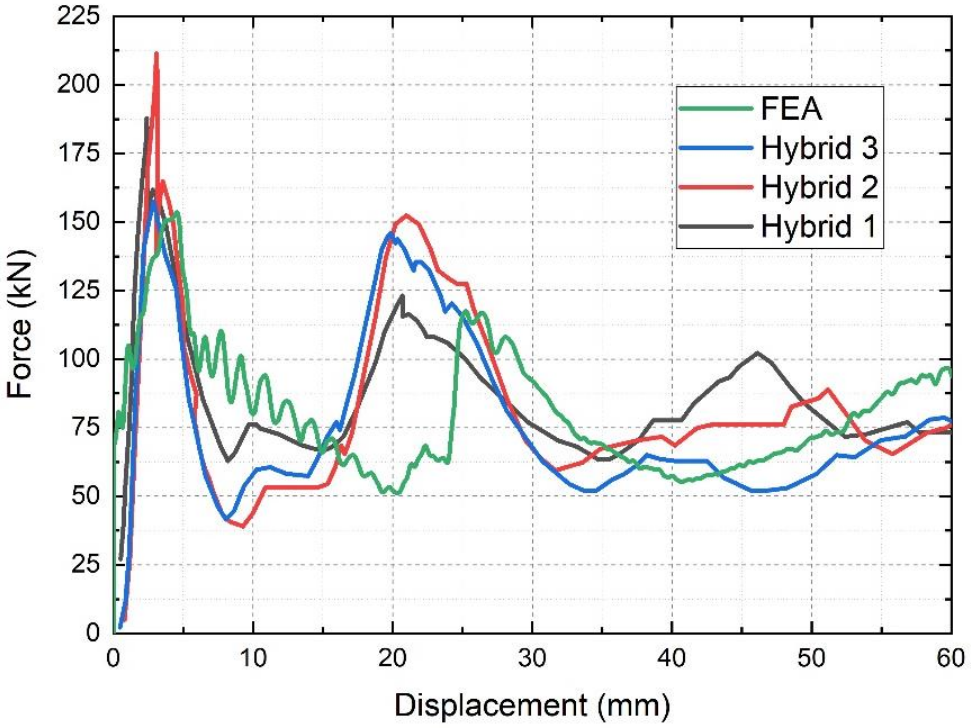

Figure 4.33 Crushing load–displacement curves for hybrid tubes

As illustrated in Fig. 4.33, the force-displacement graph of the FEM for the hybrid tube exhibits a lower initial peak load than the test specimens. The axial force increases throughout the initial stage of deformation for both FEM and tests, reaching a peak value of about 185 kN. After the initial peak force is noticed, the crash force decreases to approximately 65 kN and increases to a second peak force of around 140 kN for the average experimental results. However, the second peak value for the FE model is 117 kN.

Table 4.17 Comparison of energy absorption values between simulation and experimental results of hybrid tubes

	Peak force (kN)	Mean force (kN)	CFE	EA (kJ)	Mass (kg)	SEA (kJ/kg)
Hybrid1	187.76	85.95	0.46	5.157	0.218	23.655
Hybrid2	211.38	82.45	0.39	4.947	0.218	22.693
Hybrid3	157.45	76.32	0.48	4.579	0.211	21.702
Ave	185.53	81.57	0.44	4.894	0.216	22.657
FEA	153.54	82.08	0.53	4.925	0.230	21.414
Error (%)	-17.2	0.6	20.4	0.6	6.5	-5.5

FEA and test results of hybrid tubes are compared in Fig. 4.33 and Table 4.17, and it was discovered that the FEA results agree with the test results. The average SEA of test specimens is 22.657 kJ/kg, with a -5.5% error, as compared to the SEA obtained via FEA, which is 21.414 kJ/kg. Fig. 4.34 displays the deformed views of hybrid tubes with 60 mm crushing displacement. When the hybrid tube distorted axially, folding for aluminum tubes and splitting cracks for GFRP wraps are observed for both test specimens and the FE model. The numerical results prove the accuracy of the FE approach of the quasi-static crash process of GRFP and hybrid tubes.

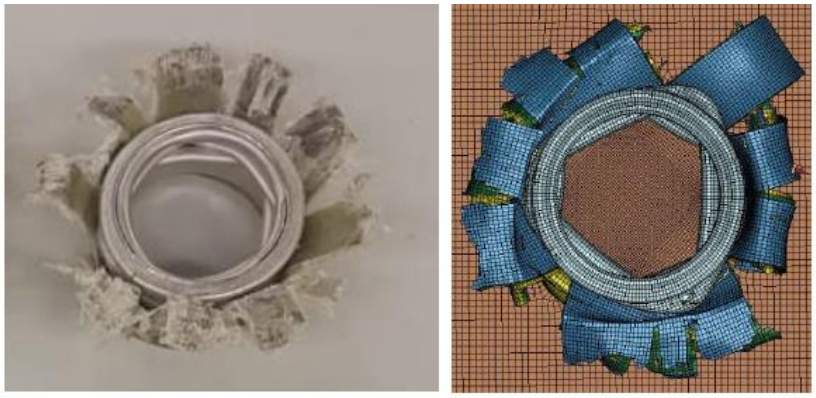

Figure 4.34 Final Views of Hybrid Tubes

Honeycomb-filled Hybrid Tubes

Figure 4.35 illustrates the numerical and experimental views of honeycomb-filled hybrid tubes with corresponding deformations of 20 mm, 40 mm, and 60 mm.

Additional observations reveal that the FEM results are consistent with the experimental results according to the force-displacement graph and deformed views of the tubes. As seen in Fig. 4.35, specimens demonstrate a failure phase that involves cracks and delamination.

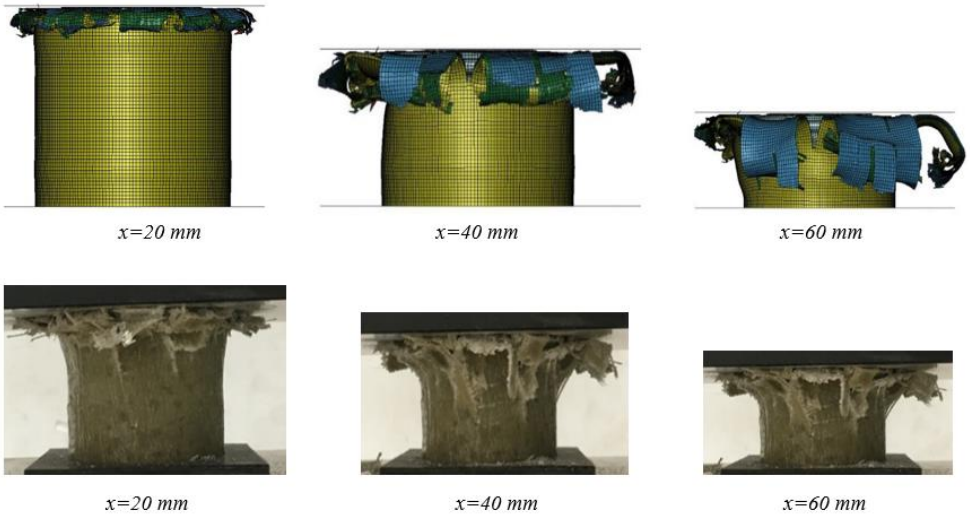

Figure 4.35 Comparison of collapse modes of honeycomb-filled hybrid tubes between experimental and FEA results

In terms of collapse modes, Fig. 4.35 illustrates the similar crushing response and collapse mechanism between the FEM and test results of tubes filled with honeycomb.

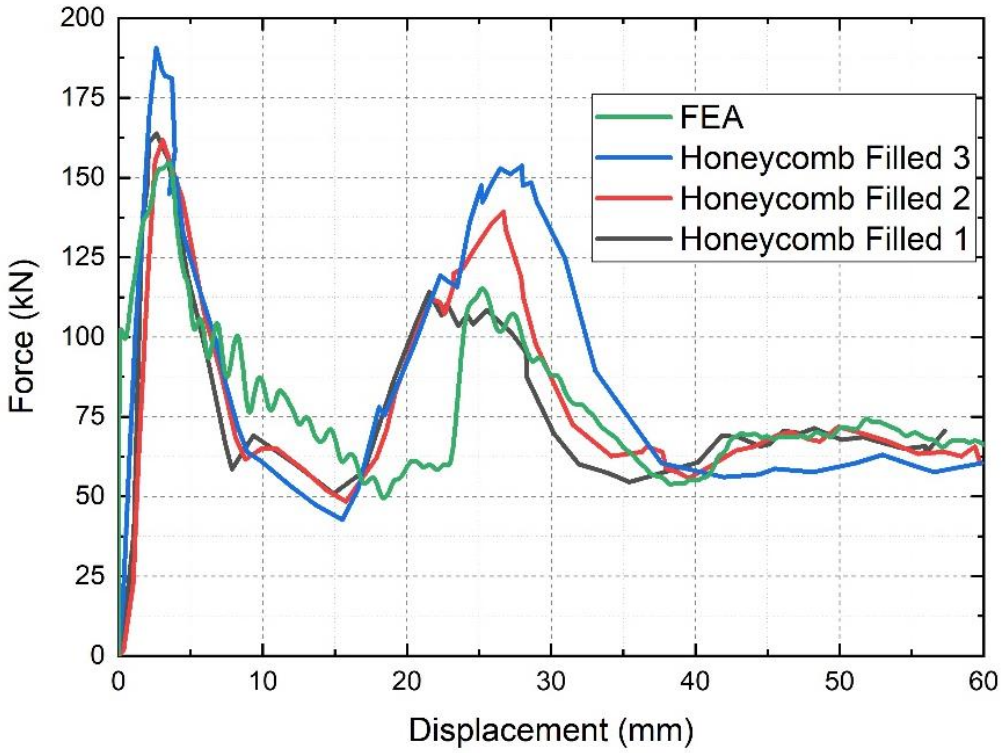

Figure 4.36 Crushing load–displacement curves for honeycomb-filled hybrid tubes

The load-displacement curves of the honeycomb-filled hybrid tubes are given in Fig.4.36. It is apparent that delamination and fracture begin before 20 mm of deformation. Experiments show that the axial force increases at the beginning of deformation and peaks at 170 kN, comparable to the empty hybrid tubes. Crash force drops after the first peak force is viewed, then rises to a second peak force about 135 kN.

Table 4.18 provides the mean force, initial peak force, EA, and SEA of the tubes. The average SEA of test specimens is 19.634 kJ/kg, with a -0.3% error, as compared to the SEA obtained via FEA, which is 19.580 kJ/kg. The results reveal that adding honeycomb to the hybrid tubes does not improve energy absorption.

Table 4.18 Comparison of energy absorption values between simulation and experimental results of honeycomb-filled hybrid tubes

	Peak force (kN)	Mean force (kN)	CFE	EA (kJ)	Mass (kg)	SEA (kJ/kg)
Honey1	161.01	72.58	0.45	4.355	0.238	18.298
Honey2	161.76	77.91	0.48	4.675	0.238	19.642
Honey3	190.64	83.18	0.44	4.991	0.239	20.882
Ave	171.14	77.88	0.46	4.673	0.238	19.634
FEA	154.76	79.30	0.51	4.758	0.243	19.580
Error (%)	-9.6	1.8	10.9	1.8	2.1	-0.3

As seen in FEM, the test specimen shows a crushing failure process in terms of bundles and cracks. The test results for 60 mm deformed views, as shown in Fig. 4.37, are found to be compatible for the failure mechanisms for honeycomb-filled tubes.



Figure 4.37 Final Views of Honeycomb-filled Hybrid Tubes

Crash load increases at a peak force of about 170 kN at the beginning of deformation for both non-filled and honeycomb-filled hybrid tubes, which is higher than the mean

crash force. As seen in Figs. 4.34 and 4.37, after the initial failure occurs, the crash force decreases and stays around the mean crash force after the second peak force is noticed.

Honeycomb-filled hybrid tubes had lower EA and SEA than empty tubes. Additionally, it is discovered that the mean force and first peak force values obtained for tubes filled with honeycomb are comparable to those for tubes that aren't filled. The deformation behavior and energy absorption capacity of hybrid tubes are unaffected by the honeycomb filling. Because of this, honeycomb filling is not a good solution for enhancing SEA and EA of hybrid tubes.

4.6 Conclusion

The quasi-static test response of GFRP, empty and honeycomb-filled hybrid tubes are studied experimentally and numerically. The primary goal of this thesis is to describe how GFRP and hybrid tubes behave in terms of crashworthiness.

The important findings can be summarized as follows:

-In the experimental section, all specimens demonstrated progressive failure mechanisms.

-Due to lower density and mass of the GFRP, SEA is superior for empty composite tubes. Composite tubes have a lower EA than hybrid tubes, nevertheless.

-Due to the minimal change in mass and mechanical properties, the honeycomb filler inside the hybrid tubes did not lead to different deformation patterns.

-Applying trigger mechanisms in the FE model of composite circular tubes makes it possible to capture the deformation process and obtain consistent crashworthiness values with experimental data.

-The element size and type utilized in the FE model are crucial in successfully modeling the crash tests of thin-walled tubes.

-The CFE and SEA of empty GFRP tubes are 83% and 59% greater than those of empty Al tubes, respectively when the crashworthiness performances of empty Al and empty GFRP tubes are compared.

-It is discovered that the CFE of the empty hybrid tube is 6% lower than the CFE of the empty Al tube when the crashworthiness performances of the empty Al and empty hybrid tubes are compared.

-The CFE and SEA of the empty composite tube are 95% and 29% higher than the empty hybrid tube, respectively, when the crashworthiness performances of the empty composite and empty hybrid tubes are compared.

-It is discovered that the CFE of an empty hybrid tube is 2% lower than that of an empty Al tube when the crashworthiness performances of empty Al and honeycomb-filled hybrid tubes are compared. A hybrid tube filled with honeycomb has a SEA that is 6% higher than an Al tube that is empty.

-It is discovered that the CFE of the honeycomb-filled hybrid tube is 4.5% greater than the empty hybrid tube when the crashworthiness performances of empty and honeycomb-filled hybrid tubes are compared. The SEA of a hybrid tube with honeycomb inside is 13% smaller than that of an empty hybrid tube.

-Empty GFRP composite tubes were determined to have the best performance overall in terms of CFE and SEA. GFRP composites' lower bulk and density could be to reason for this.

CHAPTER 5

SUMMARY, CONCLUSIONS, AND FUTURE WORK

5.1 Summary

This chapter offers a thorough summary of the entire investigation, summarizes the conclusions of the thesis, and connects the findings from several chapters.

In the first stage of the study, the experimental results of empty and foam-filled multi-cell aluminum 6061 tubes were confirmed by finite element analysis via Ls-Dyna.

In the second stage of the study, aluminum 6082, GFRP, and hybrid tubes were tested and their energy absorption characteristics were investigated experimentally. The results obtained from the experimental studies were confirmed by finite element analysis. At the last stage of the study, with the successful completion of the verification studies, empty hybrid tubes were compared with honeycomb-filled tubes in terms of energy absorption parameters.

5.2 Conclusions

The results obtained for the aluminum multi-cell tubes are summarized below:

- To effectively simulate the crash tests of thin-walled aluminum multi-cell tubes, the material model utilized in the FE model is crucial. By specifying suitable contact mechanisms and boundary conditions, the FE model provides energy absorption parameters that are consistent with experimental results.
- When foam characteristics and geometrical properties are defined, an empirical formula may forecast the mean force values of multi-cell tubes that are both empty and filled with foam.
- In terms of CFE and EA, both foam-filled multi-cell tube designs performed significantly better than empty multi-cell tubes.
- FE model predicts the energy absorption parameters with less than 20% relative error.

- Empirical formula calculates the mean forces of empty multi-cell tubes with less than 5% relative error. Also, the formula calculates the mean forces of foam-filled multi-cell tubes with less than 15% relative error.

The results obtained for the GFRP and hybrid tubes are summarized below:

- The circular tubes deformed axially as a result of the compression tests and provided energy absorption as expected.
- Under quasi-static loading, GFRP tubes significantly performed better specific energy absorption compared to aluminum tubes.
- To improve energy absorption, aluminum tubes were wrapped with GFRP to obtain hybrid tubes. Hybrid circular tubes absorbed more energy than aluminum and composite tubes.
- The honeycomb filling of hybrid tubes has no impact on their deformation behavior or ability to absorb energy.
- A 3-layer shell configuration with MAT_54 material card in Ls-Dyna provided accurate results with a low computational cost. This model was capable to predict the energy absorption parameters and the evolution of damage.
- Applying a fine-tuned trigger mechanism to the composite tubes can produce FEA results that nearly resemble the deformation process that occurs during the axial crashing of the tubes.

For the crashworthiness of composite constructions made of shell and cohesive parts, Ls-Dyna is widely used. Researchers employ cohesive zone models to better forecast deformations and detect cracks in materials. To improve and expand the use of the software, more material models are being added to its database. Because MAT_54 needs a small number of measurable material input parameters, it is frequently employed in dynamic failure simulations. The simplified material model MAT_22 is improved in the material card MAT_54. The failure can occur in tensile fiber mode, compressive fiber mode, tensile matrix mode, or compressive matrix mode. A

crashfront algorithm, which provides a softening factor to the strength in the elements of the crashfront, may be implemented in addition to the usual material behavior. This can be employed to curb progressive failure and decrease global buckling. The function DEFINE_CURVE allows the model to incorporate strain rate dependent strength. Shells, thick-shelled elements, and solid elements can all use the material models. MAT_54 material model can be applied with few calibration for satisfactory aggrement with experimental data. Other models for composites such as MAT_58, MAT_59, MAT_116, MAT_162 or MAT_262 require extensive calibration to achieve correlation with test results.

5.3 Future Works

In this study, the built-in material models in the material library of the Ls-Dyna commercial software were examined for the simulation of the quasi-static loading process, and it was found that the MAT_54 material model can be used to model GFRP tubes.

-Various foams of different densities can be produced and placed inside hybrid crash boxes.

- Energy dissipation characteristics can be compared by placing different metallic and non-metallic foam materials inside the designed crash boxes.

- In the continuation of the study, the optimization of the designed collision boxes can be made.

-CFRP tubes and aluminum wrapped CFRP tubes can be produced and compressed axially to investigate crashworthiness parameters.

REFERENCES

[1] Baroutaji, A., Sajjia, M., & Olabi, A. G., On the crashworthiness performance of thin-walled energy absorbers: recent advances and future developments. *Thin-Walled Structures*, *118*, 137-163, 2017.

[2] Kocaoğlu B., Investigation of the Effect of Aluminium in Different Alloys Placed in Collision Boxes on the Strength, Unpublished masters dissertation, Karabük University, 2021.

[3] Dubey, R., Jayaganthan, R., Ruan, D., Gupta, N. K., Jones, N., & Velmurugan, R., Energy absorption and dynamic behaviour of 6xxx series aluminium alloys: A review. *International Journal of Impact Engineering*, 104397, 2022.

[4] Albayrak M., Eğri yüzeylere sahip kauçuk takviyeli kompozitlerin darbe davranışlarının araştırılması, Unpublished doctoral dissertation, Fırat Üniversitesi, 2022.

[5] Altin, M, Acar, E., & Güler, M. A., Foam filling options for crashworthiness optimization of thin-walled multi-tubular circular columns. *Thin-Walled Structures*, *131*, 309-323, 2018.

[6] Ask, S., & Sellgren, A. Evaluation of strain path independent material models for failure prediction in sheet metals using LS-DYNA, Unpublished masters dissertation, Chalmers University, 2016.

[7] Li, Z., Chen, R., & Lu, F., Comparative analysis of crashworthiness of empty and foam-filled thin-walled tubes. *Thin-Walled Structures*, *124*, 343-349, 2018.

[8] Baroutaji, A., Sajjia, M., & Olabi, A. G., On the crashworthiness performance of thin-walled energy absorbers: recent advances and future developments. *Thin-Walled Structures*, *118*, 137-163, 2017.

[9] Langseth, M., & Hopperstad, O. S., Static and dynamic axial crushing of square thin-walled aluminium extrusions. *International Journal of Impact Engineering*, *18*(7-8), 949-968, 1996.

[10] Al Galib, D., & Limam, A., Experimental and numerical investigation of static and dynamic axial crushing of circular aluminum tubes. *Thin-Walled Structures*, *42*(8), 1103-1137, 2004.

[11] Simhachalam, B., Rao, C. L., & Srinivas, K., The effect of holes on the dynamic behavior and energy absorption of aluminum alloy AA7005 Tube. In *Applied Mechanics and Materials* (Vol. 446, pp. 325-328). Trans Tech Publications Ltd, 2014.

[12] A. Alavi Nia, M. Parsapour Comparative analysis of energy absorption capacity of simple and multi-cell thin-walled tubes with triangular, square, hexagonal and octagonal sections, *Thin-Walled Struct*., 74, pp. 155-165, 2014.

[13] An X., Gao Y., Fang J., Sun G., Li Q., Crashworthiness design for foam-filled thin-walled structures with functionally lateral graded thickness sheets. *Thin-Walled Struct*., 91:63–71, 2015.

[14] Attia M., Meguid S., Nouraei H., Nonlinear finite element analysis of the crush behaviour of functionally graded foam-filled columns. Finite Elements Anal Des; 61:50–9, 2012.

[15] Djamaluddin F., Abdullah S., Ariffin A, Nopiah Z., Optimization of foam-filled double circular tubes under axial and oblique impact loading conditions. *Thin-Walled Struct.*, 87:1–11, 2015.

[16] Hanssen A., Hopperstad O., Langseth M., Ilstad H., Validation of constitutive models applicable to aluminium foams. *Int J Mech Sci*; 44(2):359–406, 2002.

[17] Onsalung N., Thinvongpituk C., Pianthong K., Impact response of circular aluminum tube filled with polyurethane foam. Mater Trans; 55(1):207–15, 2014.

[18] Mohammadiha O., Ghariblu H., Crush behavior optimization of multi-tubes filled by functionally graded foam. *Thin-Walled Struct*., 98:627–39, 2016.

[19] Mohammadiha O., Beheshti H., Aboutalebi FH., Multi-objective optimisation of functionally graded honeycomb filled crash boxes under oblique impact loading. *Int J Crashworthiness*; 20(1):44–59, 2015.

[20] Zarei H., Kröger M., Optimum honeycomb filled crash absorber design. *Mater Des*.; 29(1):193–204, 2008.

[21] Gao Q., Wang L., Wang Y., Wang C., Crushing analysis and multiobjective crash-worthiness optimization of foam-filled ellipse tubes under oblique impact loading. *Thin-Walled Struct*.; 100:105–12, 2016.

[22] Kılıçaslan C., Numerical crushing analysis of aluminum foam-filled corrugated sin- gle-and double-circular tubes subjected to axial impact loading. *Thin-Walled Structures*; 96:82–94, 2015.

[23] Qi C., Yang S., Crashworthiness and lightweight optimisation of thin-walled conical tubes subjectedto an oblique impact. *Int J Crashworthiness*; 19(4): 334–51, 2014.

[24] Ahmad Z., Thambiratnam D., Crushing response of foam-filled conical tubes under quasi-static axial loading. *Mater Des*.; 30(7): 2393–403, 2009.

[25] A.K. Toksoy, M. Güden, The optimisation of the energy absorption of partially al foam-filled commercial 1050h14 and 6061t4 al crash boxes *Internat J Crashworthiness*, 16 (1), pp. 97-109, 2011.

[26] M. Altin, M.A. Güler, S.K. Mert, The effect of percent foam fill ratio on the energy absorption capacity of axially compressed thin-walled multi-cell square and circular tubes, Int. J. Mech. Sci., 131, pp. 368-379, 2017.

[27] H. Nikkhah, F. Guo, Y. Chew, J. Bai, J. Song, P. Wang, The effect of different shapes of holes on the crushing characteristics of aluminum square windowed tubes under dynamic axial loading, *Thin-Walled Struct*, 119 , pp. 412-420, 2017.

[28] Zhang X., Cheng G., A comparative study of energy absorption characteristics of foam-filled and multi-cell square columns, Int. J. *Impact Eng*., 34, pp. 1739-1752, 2007.

[29] Kim, S. B.; Huh, H.; Lee, G. H.; Yoo, J. S.; Lee, M. Y., Design of the Cross Section Shape of an Aluminum Crash Box for Crashworthiness Enhancement of a CAR, International Journal of Modern Physics B, Volume 22, Issue 31-32, pp. 5578-5583, 2008.

[30] A. Reyes, M. Langseth, O.S. Hopperstad; Square aluminum tubes subjected to oblique loading, Int. J. *Impact Eng*., 28 (10), pp. 1077-1106, 2003.

[31] J. Qiao, J. Chen, H. Che, Crashworthiness assessment of square aluminum extrusions considering the damage evolution, *Thin-walled Struct*, 44, pp. 692-700, 2006.

[32] J. Marzbanrad, A. Keshavarzi, F.H. Aboutalebi, Influence of elastic and plastic support on the energy absorption of the extruded aluminium tube using ductile failure criterion, *Int. J. Crashworthiness*, 19 (2), pp. 172-181, 2014.

[33] H. Hooputra, H. Gese, H. Dell, H. Werner, A comprehensive failure model for crashworthiness simulation of aluminium extrusions, *Int J Crashworthiness*, 9 (5), pp. 449-464, 2004.

[34] Allahbakhsh, H. R., Saemi, J., & Hourali, M. Design optimization of square aluminium damage columns with crashworthiness criteria. *Mechanics*, *17*(2), 187-192, 2011.

[35] Quirino Estrada, Dariusz Szwedowicz, Jesús Silva-Aceves, Tadeusz Majewski, JulioVergara-Vazquez, AlejandroRodriguez-Mendez, Crashworthiness behavior of aluminum profiles with holes considering damage criteria and damage evolution, *International Journal of Mechanical Sciences* 131–132, pp.776-791, 2017.

[36] Estrada, Quirino, Dariusz Szwedowicz, Alejandro Rodriguez-Mendez, Oscar A. Gómez-Vargas, Milton Elias-Espinosa, and Jesús Silva-Aceves. "Energy absorption performance of concentric and multi-cell profiles involving damage evolution criteria." *Thin-Walled Structures* 124: 218-234, 2018.

[37] Quirino Estrada, Dariusz Szwedowicz, Martin Baltazar, Claudia Cortes, Tadeusz Majewski, Claudio A. Estrada; The performance of energy absorption in structural profiles with different discontinuities, Int J Adv Manuf Technol 84: 1081, 2016.

[38] L. Mirfendereski, M. Salimi, S. Ziaei-Rad, Parametric study and numerical analysis of empty and foam-filled thin-walled tubes under static and dynamic loadings, *Int. J. Mech. Sci*., 50 (6), pp. 1042-1057, 2008.

[39] M.D. Goel, Deformation, energy absorption and crushing behavior of single-, double-and multi-wall foam filled square and circular tubes, *Thin-Walled Struct*., 90, pp. 1-11, 2015.

[40] V.S. Deshpande, N.A. Fleck Isotropic constitutive models for metallic foams J. *Mech. Phys. Solids*, 48 (6–7), pp. 1253-1283, 2000.

[41] A. Reyes, O.S. Hopperstad, T. Berstad, M. Langseth, Implementation of a constitutive model for aluminum foam including fracture and statistical variation of density, in: Proceedings of the 8th International LS-DYNA Users Conference, Detroit, MI, 2004.

[42] Altın, M., Investigation of the energy absorption capacities of the crash boxes containing metalic foam used on vehicles, Unpublished doctoral dissertation, Gazi University, 2017.

[43] Alexander JM. An approximate analysis of the collapse of thin cylindrical shells under axial loading. Mechanics and Applied Mathematics; 13(1):5–10, 1960.

[44] Wierzbicki T, Abramowicz W. On the crushing mechanics of thin-walled structures. Applied Mechanics-Transactions ASME; 50(4):727–34, 1983.

[45] Abramowicz W, Wierzbicki T. Axial crushing of multi-corner sheet metal columns. Applied Mechanics-Transactions ASME; 56(1):113–20, 1989.

[46] Abramowicz W, Jones N. Dynamic axial crushing of square tubes. *International Journal of Impact Engineering;* 2(2):179–208, 1984.

[47] Abramowicz W, Jones N. Dynamic progressive buckling of circular and square tubes. International Journal of Impact Engineering; 4(4):243–70, 1986.

[48] Andrews KRF, England GL, Ghani E. Classification of the axial collapse of cylindrical tubes under quasi-static loading. International Journal of Mechan- ical Sciences; 25(9–10):687–96, 1983.

[49] Santosa S, Wierzbicki T. Crash behavior of box columns filled with aluminum honeycomb or foam. *Comput Struct*; 68:343–67, 1998.

[50] Hanssen AG, Langseth M, Hopperstad OS. Static and dynamic crushing of circular aluminum extrusions with aluminum foam filler. *Int J Impact Eng*; 24:475–507, 2000.

[51] Santosa SP, Wierzbicki T, Hanssen AG, Langseth M. Experimental and numerical studies of foam filled sections. *Int J Impact Eng*; 24:509–34, 2000.

[52] Chen W, Wierzbicki T. Relative merits of single-cell multi-cell and foam-filled thin-walled structures in energy absorption. *Thin-Walled Struct*; 39: 287–306, 2001.

[53] A. Niknejad, G.H. Liaghat, H. Moslemi Naeini, A.H. Behravesh, Theoretical and experimental studies of the instantaneous folding force of the polyurethane foam-filled square honeycombs, *Materials and Design*, 32:69–75, 2011.

[54] Niknejad, A., Abedi, M. M., Liaghat, G. H., & Nejad, M. Z., Absorbed energy by foam-filled quadrangle tubes during the crushing process by considering the interaction effects. *Archives of Civil and Mechanical Engineering*, *15*(2), 376-391, 2015.

[55] Mohammad Mahdi Abedi, Abbas Niknejad, Gholam Hossein Liaghat, Mohammad Zamani Nejad, Theoretical and experimental study on empty and foam-filled columns with square and rectangular cross section under axial compression, *International Journal of Mechanical Sciences*, 65:134–146, 2012.

[56] G. Sun, T. Pang, C. Xu, G. Zheng, J. Song, Energy absorption mechanics for variable thickness thin-walled structures, *Thin-Walled Struct*, 118, pp. 214-228, 2017.

[57] Xie S., Yang W., Wang N., Li H. Crashworthiness analysis of multi-cell square tubes under axial loads *Int. J. Mech. Sci*., 121, pp. 106-118, 2017.

[58] X. Zhang, G. Cheng, H. Zhang Theoretical prediction and numerical simulation of multi-cell square thin-walled structures *Thin-Walled Struct*., 44 (11), pp. 1185-1191, 2006.

[59] Googarchin H., Pasandidehpoor M., Mahmoodi A., Shojaeefard M. Energy absorption analysis for tapered multi-cell tubes improved by foams: Theoretical development and numerical simulation *Compos. Struct*., 207, pp. 213-222, 2019.

[60] Sun G., Chen D., Zhu G., Li Q. Lightweight hybrid materials and structures for energy absorption: A state-of-the-art review and Outlook *Thin-Walled Struct*., 172, 2022.

[61] Impact behaviour of hybrid composites for structural applications: A review, *Composites Part B*, 133:112-121, 2018.

[62] Kakogiannis D., Chung Kim Yuen S., Palanivelu S., Van Hemelrijck D., Van Paepegem W., Wastiels J., Vantomme J., Nurick G.N. Response of pultruded composite tubes subjected to dynamic and impulsive axial loading, Composites B, 55, pp. 537-547, 2013.

[63] Guades E., Aravinthan T., Manalo A., Islam M. Experimental investigation on the behaviour of square FRP composite tubes under repeated axial impact, Compos. Struct., 97, pp. 211-221, 2013.

[64] L. Wang, X. Fan, H. Chen, W. Liu Axial crush behavior and energy absorption capability of foam-filled GFRP tubes under elevated and high temperatures Compos Struct, 149, pp. 339-350, 2016.

[65] Palanivelu S., Paepegem W.V., Degrieck J., Vantomme J., Kakogiannis D., Ackeren J.V., Hemelrijck D.V., Wastiels J. Crushing and energy absorption performance of different geometrical shapes of small-scale glass/polyester composite tubes under quasi-static loading conditions Compos. Struct., 93 (2), pp. 992-1007, 2011.

[66] L. Wang, W. Liu, Y. Fang, L. Wan, R. Huo, Axial crush behavior and energy absorption capability of foam-filled GFRP tubes manufactured through vacuum assisted resin infusion process, Thin-Walled Structures, 98, pp. 263-273, 2016.

[67] Othman A., Abdullah S., Ariffin A.K., Mohamed N.A.N. Investigating the crushing behavior of quasi-static oblique loading on polymeric foam filled pultruded composite square tubes Compos. B Eng., 95, pp. 493-514, 2016.

[68] L.i. Chen, D. Pan, Q. Zhao, L.i. Chen, L. Niu, L. Cong, et.al., Overall buckling characteristics of slender FRP-foam sandwich tube under axial compression, Compos Commun, 24, Article 100585, 2021.

[69] Qing Jin, Jun Wang, Jiye Chen, Fengling Bao, Axial compressive behavior and energy absorption of syntactic foam-filled GFRP tubes with lattice frame reinforcement, Composite Structures, Volume 299, 116080, ISSN 0263-8223, 2022.

[70] J. Wang, H. GangaRao, M. Li, R. Liang, W. Liu, Axial behavior of columns with glass fiber-reinforced polymer composite shells and syntactic foam core, J Compos Constr, 23 (2), p. 04018083, 2019.

[71] Mirzaei M., Shakeri M., Sadighi M., Akbarshahi H. Experimental and analytical assessment of axial crushing of circular hybrid tubes under quasi-static load Compos. Struct., 94 (6), pp. 1959-1966, 2012.

[72] HW Song, ZM Wan, ZM Xie, XW. Du Axial impact behavior and energy absorption efficiency of composite wrapped metal tubes *Int. J. Impact Eng*., 24, pp. 385-401, 2000.

[73] K.C. Shin, J.J. Lee, K.H. Kim, M.C. Song, J.S. Huh, Axial crush and bending collapse of an aluminum/GFRP hybrid square tube and its energy absorption capability, *Compos. Struct*., 57, pp. 279-287, 2002.

[74] A. Tarafdar, G. Liaghat, H. Ahmadi, et al. Quasi-static and low-velocity impact behavior of the bio-inspired hybrid Al/GFRP sandwich tube with hierarchical core: Experimental and numerical investigation *Compos Struct*, 276, Article 114567, 2021.

[75] J. Babbage, P. Mallick, Static axial crush performance of unfilled and foam-filled aluminum–composite hybrid tubes, *Compos. Struct*., 70, pp. 177-184, 2005.

[76] M. Guden, S. Yuksel, A. Tasdemirci, M. Tanoglu; Effect of aluminum closed-cell foam filling on the quasi-static axial crush performance of glass fiber reinforced polyester composite and aluminum/composite hybrid tubes, Compos Struct, 81 (4), pp. 480-490, 2007.

[77] Subbaramaiah R., Prusty B.G., Pearce G.M.K., Lim S.H., Thomson R.S. Crashworthy response of fibre metal laminate top hat structures Compos. Struct., 160, pp. 773-781, 2017.

[78] El-Hage H., Mallick P., Zamani N. A numerical study on the quasi-static axial crush characteristics of square aluminum–composite hybrid tubes Compos. Struct., 73 (4), pp. 505-514, 2006.

[79] H. Han, F. Taheri, N. Pegg, Y. Lu A numerical study on the axial crushing response of hybrid pultruded and±45 braided tubes Compos Struct, 80 (2), pp. 253-264, 2007.

[80] Z. Zhang, W. Sun, Y. Zhao, S. Hou, Crashworthiness of different composite tubes by experiments and simulations, Compos B Eng, 143, pp. 86-95, 2018.

[81] Deepak Siromani, Jonathan Awerbuch, Tein-Min Tan, Finite element modeling of the crushing behavior of thin-walled CFRP tubes under axial compression, Composites Part B: Engineering, Volume 64, Pages 50-58, 2014.

[82] Yan Tong, Yuanming Xu, Improvement of crash energy absorption of 2D braided composite tubes through an innovative chamfer external triggers, International Journal of Impact Engineering, Volume 111, Pages 11-20, 2018.

[83] S. Boria, S. Pettinari, F. Giannoni, G. Cosimi, Analytical and numerical analysis of composite impact attenuators, Compos Struct, 156, pp. 348-355, 2016.

[84] S. Boria, J. Obradovic, G. Belingardi, Experimental and numerical investigations of the impact behaviour of composite frontal crash structures, Composites Part B: Engineering, Volume 79, 15, Pages 20-27, 2015.

[85] Carla McGregor, Reza Vaziri, Xinran Xiao, Finite element modelling of the progressive crushing of braided composite tubes under axial impact, International Journal of Impact Engineering, Volume 37, Issue 6, Pages 662-672, 2010.

[86] Aleksandr Cherniaev, Clifford Butcher, John Montesano, Predicting the axial crush response of CFRP tubes using three damage-based constitutive models, Thin-Walled Structures, Volume 129, Pages 349-364, 2018.

[87] L.W. Ying, F.P. Yang, X. Wang; Analytical method for the axial crushing force of fiber-reinforced tapered square metal tubes, Compos Struct, 153, pp. 222-233, 2016.

[88] Qiang Liu, Jingbo Ma, Xiyu Xu, Yinghan Wu, Qing Li, Load bearing and failure characteristics of perforated square CFRP tubes under axial crushing, Composite Structures, Volume 160, Pages 23-35, 2017.

[89] Danghe Shi, Xinran Xiao, A new shell-beam element modeling method and its use in crash simulation of triaxial braided composites, Composite Structures, Volume 160, Pages 792-803, 2017.

[90] Danghe Shi, Xinran Xiao, An enhanced continuum damage mechanics model for crash simulation of composites, Composite Structures, Volume 185, 774-785, 2018.

[91] Software Technology Corporation L. LS-DYNA ® Keyword User's Manual Volume II Material Models Livermore Software Technology Corporation (LSTC), 2014.

[92] Foam filling options for crashworthiness optimization of thin-walled multitubular circular columns, Thin-Walled Structures 131:309–323, 2018.

[93] Harral A., Material Properties of Aluminum 6061 T6 for MAT_18, Retrieved December 7, 2022 varmintal.com/aengr.htm#MaterialDataBase, 2018.

[94] Constitutive Models Onvestigation to simulate damage/failure of Aluminium (Al) 6061-T6, Defence Research and Development Canada, Scientific Report, 2018.

[95] Arcillas A., Mechanical Behavior, Testing, and Manufacturing Properties of Materials, Accessed December 7, 2022, Available from: https://www.academia.edu/25452539/Mechanical_Behavior_Testing_and_Manufacturing_Properties_of_Materials, 2022.

[96] Huang, J., & Wang, X., Numerical and experimental investigations on the axial crushing response of composite tubes. Composite Structures, 91(2), 222-228, 2009.

[97] A. Atthapreyangkul, B.G. Prusty; Experimental and numerical analysis on the geometrical parameters towards the maximum SEA of CFRP Components, Compos Struct, 164, pp. 229-236, 2016.

[98] J. Huang, X. Wang; Numerical and experimental investigation on the axial crushing response of composite tubes, Compos Struct, 91, pp. 222-228, 2009.

[99] C. Reuter, K.-H. Sauerland, T. Tröster Experimental and numerical crushing analysis of circular CFRP tubes under axial impact loading Compos Struct, 174, pp. 33-44, 2017.

[100] Meriç D., Gedikli H., Multi-objective optimization of energy absorbing behavior of foam-filled hybrid composite tubes. Compos Struct 279:114771, 2022.

[101] A. Rabiee, H. Ghasemnejad, Effect of multi stitched locations on high speed crushing of composite tubular structures, Composites Part B: Engineering, Volume 100, Pages 164-175, 2016.

CURRICULUM VITAE

PERSONAL INFORMATION

Name Surname **:** Sinem Kocaoğlan Mert
Date of Birth **:**
E-mail **:**

EDUCATION

Bachelor **:** Celal Bayar University (2004 - 2008)
Master Degree **:** Boğaziçi University (2009 - 2013)
PhD **:** Ankara Yıldırım Beyazıt University (2013 - 2022)

WORK EXPERIENCE

Expert **:** TÜBİTAK (2011-present)

PUBLICATIONS

[1] Ozturk, Murat, Sinem Kocaoglan, and Fazil O. Sonmez. "Concurrent design and process optimization of forging." *Computers & Structures* 167 (2016): 24-36.

[2] Altin, Murat, Mehmet A. Güler, and Sinem K. Mert. "The effect of percent foam fill ratio on the energy absorption capacity of axially compressed thin-walled multi-cell square and circular tubes." *International Journal of Mechanical Sciences* 131 (2017): 368-379.

[3] Güler, Mehmet Ali, Muhammed Emin Cerit, Sinem Kocaoglan Mert, and Erdem Acar. "Experimental and numerical study on the crashworthiness evaluation of an intercity coach under frontal impact conditions." *Proceedings of the Institution of Mechanical Engineers, Part D: Journal of Automobile Engineering* 234, no. 13 (2020): 3026-3041.

[4] Mert, Sinem K., Murat Demiral, Murat Altin, Erdem Acar, and Mehmet A. Güler. "Experimental and numerical investigation on the crashworthiness optimization of thin-walled aluminum tubes considering damage criteria." *Journal of the Brazilian Society of Mechanical Sciences and Engineering* 43, no. 2 (2021): 1-22.